The Astrophysical Journal, 801:45 (31pp), 2015 March 1 doi:10.1088/0004-637X/801/1/45

ESTIMATING BLACK HOLE MASSES IN HUNDREDS OF QUASARS

Nina Hernitschek[1], Hans-Walter Rix[1], Jo Bovy[2,4], and Eric Morganson[3]
[1] Max-Planck-Institut für Astronomie, Königstuhl 17, D-69117 Heidelberg, Germany; hernitschek@mpia-hd.mpg.de
[2] Institute for Advanced Study, School of Natural Sciences, Einstein Drive, Princeton, NJ 08540, USA
[3] Harvard-Smithsonian Center for Astrophysics, 60 Garden St, Cambridge, MA 02138, USA
Received 2014 July 16; accepted 2014 December 29; published 2015 March 2

ABSTRACT

We explore the practical feasibility of active galactic nucleus (AGN) broadband reverberation mapping and present first results. We lay out and apply a rigorous approach for the stochastic reverberation mapping of unevenly sampled multi-broadband flux measurements, assuming that the broad-line region (BLR) line flux is contributing up to 15% in some bands, and is directly constrained by one spectroscopical epoch. The approach describes variations of the observed flux as the continuum, modeled as a stochastic Gaussian process, and emission line contribution, modeled as a scaled, smoothed, and delayed version of the continuum. This approach can be used not only to interpolate in time between measurements, but also to determine confidence limits on continuum—line emission delays. This approach is applied to Sloan Digital Sky Survey observations in Stripe 82 (S82), providing flux measurements that are precise to 2% at ∼60 epochs over ∼10 yr. The strong annual variations in the epoch sampling prove a serious limitation in practice. In addition, suitable redshift ranges must be identified where strong, broad emission lines contribute to one filter, but not to another. By generating and evaluating problem-specific mock data, we verify that S82-like data can constrain $\tau_{\rm delay}$ for a simple transfer function model. In application to real data, we estimate $\tau_{\rm delay}$ for 323 AGNs with $0.225 < z < 0.846$, combining information for different objects through the ensemble-scaling relationships for BLR size and black hole mass. Our analysis tentatively indicates a 1.7 times larger BLR size of Hα and Mg II compared to Kaspi et al. and Vestergaard, but the seasonal data sampling casts doubt on the robustness of the inference.

Key words: galaxies: photometry – quasars: supermassive black holes

1. INTRODUCTION

Quasars have long been known to exhibit rapid optical variability that can be attributed to variations in the luminosity of the accretion disk surrounding a black hole of typically $10^8\,M_\odot$ (Smith & Hoffeit 1963; Greenstein & Smith 1964).

Reverberation mapping (Blandford & McKee 1982; Kaspi et al. 2000) is an established way for estimating the size of the active galactic nucleus' (AGN's) broad-line region (BLR). The continuum radiation from the accretion disk photo-ionizes and excites gas clouds close to the black hole to produce broad (about 1000 to 10,000 km s^{-1}) emission lines. In reverberation mapping, the time delay $\tau_{\rm delay}$ between observed variations in the accretion disk continuum and the broad emission lines is a proxy for $R_{\rm BLR}$ as light-travel time arguments lead to $R_{\rm BLR} \propto c\,\tau_{\rm delay}$. For Keplerian motions of the BLR clouds, this implies for the mass of the central black hole, $M_{\rm BH}$

$$M_{\rm BH} = f\,\frac{\Delta V^2 c\,\tau_{\rm delay}}{G} \qquad (1)$$

where G is the gravitational constant and f is a proportionality factor of order unity that depends on the geometry and kinematics of the BLR (e.g., Peterson & Wandel 1999). Detailed descriptions of this method as well as applications can be found, for example, in Peterson (1997), Peterson & Wandel (1999), Peterson (2013), and Kaspi et al. (2000).

With the benefits of many spectral observational epochs in reverberation mapping campaigns, given reliable average emission line widths Δv, reverberation mapping provides reliable direct measurements of the size of the BLR and the black hole mass (e.g., Kaspi et al. 2007; Peterson et al. 2004). Kaspi et al. (2000) presents an $M_{\rm BH}$–L relation based on spectrophotometrical reverberation measurements for a sample of 17 Palomar-Green quasars, and a total of 34 sources, including low-L AGNs.

They obtained the size of their BLRs and determined relationships between line luminosities, BLR sizes, and central black hole masses to find that the BLR size scales with the rest frame 5100 Å luminosity as

$$R_{\rm BLR} = \left(32.0^{+2.0}_{-1.9}\right)\left(\frac{\lambda L_\lambda(5100\ \text{Å})}{10^{44}\ \text{erg s}^{-1}}\right)^{0.700\pm0.033}\ \text{light days}. \qquad (2)$$

Comparable studies have been done by Vestergaard et al. (Vestergaard 2002; Vestergaard & Peterson 2006) and Bentz et al. (2009). They found four empirical mass scaling relationships between the line widths and luminosity for estimating $M_{\rm BH}$ in nearby AGNs and distant luminous quasars. Those mass estimates are quite rough. For example, Vestergaard (2002) indicate the absolute uncertainties in masses estimated from the relationships of a factor of ∼4.

The purpose of the present study is to estimate BLR sizes from existing multi-epoch broadband flux measurements. We build on the formalism from Zu et al. (2011) and Chelouche & Daniel (2012) and extend it to handle sparsely sampled broadband photometric data.

The basic idea is that some of the photometric passbands contain only continuum emission, while other passbands have significant contributions from continuum and (temporally delayed) line flux. Recent results from Haas et al. (2011), who tested narrow-band photometric reverberation mapping, and Chelouche & Daniel (2012) and Chelouche & Zucker (2013), who suggested broadband photometric reverberation mapping,

[4] Hubble Fellow.

illustrate the potential of using photometric data. Zu et al. (2013a) compared the results of spectroscopic and photometric reverberation mapping applied to the Palomar-Green quasars and OGLE-III and IV. They found that the photometric approach is capable of competing with spectroscopic reverberation mapping if very small photometric uncertainties are available and strong lines (Hα, Hβ) are used. Upcoming photometric surveys, such as the LSST, are planned to continuously monitor at least 10^7 quasars ($0 < z < 6$) during the next decade (MacLeod et al. 2012). Broadband photometric reverberation mapping can use such data to make the mass estimate of large samples of objects feasible to increase the number of reverberation mapped objects by several orders of magnitude (e.g., Chelouche et al. 2014).

This formalism was first tested on mock light curves generated by a Gaussian stochastic process. Then it was applied to a suitable set of multi-band quasar light curves, drawn from the nearly 10,000 spectroscopically confirmed quasars in the Sloan Digital Sky Survey Stripe 82 (SDSS S82; Schmidt et al. 2010; Schneider et al. 2007), which were complemented by a spectroscopic measurement of the emission line widths for each quasar at one epoch. Due to the small expected signal and the S82 time sampling, we found it useful to not focus on the $\tau_{\rm delay}$ estimates of individual objects, but to presume that there is a $R_{\rm BLR}(L)$ relation, and determine its scaling normalization in different redshift and luminosity regimes by jointly modeling several light curves. The reverberation mapping results are compared to estimates from $M_{\rm BH}$–L relationships in Kaspi et al. (2000), Vestergaard (2002) and Bentz et al. (2013).

This paper is organized as follows. In Section 2 we give an overview of reverberation mapping, especially the theory behind this method, and preliminary reverberation mapping results. After introducing the methods of describing quasar variability as a stochastic process in Section 3, we introduce the stochastic reverberation mapping approach in Section 4. This is outlined in more detail in Appendix A, where the mathematical framework of the stochastical process model for the light curve and the application of the method to data are described. After describing the application to SDSS S82 data in Section 5, results are shown in Section 6. In Section 7, we conclude with a discussion of results. In the table section we provide a complete list of estimated masses for all quasars from our samples where reverberation mapping was carried out successfully.

2. REVERBERATION MAPPING

Over the duration of a reverberation mapping program, the continuum behavior can be written as $f^c(t) = \langle f^c \rangle + \Delta f^c(t)$, where $\Delta f^c(t)$ is the continuum light curve relative to its mean value $\langle f^c \rangle$, given in arbitrary flux units (Peterson 1997). Integrated over the velocity-dependent line profile, the emission-line response can be written as a function of the line-of-sight velocity v as $f^e(t) = \langle f^e \rangle + \Delta f^e(t)$. On reverberation timescales (weeks to years), both continuum and emission-line variations are usually rather small (typically ~10–20%), so the response of the emission line flux to (e.g., increased) continuum flux can be modeled by a convolution integral (Peterson 1997)

$$\Delta f^e(t) = \int \Psi(\tau_{\rm delay}) \Delta f^c(t - \tau_{\rm delay})\, d\tau_{\rm delay}, \qquad (3)$$

which is usually known as the *transfer equation*, where $\Psi(\tau_{\rm delay})$ is the *transfer function*. In its mathematically simplest form, this transfer function can be taken as a δ function that is offset in time by $\tau_{\rm delay}$, $\Psi(\tau_{\rm delay}) = \delta(t - \tau_{\rm delay})$. The BLR geometry and detailed spectrosopic data for nearby objects indicate that such a transfer function is too simplistic; nonetheless, we use this approach involving a δ function transfer function in this study, because broadband reverberation mapping is unlikely to yield any velocity-dependent information. This leads to a scaling and delay during the transfer function, whereas the use of other transfer functions can also lead to smoothing.

The goal of reverberation mapping is to use the observables, namely the continuum light curve $f^c(t)$ and emission-line light curve $f^e(t)$, and invert the transfer equation (3) in order to recover the velocity–delay map $\Psi(\tau_{\rm delay})$, or at least make inferences about $\tau_{\rm delay}$ (Peterson 1997).

When spectroscopic reverberation mapping data are available, a cross-correlation approach between the pure line and continuum light curves has often been employed (Peterson 1997). For the case of broadband photometric light curve data, a simple model to illustrate the calculations based on photometric data is

$$\begin{aligned} f_k(t) &= f_k^c(t) \\ f_l(t) &= f_l^c(t) + f_l^e(t) \\ &= s\, f_k^c(t) + e\, f_k^c(t - \tau_{\rm delay}) \end{aligned} \qquad (4)$$

where $f(t)$ is the flux on each time, index k denotes a band with only continuum, l a continuum and emission line contribution band, the superscripts ^{c} and ^{e} denote continuum or emission line contributions, $\tau_{\rm delay}$ is the delayed response, and s and e are scaling factors. For estimating the delay $\tau_{\rm delay}$ between the continuum flux $f_k^c(t)$ and emission line flux $f_l^e(t)$, one must compute the cross-correlation function (CCF) between these two components of the light curve (Edri et al. 2012):

$$\begin{aligned} {\rm CCF}(\Delta t) &= f_l^e(t + \Delta t) * f_l^c(t) \\ &= \left(f_l(t + \Delta t) - f_l^c(t + \Delta t)\right) * f_l^c(t) \end{aligned}$$

where $*$ denotes the integral over time (convolution between the two functions).

The peak (maximum) of the CCF (Δt) gives the required time delay $\tau_{\rm delay}$.

We now assume that the time variability of the continuum flux in the l band is the same as in the k band. This is a good approximation in the optical because the continuum is 75%–95% of the total flux, where the remaining variable flux is mostly coming from the broad lines. With this approximation, $f_l^c(t) \approx f_k(t)$, and $e \ll 1$ (Equation (4)), so that CCF(0) $\sim$ 1, this leads to:

$$\begin{aligned} {\rm CCF}(\Delta t) &\approx \left(f_l(t + \Delta t) - f_k(t + \Delta t)\right) * f_k(t) \\ &\approx {\rm CCF}_{lk}(\Delta t) - {\rm ACF}_k(\Delta t). \end{aligned} \qquad (5)$$

This approximation was also used by Chelouche & Daniel (2012). One complication to consider when calculating the CCF and the autocorrelation function (ACF) is the non-uniform time sampling that is generic for astronomical data. In order to overcome this difficulty, some authors use the interpolated cross-correlation function method (ICCF; Gaskell & Peterson 1987), where mean and standard deviation of the time series are calculated at every time step, taking into account only the values within the overlapping part of the light curves. Another complication arises from propagating the magnitude errors to errors for the time delay. Most of the CCF-related approaches have problems doing so. Both problems can be solved with advanced reverberation mapping techniques based on fitting and modeling the light curves using a structure-function model. What is explained here for the CCF and ACF, will also apply basically to more advanced reverberation mapping techniques.

3. QUASAR LIGHT CURVES AS A STOCHASTIC PROCESS

Simple interpolation methods may fail when trying to carry out reverberation mapping on sparsely and very non-uniformly sampled light curves. Some methods, such as ICCF (Gaskell & Peterson 1987), have been developed to deal with some degree of non-uniform time sampling. However, for temporal sampling as uneven as in S82, we found that these methods are not suitable (as we demonstrate in Appendix C.2. For the case at hand we need a description of the quasar variability that rigorously accounts for all the information we have on the overall light-curve statistics, when interpolating between measurements. Following Kozłowski et al. (2010) and Butler & Bloom (2011), we build a model for the quasar light curves based on a Gaussian process, because the Gaussian is the simplest two-point distribution function with a non-trivial variance that allows one to fit and stochastically interpolate light curves.

Quasar light curves vary stochastically across a large dynamic range of timescales (e.g., Kozłowski et al. 2010). Their variability is sensibly characterized by a *structure function* (e.g., Hughes et al. 1992; Collier & Peterson 2001; Kozłowski et al. 2010) that describes the mean squared difference (or, sometimes, root mean square difference) between pairs of observations of some object's brightness as a function of the time lag difference between the observations. In more detail, the structure function is a description of a second-order statistic of the brightness history of the source. As such, it does not give a direct description on how to fit such measurements or generate mock data.

A model and algorithm based on this is built to have a consistent description of quasar variability, from which we cannot only estimate structure function parameters of given light curves, but also generate mock light curves consistent with any reasonable set of structure function parameters, fit light curves, and, as a main goal, produce a reverberation mapping model that is able to deal with the very uneven time sampling present in SDSS S82 quasar light curves. Because the Gaussian is the simplest two-point distribution function with a non-trivial variance that meets these conditions, we build this model from a Gaussian process. The description here is mainly based on Butler & Bloom (2011).

We assume a set of N measurements m_i taken at time t_i, being calibrated magnitude or flux measurements taken in a single bandpass of a single source associated with an uncertainty variance σ_i. The structure function $V(|\Delta t|)$ is then defined (Rybicki & Press 1992) as the expectation value $E[\cdot]$ for the difference between observation m_i and m_j (with $i \neq j$),

$$E[(m_i - m_j)^2] = \sigma_i^2 + \sigma_j^2 + V(|t_i - t_j|). \quad (6)$$

Here, the observations are presumed to be independent, and the structure function $V(\cdot)$ effectively describes the variance.

To proceed, one must specify a concrete form for the quasar structure function, and two forms have been used in literature (e.g., Schmidt et al. 2010, Butler & Bloom 2011, MacLeod et al. 2010), first a power law

$$V(|\Delta t_{ij}|) = A^2 \left(\frac{\Delta t_{ij}}{1\ \mathrm{yr}}\right)^{\gamma} \quad (7)$$

(e.g., Schmidt et al. 2010), where the amplitude A quantifies the root-mean-square magnitude difference on a 1 yr timescale, and γ characterizes the time dependence of this difference. As $V_{\Delta t=\infty} \rightarrow \infty$, for V_∞, it is practical to use reference values, $V(t_{\mathrm{obs}})$ and t_{obs} in the characterization.

Second, one can describe the quasar structure function as a damped random walk (DRW), for which the covariance function of a Gaussian process has an exponential form

$$C_{ij} = \frac{\omega^2}{2} \exp\left(-\frac{|\Delta t_{ij}|}{\tau}\right), \quad (8)$$

(e.g., Butler & Bloom 2011) where τ is a damping timescale and ω^2 is the intrinsic variance of the process. Following MacLeod et al. (2012), using the asymptotic value of the structure function V ($V_\infty = \sqrt{2}\omega$) results in

$$V(|\Delta t_{ij}|) = \frac{\omega^2}{2}\left(1 - \exp\left(\frac{-2|\Delta t_{ij}|}{\tau}\right)\right). \quad (9)$$

The DRW model can be equivalently parameterized τ and the slope of V on short timescales, $\hat{\omega} = \sqrt{2\omega^2/\tau}$ (Kelly et al. 2009).

A detailed description can be found in Appendix A.

Depending on the application, $|\Delta t_{ij}|$ can refer to the time lag between observations in the quasar rest frame or in the observed frame. Referring to the quasar rest frame, which needs a priori knowledge of the quasar redshift, can be important if the structure-function parameters being estimated should be linked to physical properties of a quasar.

There is some discussion about which structure-function model would fit best. Kelly et al. (2009), Kozłowski et al. (2010), MacLeod et al. (2012), and Andrae et al. (2013) have shown that quasar variability is well modeled by the DRW. Zu et al. (2013b) tested whether the DRW model provides an adequate description of quasar variability across all timescales. On timescales larger than a few years, the light curves are generally consistent with the DRW model, but are not giving clear constraint on models. Alternatively, some authors (Hook et al. 1994; Richards et al. 2006, 2008; Schmidt et al. 2010; Morganson et al. 2014) use the power-law model described above.

The structure function is the basis for the Gaussian process model that we fit to the data.

A Gaussian process is characterized by a function describing the mean measurement $\mathbf{m}(t)$ (magnitude or flux) as a function of time t and a function $C(t, t')$ describing the covariance between observations at different epochs t and t'. Assuming that the mean is constant and the process is stationary such that $C(t, t') \equiv C(t - t')$, the probability of a set of N observations $\{m_i\}_{i=1}^N$ is given by that of the N-dimensional Gaussian with mean $(m, m, ..., m)^{\mathrm{T}}$ and $N \times N$ dimensional covariance matrix C with elements $C_{ij} = C(t_i - t_j)$.

After parameterizing the structure function, the complete model—the Gaussian process with mean vector $\bar{\mathbf{m}}$ and variance V—for any set of observations is specified by only three model parameters, either in the case of the power law $(\bar{m}, A, \gamma)$ or in the case of a damped random walk $(\bar{m}, \omega, \tau)$. Thus, the likelihood $P(\mathrm{data}|\mathrm{modelpar})$ can be described as $P(\mathbf{m}, A, \gamma) = N(\mathbf{m}|\bar{m}, C)$ or $P(\mathbf{m}, \omega, \tau) = N(\mathbf{m}|\bar{m}, C)$, respectively, with V expressed as a function of the structure-function parameters (A, γ) or (ω, τ), respectively. The term $N(\mathbf{m}|\bar{m}, C)$ is the Gaussian process. This approach can yield a posterior probability distribution to the two model parameters, A and γ or ω and τ. We assign uninformative priors for the parameters, and then explore the posterior distribution for these parameters via a Markov Chain Monte Carlo (MCMC) approach. By using this, one can (a) model the light curve to get an estimate for the structure function parameters, (b) use the estimates for the structure function parameters (e.g., for selecting quasars), or for advanced

reverberation mapping techniques as in the present work that require interpolation of the light curves, and (c) generate mock light curves as test data for this methods.

In the following, we refer to the formalism by Rybicki & Press (1992) and Zu et al. (2011), and summarize them here for convenience.

In practice, we marginalize over the mean $\bar{m}$ rather than fitting for it. This marginalization can be done analytically when assuming a uniform prior on the mean (see Rasmussen & Williams 2006, Equation (2.45)), and leads to the probability

$$P(\mathbf{m}|\mathbf{p}) \propto \mathcal{L}(\mathbf{m}|\mathbf{p}) \equiv |S+N|^{-1/2}|L^{\mathrm{T}}C^{-1}L|^{-1/2} \times \exp\left(-\frac{\mathbf{m}^{\mathrm{T}}C_{\perp}^{-1}\mathbf{m}}{2}\right), \quad (10)$$

where for the damped random walk model the remaining parameters $\mathbf{p}$ are τ and ω, and for the power-law model A and γ. $\mathcal{L}$ represents the likelihood function that we must maximize in order to find the most likely combination of those parameters.

In Equation (10), the intrinsic variability has a covariance matrix $S = \langle \mathbf{ss} \rangle$, whereas the noise has a covariance matrix $N = \langle \mathbf{nn} \rangle$. The covariance function of the Gaussian process is then given by $C = S + N$. The component of the covariance matrix C that is orthogonal to the fitted linear functions is given by $C_{\perp}^{-1} \equiv C^{-1} - C^{-1}LC_qL^{\mathrm{T}}C^{-1}$. $\mathbf{m}$ is the data vector. L is a response matrix (see Zu et al. 2011 and Press & Rybicki 1992).

Suppose we have measured data $\mathbf{m}$ consisting of an underlying true signal $\mathbf{s}$, measurement uncertainties $\mathbf{n}$, and a general trend defined by the response matrix L and a set of linear coefficients $\mathbf{q}$, thus, $\mathbf{m} = \mathbf{s} + \mathbf{n} + L\mathbf{q}$. Using the linear coefficients to optimally determine the light curve mean, in the case of one light curve, we have one linear coefficient $q_1 \equiv \mathbf{q}$ for the mean, and the response matrix is simply a column vector $L_{i1} = 1$ with an entry for each of the K data points, $i = 1, \ldots, K$. If we have two light curves with a possible offset in their means, we could use separate means for each, $(L_{i1}, L_{i2}) = (1, 0)$ for data from the first light curve and $(L_{i1}, L_{i2}) = (0, 1)$ for the second one. Additionally, L can be used for light curve de-trending. For details on how we implemented de-trending, see Section 4.1.2.

The Gaussian-process formalism also allows for straightforward interpolation of the observed light curve between time samples with interpolation uncertainties, or the construction of mock light curves with a given structure function. We use the latter to generate mock light curves to test our photometric reverberation mapping technique. This formalism is explained in detail in Rasmussen & Williams (2006) and Rybicki & Press (1992). We refer the reader to those references for full details.

For an example light curve (Figure 1), this fit is shown in the left panel of Figure 2. We also give the best model parameter values along with the confidence regions (see below) in the right panel of Figure 2.

The expression in terms of a Gaussian process allows one to generate a wide variety of mock light curves as test data for applications dealing with light curves, such as structure-function parameter estimation or reverberation mapping.

As the fundamental property of a Gaussian process is that all of its marginal distributions—marginalizing over unobserved times—are Gaussian, generating a mock light curve is then just sampling from the appropriate Gaussian distribution. Realistic values in the power-law case are $0.07 < A < 0.28$, $0.15 < \gamma < 0.5$ (Schmidt et al. 2010). In the power-law model, the amplitude A quantifies the root-mean-square magnitude difference on a 1 yr timescale. γ is the logarithmic gradient of this mean change in magnitude. In DRW model, a larger ω makes the curve more variable, and a larger τ makes it more smooth (variability on longer timescales). Realistic values in the DRW case are $0.1 < \omega < 0.4$, $1 < \log \tau < 3$ (MacLeod et al. 2010).

4. STOCHASTIC REVERBERATION MAPPING

As reverberation mapping is often carried out using CCF and ACF, a complication to consider when calculating the CCF and ACF is the non-uniform time sampling that is generic for astronomical data. In addition, in order to estimate the time delay and its uncertainty, we need to propagate the magnitude errors in the light curves to errors for the time delay. Most of the CCF-related approaches have problems with doing so because they are not able to propagate errors. Additionally, in Appendix C.2 we demonstrate that for a S82-like time sampling, these approaches are not sufficient. Both problems can be solved by advanced reverberation mapping techniques based on fitting and modeling the light curves using a structure-function model so the structure-function parameters, the time lag τ_{delay}, its statistical confidence limits, and in some cases additional values are estimated.

In detail, we follow the approach of Rybicki & Kleyna (1994) and Zu et al. (2011), which we extended for application to broadband photometry. The basic methodology is described here, and is outlined in more detail in Appendix A.1, where the mathematical framework and application of the method to the data are described. Additionally, the methodology and output of the stochastic reverberation mapping algorithm is summarized in Figure 4.

The approach being described in this section is capable of

1. handling transfer functions $\Psi(\tau_{\mathrm{delay}})$ instead of simply a τ_{delay}, thus being able to map out the physical structure of the broad-line region that cannot simply be modeled by a δ function
2. not only interpolating between data points, but also making self-consistent estimates and including these uncertainties in the interpolation
3. separating light curve means and systematic errors in flux calibration from variability signals and measurement uncertainties in a self-consistent way
4. deriving simultaneously the lags of multiple emission lines and their covariances
5. providing statistical confidence limits on all estimated parameters

The approach assumes that all emission-line light curves are scaled, smoothed, and displaced versions of the continuum. We assume for simplicity that we have photometric quasar light curves in the k (e.g., SDSS r) and l (e.g., SDSS g) bands, where the l band contains emission line and continuum flux, and the k band has continuum only. Then we can write the fluxes as

$$\begin{aligned} f_k(t) &= f_k^c(t) \\ f_l(t) &= f_l^c(t) + f_l^e(t) \\ &= s\, f_k^c(t) + e \int \Psi(\tau_{\mathrm{delay}}) f_k^c(t - \tau_{\mathrm{delay}})\, d\tau_{\mathrm{delay}}. \end{aligned} \quad (11)$$

This equation is the general version of (4), allowing for a smoothed response due to the arbitrary transfer functions. In (11), f_k and f_l are the total fluxes in the k and l band, respectively, and superscripts ^{c} and ^{e} denote continuum and emission-line contributions. s and e are linear scaling factors between

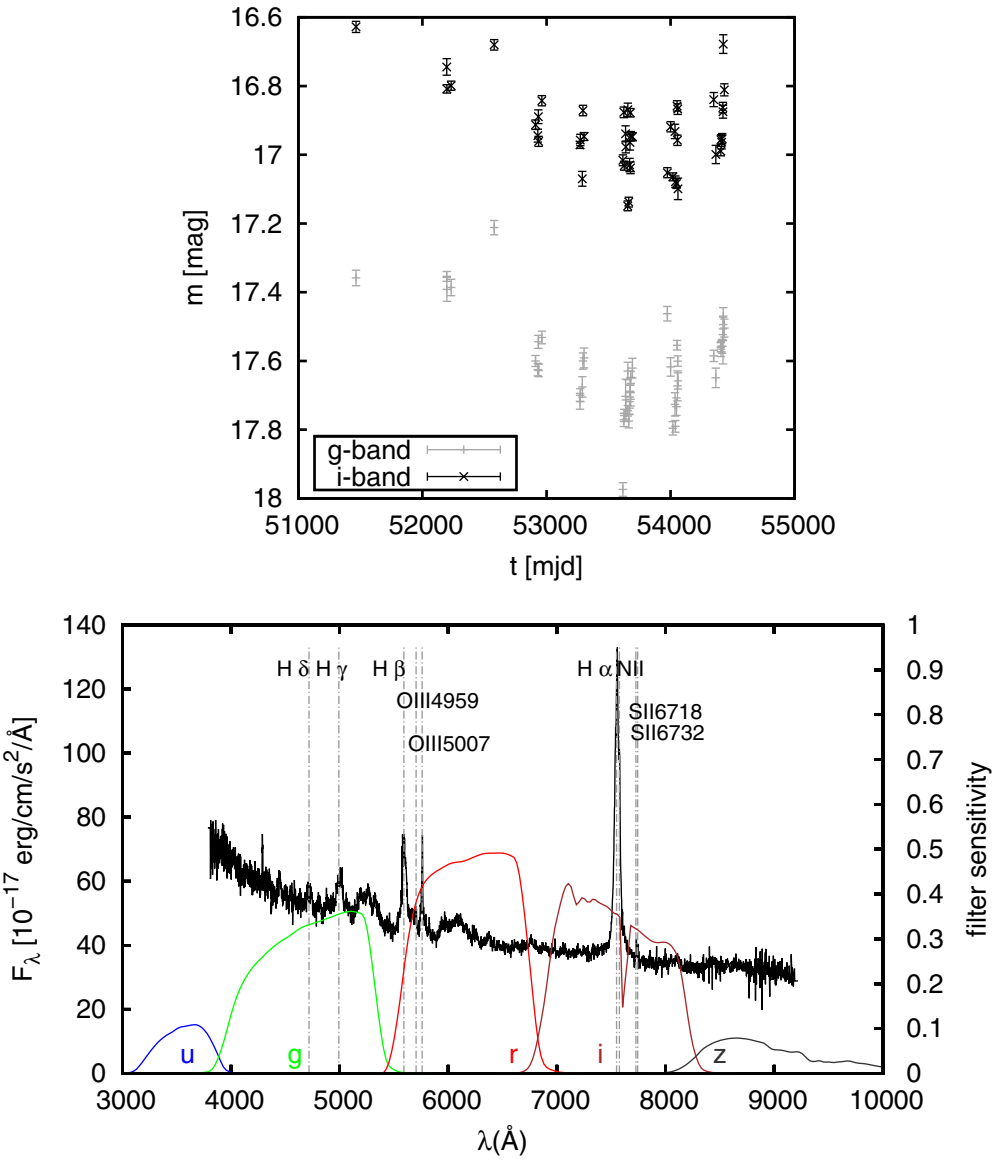

Figure 1. Magnitudes in two filter bands of the example light curve headobjid = 587731185126146081 and corresponding spectrum plate = 383, fiber = 257, mjd = 51818; the light curve is from a spectroscopically confirmed quasar of the SDSS Stripe 82 in a redshift region where the *g* band reflects almost exclusively accretion disk continuum emission, whereas the *i* band has Hα emission line contribution. Additionally, other emission lines are present.

k and *l* band variability. In our application, they are constrained spectroscopically (see Equations (27) and (28)). The delayed response to the continuum is described by the normalized one-dimensional transfer function $\Psi(\tau_{\rm delay})$ (Peterson 1997), that is,

$$f^e(t) = \int_{-\infty}^{+\infty} \Psi(\tau_{\rm delay}) f^c(t - \tau_{\rm delay})\, d\tau_{\rm delay}. \quad (12)$$

The generalization of this formalism to the case of two or more emission lines in separate bands is straightforward. We did not use this here because it was not appropriate for the light curves we had analyzed. In the case of a δ function transfer function, Equation (11) reduces to Equation (4).

We assume that the quasar continuum light curve can be described as a Gaussian stochastic process (e.g., Kozłowski et al. 2010, MacLeod et al. 2012) and that the *l*-band flux varies linearly with the *k*-band flux (Schmidt et al. 2012). The continuum model is then characterized by a variance matrix C^{cc}_{kk} resulting from any Gaussian stochastic variability process, for example, the damped random walk Kelly et al. (2009) or a power-law structure function model (Schmidt et al. 2010). The emission-line covariance matrix C^{ee}_{ll} is then given by

$$\begin{aligned} C^{ee}_{ll}(\Delta t) &= \langle f^e_l(t),\, f^e_l(t+\Delta t)\rangle \\ &= e^2 \int d\tau_{\rm delay,1} \int d\tau_{\rm delay,2} \Psi(\tau_{\rm delay,1})\Psi(\tau_{\rm delay,2}) C^{cc}_{kk} \\ &\quad \times (\Delta t - \tau_{\rm delay,2} - \tau_{\rm delay,1}). \end{aligned} \quad (13)$$

Similarly, the continuum–line-emission cross terms are given by

$$\begin{aligned} C^{ec/ce}_{ll}(\Delta t) &= e \int d\tau_{\rm delay} \Psi(\tau_{\rm delay}) C^{cc}_{ll}(\Delta t \pm \tau_{\rm delay}) \\ &= s^2\, e \int d\tau_{\rm delay} \Psi(\tau_{\rm delay}) C^{cc}_{kk}(\Delta t \pm \tau_{\rm delay}) \end{aligned} \quad (14)$$

$$C^{ec/ce}_{lk/kl}(\Delta t) = e \int d\tau_{\rm delay} \Psi(\tau_{\rm delay}) C^{cc}_{kk}(\Delta t \pm \tau_{\rm delay}) \quad (15)$$

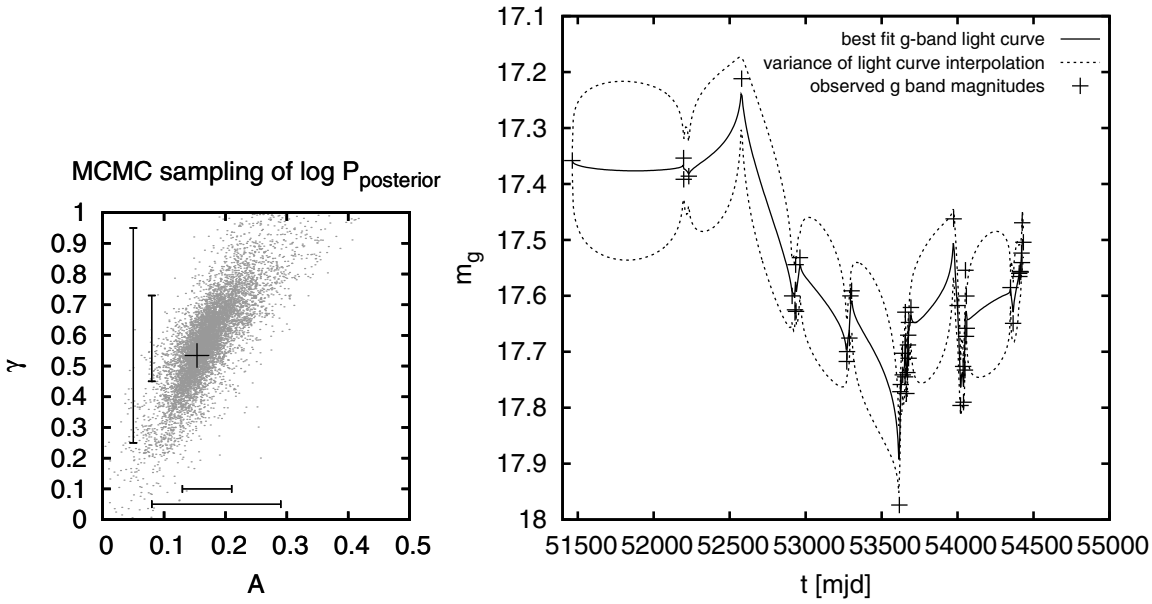

Figure 2. (a) Result of a structure-function model fit to the g-band light curve of the Stripe 82 quasar headobjid = 587731185126146081, Figure 1; for this object the g band reflects almost exclusively accretion disk emission. The posterior probability distribution (PDF) obtained through MCMC (Foreman-Mackey et al. 2012) is shown. The marginalized 68% and 90% confidence intervals for A and γ are indicated by horizontal and vertical bars. The cross marks maximum-at-posterior. (b) Result of the interpolation of continuum light curve (g band) for fit (Equation (A13)) for object headobjid = 587731185126146081, Figure 1, derived from the best fit (structure-function parameters at maximum at posterior) to the light curve's structure function. The solid line represents the best-fit mean model light curves from the power-law model. The area between the dashed lines reflects the variance for the light curve prediction, arising from the stochastic models; this variance reduces to the range of measurement errors at epochs where data exist (see Equation (A13)). These figures can be also found as part of Figure 4 in Section 4, which gives an overview about methodology and the output of the stochastic reverberation mapping algorithm.

where the $\pm$ refers to combinations in the sub- and superscripts of the left-hand side as $\pm$ and $C_{ll}^{cc} = s^2 C_{kk}^{cc}$, $C_{kl}^{cc} = s C_{kk}^{cc}$ as given by the flux model Equation (11).

Corresponding equations where the integrals are written out using a δ-function transfer function and the power-law model can be found in Appendix B at Equations (B1)–(B3). Figure 4 gives an overview on the usage of the different covariance matrices.

These terms can now be used to write the covariance matrix for the k-band continuum and l-band continuum plus emission line fluxes as

$$C = \begin{pmatrix} C_{kk}^{cc} & C_{kl}^{c,(e+c)} \\ C_{lk}^{(e+c),c} & C_{ll}^{(e+c),(e+c)} \end{pmatrix} \tag{16}$$

with

$$C_{kl}^{c,(e+c)} = C_{kl}^{ce} + C_{kl}^{cc} \tag{17}$$

$$C_{ll}^{(e+c),(e+c)} = C_{ll}^{cc} + C_{ll}^{ec} + C_{ll}^{ce} + C_{ll}^{ee}. \tag{18}$$

Using the covariance matrix as defined above, in Gaussian statistics the probability of some parameters (the structure function parameters and the time delay $\tau_{\rm delay}$) given the data (in flux units as we refer to flux here) can be computed, which yields a maximum likelihood approach $P(\mathbf{m}|\mathbf{p}) \propto \mathcal{L}(\mathbf{m}|\mathbf{p})$ (see Equation (A20)) where $\mathbf{p}$ are the model parameters (i.e., the structure-function parameters) and $(e, s, \tau_{\rm delay})$ where e and s are constrained spectroscopically. How this approach is carried out technically is shown in Appendix A and B.

To illustrate the typical shape of the probability distribution functions (PDFs), an example output is shown in Figure 3.

4.1. Parameter Estimation by MCMC

We chain the likelihoods, as we first analyze the continuum light curve on its own to estimate the structure-function parameters $\mathbf{p}_{\rm struc}$. Then we do a joint analysis of the continuum and emission line light curve using the values for the structure-function parameters estimated in the first step in order to estimate $\mathbf{p}_{\rm trans}$.

4.1.1. Estimating Structure Function Parameters

Estimation of the structure-function parameter is done by evaluating the logarithmic posterior probability distribution

$$\log P_{\rm posterior} = \log P(\mathbf{p}) + \log \mathcal{L}(\mathbf{m}|\mathbf{p}) \tag{19}$$

where $\mathbf{p} = \mathbf{p}_{\rm struc}$ are the structure function parameters and $\mathbf{m}$ are the measured light curve points. $\mathcal{L}(\mathbf{m}|\mathbf{p})$ is given by Equation (A20) and $P(\mathbf{p})$ represents the prior PDF of the structure-function parameters. In this equation the intrinsic variability of the data is described by a covariance matrix S, whereas the noise has a covariance matrix N. For estimation of the structure-function parameters, we use a data vector $\mathbf{m} \leftarrow \mathbf{f_k}$.

For a power-law model, we have

$$\log P(\mathbf{p}) = \log P(A) + \log P(\gamma), \tag{20}$$

where

$$P(A) \propto \begin{cases} \frac{1}{A}, & \text{if } 0 < A \leqslant 1 \\ 0, & \text{else} \end{cases} \tag{21}$$

$$P(\gamma) \propto \begin{cases} \frac{1}{1+\gamma^2}, & \text{if } 0 \leqslant \gamma \leqslant 1 \\ 0, & \text{else} \end{cases}. \tag{22}$$

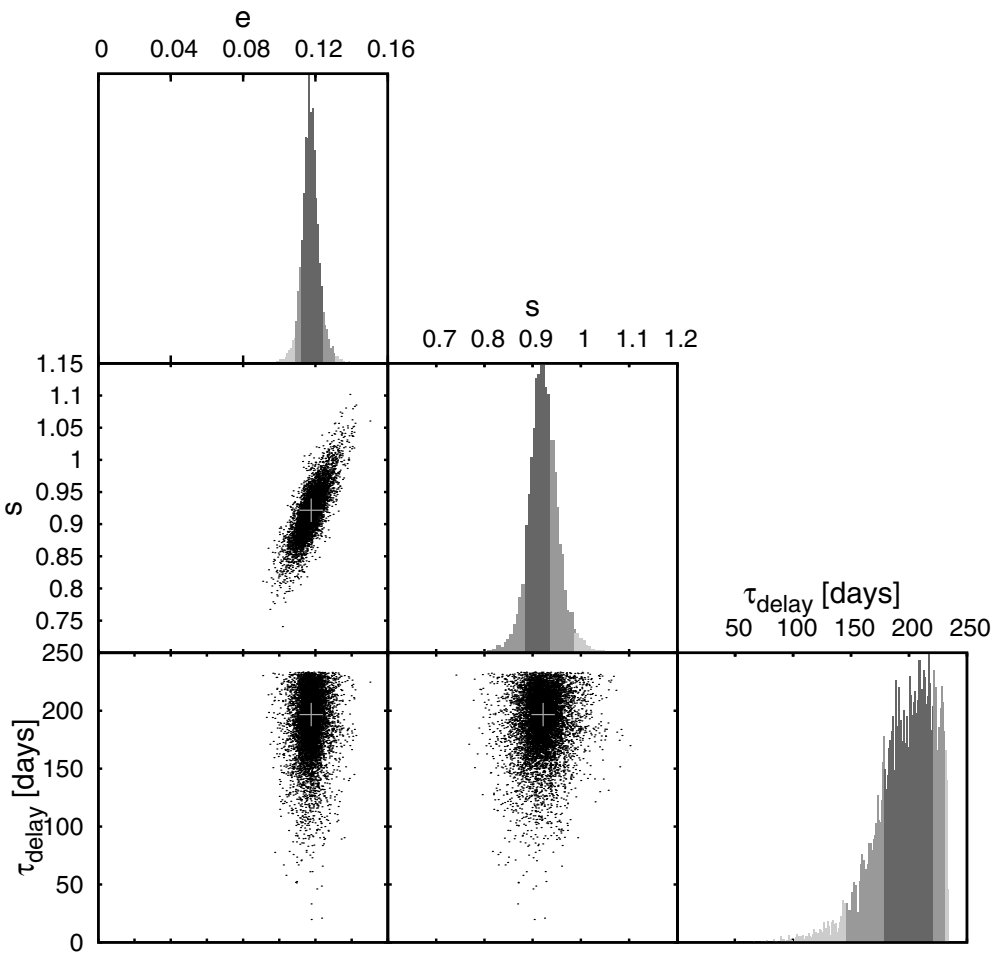

Figure 3. PDFs, represented in a triangle plot for the estimate of the reverberation delay $\tau_{\rm delay}$ for the quasar from Figure 1, derived from the simultaneous fit to the light curve that is in one band only continuum (g band), and in the other band (i band) a combination of continuum and delayed emission line flux (see Equation (23) in Appendix B). The figure shows an MCMC sampling of the PDF for the spectroscopically constrained emission-line fraction e and the emission line delay $\tau_{\rm delay}$, along with their marginalized 68% and 95% confidence regions (gray shading); cross marks maximum-at-posterior $\tau_{\rm delay,MAP} = 195.084$, $e_{\rm MAP} = 0.1176$

Thus we enforce our assumption that the power-law exponent γ, the logarithmic gradient of this mean change in magnitude, is positive and that the average variability on a 1 yr timescale is less than 1 mag.

Based on the tests described in Appendix C, we use the Affine Invariant MCMC Ensemble sampler (Foreman-Mackey et al. 2012) to explore the posterior probability distribution.

As a result of testing, for the estimation of the structure-function parameters and the mean magnitude $\bar{m}$, we use 10 walker,[5] up to 1000 iterations in a burn-in run, 200 iterations in a post-burn-in run, initialization $\mathbf{x}^{(0)} = (A^{(0)}, \gamma^{(0)}) = (0.1, 0.1)$. As $\bar{m}$ is an output parameter of the algorithm evaluating the likelihood function, it is not a component of the vector $\mathbf{x}$.

4.1.2. Estimating the Time Delay

The estimation of the time delay is done by evaluating the logarithmic posterior probability distribution

$$\begin{aligned}\log P_{\rm posterior} &= \log P(\mathbf{p}_{\rm trans}) + \log(\mathcal{L}(\mathbf{m}|\mathbf{p}_{\rm trans})) \\ &= \log P(\tau_{\rm delay}, e, s) + \log \mathcal{L}(\mathbf{m}_x, \mathbf{m}_y|\tau_{\rm delay}, e, s).\end{aligned} \quad (23)$$

$\mathcal{L}(\mathbf{m}|\mathbf{p}_{\rm trans})$ is given by (A20) and $P(\tau_{\rm delay}, e, s)$ represents the prior PDF of the transfer function parameters.

$P(\tau_{\rm delay}, e, s)$ consists of a prior on the time delay, $P(\tau_{\rm delay})$, and a prior on (e, s). The prior on the time delay is given by

$$P(\log_{10}\tau_{\rm delay}) \propto \begin{cases} \frac{1}{\sqrt{2\pi}} \exp\left[-\frac{(\log_{10}\tau_{\rm delay} - \log_{10}\tau_{\rm delay,0})^2}{\log_{10} 2}\right], \\ \quad \text{if } 0.25 \times \tau_{\rm delay,0} < \tau_{\rm delay} < 4 \times \tau_{\rm delay,0} \\ 0, \qquad \text{else} \end{cases} \quad (24)$$

$\tau_{\rm delay,0}$ is set to the time delay inferred from the Kaspi relation Equation (40) if $\lambda L_\lambda(5100\ \text{Å})$ is available, and from the virial assumption otherwise.

For the virial mass estimates, it has been assumed (Vestergaard & Peterson 2006) that the BLR is virialized, the continuum luminosity is used as a proxy for the BLR radius, and the broad-line width (FWHM or line dispersion) is used as a proxy for the virial velocity. The virial mass estimate is then expressed as

$$\log\left(\frac{M_{\rm BH,vir}}{M_\odot}\right) = a + b\log\left(\frac{\lambda L_\lambda}{10^{44}\text{erg s}^{-1}}\right) + 2\log\left(\frac{\text{FWHM}}{\text{km s}^{-1}}\right), \quad (25)$$

where the coefficients a and b are empirically calibrated against local AGNs with RM masses, or internally among different

[5] A detailed description of this term and the algorithm can be found in Foreman-Mackey et al. (2012).

lines. This results in an expected rest-frame delay of

$$\tau_{\mathrm{delay},0} = (1+z)\cdot 10^{\mathrm{LOGBH}}\cdot \frac{5.121039}{\mathrm{FWHM\_BROAD\_HB}^2} \text{ lightdays}. \quad (26)$$

LOGBH and FWHM_BROAD_HB are the logarithmic virial M_{BH} and FWHM of broad Hβ (km s^{-1}), respectively, from the Catalog of Quasar Properties from SDSS DR7 (Shen et al. 2011).

How (e, s) can be constrained by a prior depends much on the information that is available beside the photometric data. In the case of the SDSS S82 data, spectroscopic data are used to constrain (e, s).

As we assume the flux model (11), we need to know which part of flux in the l band belongs to the continuum and which is emission line contribution. From the spectrum, we can get some information on e and s, as

$$e \approx \frac{1}{f_k}\int_l f_e(\lambda)\omega_l(\lambda)\,d\lambda \quad (27)$$

$$s = \frac{1}{f_k}\int_l f_c(\lambda)\omega_l(\lambda)\,d\lambda. \quad (28)$$

with

$$f_k = \int_k f_k(\lambda)d\lambda \quad (29)$$

and $\omega_l(\lambda)$: filter curve in the l band, normalized so $\int \omega_l(\lambda)d\lambda = 1$, $\mathrm{EW} = \int (f_l^e(\lambda) - f_l^c(\lambda))/f_l^c(\lambda)d\lambda$: equivalent width of the line.

A fit for the emission line and the continuum has to be done to get f_l^e and the continuum, $f_l^c \approx f_l - f_l^e$. The emission line is fitted as a Gaussian, using the provided $\mathrm{FWHM}_{\mathrm{line}}$ and the continuum level at the emission line, $f_l^c(\lambda_{\mathrm{line,obs}})$,

$$f_l^e(\lambda) = (f_l(\lambda_{\mathrm{line,obs}}) - f_l^c(\lambda_{\mathrm{line,obs}}))\cdot \exp\left(-\frac{(\lambda-\lambda_{\mathrm{line,obs}})^2}{2\sigma^2}\right) \quad (30)$$

with

$$\sigma = 2.35\ \mathrm{FWHM}_{\mathrm{line,obs}}. \quad (31)$$

For the continuum level, we use the approximation

$$f_{\mathrm{cont}}(\lambda_{\mathrm{line,obs}}) = \frac{f_{\mathrm{left}} + f_{\mathrm{right}}}{2} \quad (32)$$

$$= \frac{1}{2}\left(f\left(\lambda_{\mathrm{line,obs}} - \frac{\mathrm{EW_{obs}}}{2}\right) + f\left(\lambda_{\mathrm{line,obs}} + \frac{\mathrm{EW_{obs}}}{2}\right)\right). \quad (33)$$

Applying this to (27) and (28) gives initial values (e_0, s_0). We are now able to predict an equivalent width from an (e, s) and compare it to the observed one,

$$\mathrm{EW_{pred}}(t) = \frac{e}{s}\frac{\int f_{\mathrm{line}}(\lambda)(t-\tau_{\mathrm{delay}})d\lambda}{\int f_{\mathrm{line}}(\lambda)(t-\tau_{\mathrm{delay}})\omega(\lambda)d\lambda} \quad (34)$$

where

$$f_{\mathrm{line}}(\lambda)(t) = a(t)\cdot f_{\mathrm{line}}(\lambda)(t_0) \quad (35)$$

with t_0 as the time the spectrum was taken. Because we assume e and s to be constant over time,

$$a(t) = \frac{f(t)}{f(t_0)} = \frac{f(m_x(t))}{f_x(t_0)}, \quad (36)$$

interpolation of the light curve in the continuum-only band x has to be done. We are now able to predict an equivalent width from some (e, s) and compare it to the observed one at the time t_0 the spectrum was taken. From this, with $\mathrm{EW_{pred}} \equiv \mathrm{EW_{pred}}(t_0)$, one gets the likelihood term

$$L_{\mathrm{spec}} \propto \frac{1}{\sqrt{2\pi}\delta\mathrm{EW_{obs}}}\exp\left(-\frac{(\mathrm{EW_{obs}} - \mathrm{EW_{pred}})^2}{2\delta EW_{\mathrm{obs}}^2}\right), \quad (37)$$

where $\delta\mathrm{EW_{obs}}$ is measurement uncertainty in the equivalent width of the observed emission line. In our application to SDSS S82 data, observed equivalent widths $\mathrm{EW_{obs}}$ are retrieved from the Catalog of Quasar Properties from SDSS DR7 (Shen et al. 2011).

Equation (37) is multiplied with the previous likelihood term (10) to describe the likelihood of the model parameter $\mathbf{p}$ given the data $\mathbf{m}$. In this equation, the intrinsic variability of the data is described by a covariance matrix S, whereas the measurement uncertainties have a covariance matrix N. For estimation of the time delay from one emission line, we use a data vector $\mathbf{m} \leftarrow (\mathbf{f_k}, \mathbf{f_l})$.

Light curve de-trending is applied through the response matrix L. Basically, if we have two light curves with a possible offset in their means, we can use separate means for each, $(L_{i1}, L_{i2}) = (1, 0)$ for the continuum light curve f_k and $(L_{i1}, L_{i2}) = (0, 1)$ for the light curve containing a continuum and emission line contribution f_l.

As mentioned in some papers referring to the basic approach of this algorithm, (e.g., Zu et al. 2011), the response matrix L can also be used to describe and remove a general trend in the light curve, which is called de-trending. De-trending has been shown to considerably improve reverberation mapping because removing a general linear trend in the light curve so better realizes the limit of stationary light curves (e.g., Welsh 1999). After some tests, for de-trending f_k and f_l, we decided to use $(L_{i1}, L_{i2}) = (t_i, 0)$ and $(L_{i1}, L_{i2}) = (0, t_j)$, respectively.

Figure 4 summarizes the methodology and output of the stochastic reverberation mapping algorithm.

Based on the tests described in Appendix C, we use the Affine Invariant MCMC Ensemble sampler (Foreman-Mackey et al. 2012) to explore the posterior probability distribution.

For the estimation of τ_{delay}, s, e, we use 15 walker, up to 2000 iterations in a burn-in run, 800 iterations in a post-burn-in run, initialization $\mathbf{x}^{(0)} = (s^{(0)}, e^{(0)}, \tau_{\mathrm{delay}}^{(0)})$, where $s^{(0)}$, $e^{(0)}$, $\tau_{\mathrm{delay}}^{(0)}$ depends on the current light curve. The start position of the walkers is $x^{(0)} + r$, where r is some random number, so the walkers start in a small area in parameter space around $x^{(0)}$.

5. QUASAR SPECTROSCOPY AND LIGHT CURVES IN THE SDSS STRIPE 82

The SDSS (York et al. 2000) provides homogeneous and deep ($r < 22.5$) photometry in five passbands (*ugriz*), typically for more than 60 epochs of observations over a decade in a 290 deg^2 area of the Southern Galactic cap known as S82, (Frieman et al. 2008; Annis et al. 2014; Ivezić et al. 2012). These photometry epochs were obtained in early seasons of about 2–3 months, effectively sampling timescales from days to years.

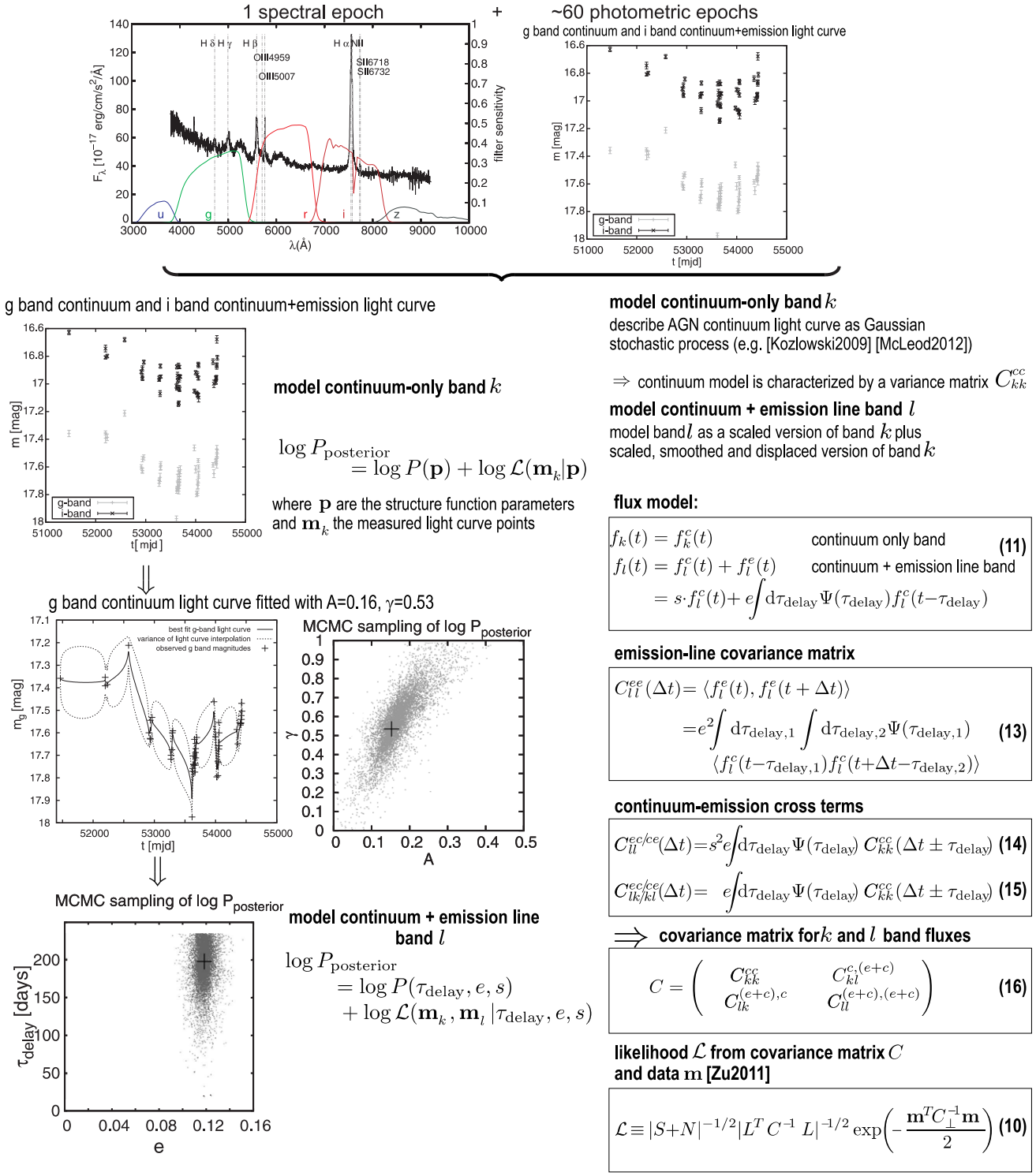

Figure 4. Methodology of stochastic reverberation mapping illustrated using the example of light curve headobjid = 587731185126146081, with $z = 0.1506$, continuum-only band k: g band, continuum+emission line band l: i band with strong Hα.

The photometric data for the *ugriz* bands are simultaneous, and an example of such a light curve (only two bands are plotted) is shown in Figure 1. This area of SDSS is also exceptional in that it has complete spectroscopic quasar identification (Shen et al. 2011), resulting in a sample of 9,156 quasars, with spectra. Additional information on these quasars exists in the Catalog of Quasar Properties from SDSS DR7 (Shen et al. 2011).

Until the first data release of LSST, this S82 data set, with its combination of single epoch spectra and multi-band light-curves for 10^4 quasars (see also Figure 1), is the best data set to carry out broadband reverberation mapping. It is the same data set that was used by Schmidt et al. (2010).

The data are all publically accessible through the SDSS data archive.[6] For our application, all light curves have been cleaned of manifest outliers by simply considering measurements having a magnitude error of $\geqslant$0.1, and removing them. To obtain further

[6] http://casjobs.sdss.org/CasJobs/default.aspx

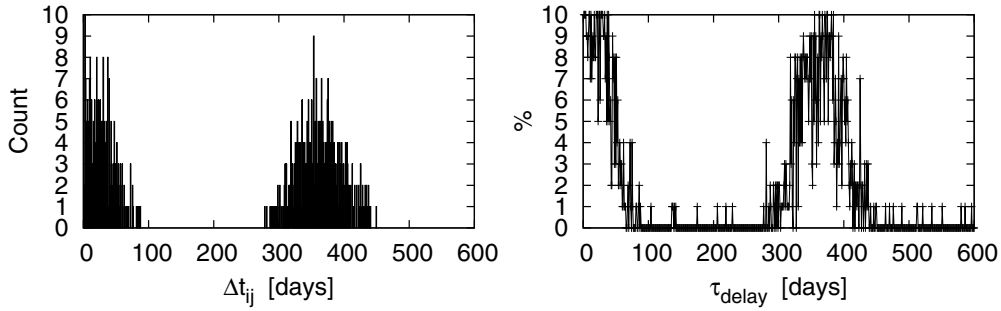

(a) (b)

Figure 5. (a) Histogram of the observational time lags (first 600 days) in the light curve (differences between the data points); total observational period: 2959 days, (b) percentage recovered ±1 day vs. $\tau_{\rm delay}$ from mock light curves with the time sampling resulting in observational time lags from figure (a); crosses mark the evaluated lags, lines are displayed to guide the eye.

information on each individual quasar, such as for instance equivalent widths or values needed for calculating a prior on the size of the broadline region as described in Section 4.1.2, Equation (24), we cross-matched the list of objects from SDSS S82 with the Catalog of Quasar Properties from SDSS DR7[7] (Shen et al. 2011).

We linked the spectra, light curves, and additional information from DR7 by requiring a positional match of ∼1. For 9,120 light curves from SDSS S82, a unique corresponding entry was found in the DR7 Quasar Properties Catalog. No match was found for the remaining 36 light curves. There were no double matches.

For the subsequent analysis, we converted all light curve measurements to linear fluxes rather than magnitudes. To get the flux f_k in the specific band k in units of erg s^{-1} cm^{-2}, the effective bandpass width $w_{\lambda,k}$ has to be taken into account, resulting in

$$f_k(t) = 3631 \times 10^{-23} \frac{2 b_k c}{w_{\lambda,k}} \times \sinh\left(-\frac{m_k(t)\log(10)}{2.5} - \log(b_k)\right) \text{ erg s}^{-1}\text{cm}^{-2}. \quad (38)$$

Not all of the 9156 quasars in the sample are comparably suitable for broadband reverberation mapping. Mock data analyses (see Appendix C.2) have shown that two conditions need to be satisfied: a redshift interval where one band has important emission line contributions, while another band is free of them; sufficiently many photometric epochs; in S82 they range from 2 to 160, with a median of 66.

To identify suitable redshift ranges that maximize continuum-line contrast between two different bands, we considered the Hα, Hβ, Mg II lines for reverberation mapping and the C IV, N II λ6585, S II λ6718, S II λ6732, O III λ4959, O III λ5007, Lyα, Lyβ, C III], Fe II λ2382, Fe II λ2600, Hγ, Hδ lines as contaminants, with the data taken from Table 2 in Vanden Berk et al. (2001). To check whether or not a line falls into a band, we defined the limits of a band as the wavelength where the neighboring filters have transmission of zero. This results in relatively narrow redshift ranges having only one out of Hα, Hβ, Mg II in one band (the continuum+emission line band) and at least one other band free of all of them. There redshift ranges are summarized in Table 1.

[7] The catalog is available at https://users.obs.carnegiescience.edu/yshen/BH_mass/dr7.htm.

Within these redshift ranges, we identify quasars whose light-curve sampling is relatively good, because this has great influence on the possibility of estimating a certain time delay $\tau_{\rm delay}$. In evenly sampled data the sampling rate must be higher than the (expected) time delay. In unevenly sampled data there must be at least some time intervals smaller than or equal to the (expected) time delay.

We illustrate this in Figure 5 by generating mock light curves within the actual S82 time sampling, but varying $\tau_{\rm delay}$. By applying the likelihood approach described in Section 4, Equations (23), and (19), we then tried to recover the delay $\tau_{\rm delay}$ used for generating the light curves before.

In its left panel, Figure 5 shows a histogram of the time-intervals between SDSS S82 observational epochs of one example light curve, illustrating the possible time-delays that are covered by the data. The right-hand panel shows the percentage of light curves out of this sample (10 light curves per $\tau_{\rm delay}$) for which $\tau_{\rm delay}$ can be recovered within ± one day. The allowed difference of one day was chosen to prevent a larger absolute error for objects having larger $\tau_{\rm delay}$. The test data used for this have the same time sampling and structure function parameters, but are light curves of different objects. The values of e and s of our mock data were set to $e = 0.2$, $s = 1.0$. As a transfer function, we used a δ function. Due to the way test data were generated, no line EW was set. (For details on test data, see Appendix C.) Here "recovered" is meant the sense of the value at maximum at posterior. A comparison of the two panels shows that time delays that match common epoch differences in S82 (left panel) can be well recovered. This makes the histogram of observational time lags a very useful tool to quickly estimate whether the expected time delay should be recoverable, given the time sampling of the light curve in case. These histograms differ among the light curves in S82, as there are common time sampling windows due to the SDSS, but the exact sampling and the number of time lags available differs.

6. RESULTS

With the analysis tools from the previous section in place, we now proceed to estimate time delays for subsets of the S82 data, which can be compared to relations for $R_{\rm BLR}$ from Kaspi et al. (2000) and Bentz et al. (2013), and relations for $M_{\rm BH}$ from Vestergaard (2002).

Given then small, expected signal and the difficulties with the S82 time sampling, it was useful to not focus on the $\tau_{\rm delay}$ estimates of individual objects, but to presume that there is a $R_{\rm BLR}(L)$ relation, and determine its scaling normalization

Table 1
Emission Lines

redshift	g	r	i	z
0.08	Hβ, Hγ (plus some other)	Continuum	-	Continuum
0.13–0.142	Continuum	Continuum	Hα (plus some other)	Continuum
0.225–0.283	Continuum	Hβ, Hγ (plus some other)	Continuum	Continuum
0.284–0.291	Continuum	Hβ, Hγ (O III λ4959, λ5007)	Continuum	-
0.349–0.371	Continuum	Continuum	Continuum	Hα (plus some other)
0.463	Continuum	Continuum	-	Hα (plus some other)
0.519–0.537	Continuum	Continuum	Hβ, Hγ (plus some other)	Continuum
0.538–0.552	Mg II	Continuum	Hβ, Hγ (O III λ4959, λ5007)	Continuum
0.553–0.554	Mg II	Continuum	-	Continuum
0.555–0.591	Mg II	Continuum	Continuum	Continuum
0.592–0.732	Mg II (Fe II λ2600)	Continuum	Continuum	Continuum
0.733–0.813	Mg II (Fe II λ2600)	Continuum	Continuum	-
0.814–0.846	Mg II (Fe II λ2600)	Continuum	Continuum	Hβ, Hγ (plus some other)
0.847–0.851	-	Continuum	Continuum	Hβ, Hγ (O III λ4959, λ5007)
1.171–1.191	Continuum	Mg II	Continuum	Continuum
1.192–1.207	Continuum	Mg II	Continuum	Continuum
1.765–1.786	C VI	Continuum	Continuum	Continuum
1.787–1.912	C VI	Continuum	-	Continuum
1.913–2.036	C VI	Continuum	Continuum	Continuum
2.037–2.185	C VI (Si VI)	Continuum	Continuum	Continuum
2.186–2.254	C VI (Si VI)	-	Continuum	Continuum
2.255–2.32	C VI (Si VI)	Continuum	Continuum	Continuum
2.903–2.969	-	C VI	Continuum	Continuum

Notes. In a compact form this table lists which emission lines can be used for a given redshift and in which cases there is more than one emission line in a band. "-" indicates that this band cannot be used (a continuum and some line contribution from a line that is not used as an emission line for reverberation mapping). Sometimes there is an emission line that can be used, but also (weak) contribution from other lines, those are written in brackets.

in different redshift (and hence luminosity) regimes, by jointly modeling several light curves.

Previous reverberation mapping studies show a simple relationship between the size of the BLR and the corresponding continuum luminosity L of the form $R_{\rm BLR} \propto L^{\gamma}$ (Kaspi et al. 2000). This is an important result because it provides a secondary method of estimating the central black hole masses by using L as proxy for $R_{\rm BLR}$. This makes it a powerful tool for mass estimation in large ensembles, since a single AGN spectrum yields both L and a line width ΔV suitable for estimating the size of the broad-line region by using L^{γ} and then estimating $M_{\rm BH}$ by applying Equation (1). The AGN sample evaluated in this study allows us to readdress the issue of the $R_{\rm BLR} - L$ and $R_{\rm BLR} - M_{\rm BH}$ relations in AGNs.

We present novel empirical relationships for estimating the BLR sizes in AGNs developed using multi-epoch photometry combined with single-epoch spectroscopy. The found that scaling relationships between line widths and luminosity are based on empirical relationships between the BLR size and luminosities in various bands by Kaspi et al. (2000), Bentz et al. (2013), and Vestergaard (2002). To obtain more definite results on the $R_{\rm BLR} - L$ and $M_{\rm BH} - L$ relations, we evaluate well-defined subsamples of reverberation-mapped AGN, as shown in the Tables 2–5.

The redshift requirements combined with the strength and S/N of the emission lines make the following redshift ranges most suitable: $z = 0.225$–0.291 (with 43 light curves), $z = 0.555$–0.591 (with 118 light curves), $z = 0.592$–0.846 (with 746 light curves).

Not all light curves of the 9,156 spectroscopically confirmed SDSS S82 quasars (see Schmidt et al. 2010; Schneider et al. 2007) can be evaluated, mostly due to inappropriate time sampling with respect to the expected time delay. The expected time delay is estimated from the Kaspi relation (40) if the rest frame 5100 Å luminosity is available, or from the virial assumption based on the FWHM of the Hβ (25) line otherwise. We found that 35 out of the 43 light curves at $z \sim 0.25$, 69 at $z \sim 0.57$, and 290 at $z \sim 0.6 - 0.85$ have reasonable epoch coverage.

To compare ensemble results to known mass–luminosity relations, we have to omit light curves. Specifically, light curves resulting in an unreliable posterior probability distribution were excluded from the samples. For ensemble estimates of black hole masses, we set a prior cutoff at $\tau_{\rm delay}/\tau_{\rm delay,expected} = 4$, and omitted the light curve where the individual mass estimates posterior PDF are increasing toward this cutoff or are flat. We base our study on the 323 AGNs for which we can calculate reliable reverberation-based $R_{\rm BLR}$ estimates. For comparison, earlier studies used much fewer objects (e.g., Kaspi et al. 2000 based on 17 QSOs and Vestergaard 2002 based on 32 AGNs), which were mostly at lower redshifts.

Tables 2–5 present detailed information about the four subsamples used for determining the $R_{\rm BLR} - L$ and $M_{\rm BH} - L$ relations and the results of individual objects. Throughout this paper, we use the `headobjid` to identify individual objects.

In the following, we present our results using a power-law structure function with posterior given by Equation (20) and assuming a δ-function transfer function where the posterior is given by Equation (23). We restrict ourselves to the power-law structure function, as we have found it to produce less covariance between the $\tau_{\rm delay}$ estimates and the structure-function parameters. Both from real and mock data, we found that using the DRW model is not successful for application to reverberation mapping of SDSS S82 light curves. During testing (with mock light curves), it came out that fitting with the DRW lead to very imprecise estimates for $\tau_{\rm delay}$, even with the given

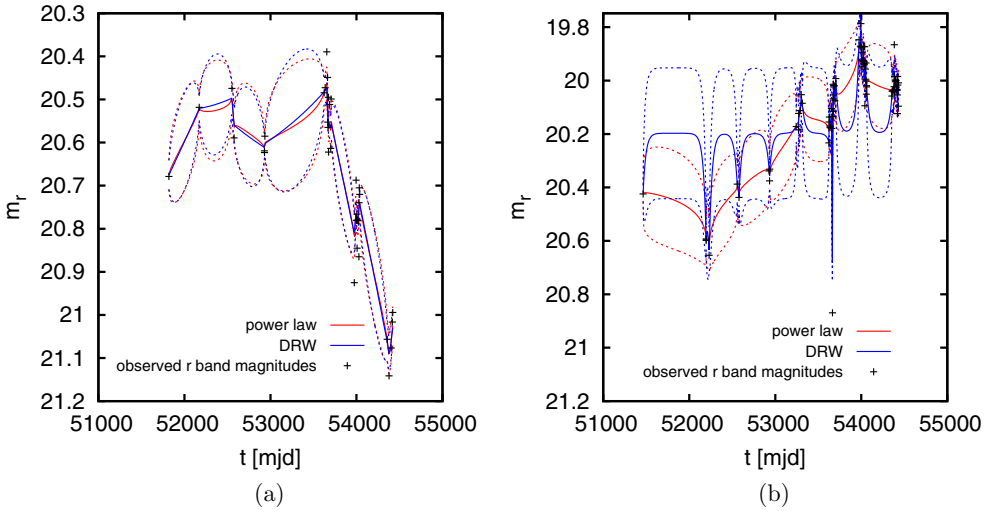

Figure 6. Result of the interpolation of continuum light curve (r band) for DRW and power law for (a) object headobjid = 587730845814686076, (b) object headobjid = 587731186724373007, derived from the best fit (structure-function parameters at maximum at posterior) to the light curve's structure function. The solid line represents the best-fit mean model light curves. The area between the dashed lines reflects the variance for the light curve prediction, arising from the stochastic models. In most cases the two functional forms lead to very similar interpolations like in (a), but in a modest number of cases the DRW provides an unsatisfying fit as in (b). This makes light-curve interpolation on the basis of power-law structure functions more robust for this context.

priors. This is because the estimation of the fit parameters does not work very well for sparsely sampled data because the fit parameters ω and τ of the structure function indicate the intrinsic variance of the process (ω^2) and the damping timescale (τ), which cannot be estimated well when having sparsely sampled data. However, the power-law model works very well in this case, because the amplitude A quantifies the root-mean-square magnitude difference on a 1 yr timescale and γ is the logarithmic gradient of this mean change in magnitude, which is easier to estimate. For many SDSS S82 quasar light curves, the shape of the fitted light curve differs considerably between the power law and the DRW model, because the DRW leads to a fit that is less smooth than that from the power law, and shows too much sensitivity to outliers in many cases. For comparison, the power law and DRW model fits for two light curves are shown in Figure 6.

6.1. Individual and Ensemble Estimates of BLR Sizes

Caution must be exercised when using time lag estimates to calculate the size of broad-line regions. It is the fact that for some objects, different reverberation mapping campaigns state different values for $\tau_{\rm delay}$. The implementation of corrections (e.g., modeling the variation of the spectrum over time) is beyond the scope of this paper. We convert the computed observer-frame time delays $\tau_{\rm delay,obs}$ directly into BLR sizes after applying a cosmological $(1+z)^{-1}$ factor, so

$$R_{\rm BLR} = c\,\tau_{\rm delay,obs}(1+z)^{-1}. \quad (39)$$

Individual $R_{\rm BLR}$ for the members of our subsamples are listed in Tables 2–5.

To define $R_{\rm BLR}$–L relations, we follow Kaspi et al. (2000) and Bentz et al. (2013), using $\lambda L_\lambda(5100\,\text{Å})$ as our luminosity measure. Kaspi et al. (2000) found for the BLR size-luminosity relation for the Hα line

$$R_{\rm BLR,Kaspi} = \left(32.0^{+2.0}_{-1.9}\right)\left(\frac{\lambda L_\lambda(5100\ \text{Å})}{10^{44}\ \text{erg s}^{-1}}\right)^{0.700\pm0.033}\ \text{light days}, \quad (40)$$

which was updated by Bentz et al. (2013) as

$$R_{\rm BLR,Bentz} = \left(33.651^{+2.490}_{-2.318}\right)\left(\frac{\lambda L_\lambda(5100\ \text{Å})}{10^{44}\ \text{erg s}^{-1}}\right)^{0.533^{+0.035}_{-0.033}} \times\ \text{light days}. \quad (41)$$

For the relationships, we adopt the simple form $R_{\rm BLR} \propto R_{\rm BLR,Kaspi}$ and $R_{\rm BLR} \propto R_{\rm BLR,Bentz}$, where $R_{\rm BLR,Kaspi}$ and $R_{\rm BLR,Bentz}$ are the estimates from Kaspi and Bentz, respectively. So we do not determine a new slope, but only a new proportionality constant.

We calculated the individual posterior PDFs by evaluating Equation (23) and introducing $R_{\rm BLR,Kaspi}$ as a prior using Equation (24). We then projected these individual PDFs as histograms, and marginalize over the flux scaling factors e and s. We assume that $\tau_{\rm delay}/\tau_{\rm delay,exp} = f(L, z, \text{EW}_{\rm line})$, this marginalization was done for different cases:

For comparing to the relations (40) and (41), we did binning by z according to our subsample Tables 2–5. We also binned by luminosity $\lambda L_\lambda(5100\,\text{Å})$. We evaluated 29 light curves in the redshift range $z = 0.225$–0.291, with i band: Hα, z band: continuum. Seventeen light curves out of this range were also evaluated with r band: Hβ, Hγ (plus some other), g band: continuum. We evaluated 68 light curves in the redshift range $z = 0.555$–0.591 with g-band Mg II, r: continuum. We evaluated 111 light curves in the redshift range $z = 0.592$–0.6999, with g-band Mg II (Fe II λ2600), r continuum. The redshift range $z = 0.7$–0.846 was evaluated with g-band Mg II (Fe II λ2600), r continuum for 115 light curves.

In Figures 7(a)–(e), we show the marginalized posterior probability distributions for comparing the ensemble $R_{\rm BLR}$ to the Kaspi relation for z-binned samples. For each sample the redshift, emission lines, and band used for continuum are given.

In Figures 8(a)–(d) we show the deviations of our ensemble $R_{\rm BLR}$ estimates from those of the Kaspi and Bentz relations as a function of z and L. Our results show ensemble estimates about 1.7 times larger than those from the scaling relations by Kaspi and Bentz. There is no correlation between e and $\tau_{\rm delay}$. The typical shape of the PDF is shown in Figure 3.

Table 2
Sample 1 Properties and Reverberation Mapping Results $z = 0.225$–0.291, with i Band: Hα, z Band: Continuum

Object[a]	z[b]	EW(Hα)/Å[c]	$\frac{\mathrm{FWHM(H}\beta)}{1000\ \mathrm{km\ s^{-1}}}$ [d]	$\log\left[\frac{\lambda L_\lambda(5100\ \text{Å})}{\mathrm{erg\ s^{-1}}}\right]$	$\frac{R_{\mathrm{BLR,Kaspi}}}{\mathrm{lightdays}}$ [e]	$\frac{R_{\mathrm{BLR}}}{\mathrm{lightdays}}$ [f]
587731172234231820	0.2351	247 ± 9	$5.0 \times 10^3 \pm 1.4 \times 10^2$	44.182 ± 0.003	43^{+4}_{-3}	$1.3 \times 10^2\ ^{+63}_{-1.2 \times 10^2}$
587731172768874535	0.2675	$2.0 \times 10^2 \pm 11$	$5.8 \times 10^3 \pm 3.1 \times 10^2$	44.264 ± 0.005	49^{+5}_{-4}	$8.2 \times 10^2\ ^{+1.4 \times 10^2}_{-68}$
587731174382370829	0.2332	$2.6 \times 10^2 \pm 10$	$5.2 \times 10^3 \pm 2.8 \times 10^2$	44.244 ± 0.006	48^{+4}_{-4}	$55\ ^{+1.6 \times 10^2}_{-25}$
587731174382370953	0.2814	$1.7 \times 10^2 \pm 37$	$2.1 \times 10^3 \pm 6.0 \times 10^2$	44.210 ± 0.004	45^{+4}_{-4}	$48^{+1.5 \times 10^2}_{-35}$
587731185660264483	0.2509	$1.6 \times 10^2 \pm 36$	$5.3 \times 10^3 \pm 1.1 \times 10^3$	43.88 ± 0.02	26^{+2}_{-2}	$65\ ^{+54}_{-53}$
587731186203361389	0.279	176 ± 8	$3.7 \times 10^3 \pm 4.9 \times 10^2$	44.33 ± 0.008	54^{+6}_{-5}	$62\ ^{+1.9 \times 10^2}_{-47}$
587731186207031353	0.2519	$2.4 \times 10^2 \pm 31$	$6.3 \times 10^3 \pm 2.5 \times 10^2$	44.410 ± 0.006	62^{+7}_{-6}	$53^{+2.3 \times 10^2}_{-35}$
587731186734203087	0.2648	217 ± 8	$3.7 \times 10^3 \pm 1.8 \times 10^2$	44.199 ± 0.004	44^{+4}_{-3}	$40^{+1.6 \times 10^2}_{-28}$
587731186735644691	0.257	266 ± 4	$2.4 \times 10^3 \pm 2.3 \times 10^2$	44.360 ± 0.004	57^{+6}_{-5}	$93^{+1.7 \times 10^2}_{-76}$
587731187260784863	0.2812	$2.5 \times 10^2 \pm 12$	$2.2 \times 10^3 \pm 2.0 \times 10^2$	44.11 ± 0.01	38^{+3}_{-3}	$44\ ^{+1.3 \times 10^2}_{-33}$
587731187276841126	0.2728	$2.2 \times 10^2 \pm 17$	$1.2 \times 10^4 \pm 1.7 \times 10^3$	44.163 ± 0.006	41^{+4}_{-3}	$48\ ^{+1.4 \times 10^2}_{-36}$
587731187806830737	0.2639	$1.2 \times 10^2 \pm 27$	$1.6 \times 10^3 \pm 2.9 \times 10^2$	44.124 ± 0.008	39^{+3}_{-3}	$56\ ^{+1.2 \times 10^2}_{-44}$
587731187815481439	0.2868	$3.1 \times 10^2 \pm 1$	$5.6 \times 10^3 \pm 3.4 \times 10^2$	44.273 ± 0.008	50^{+5}_{-5}	$64\ ^{+1.6 \times 10^2}_{-49}$
587731187817381938	0.2728	$3.5 \times 10^2 \pm 12$	$3.8 \times 10^3 \pm 3.8 \times 10^2$	44.166 ± 0.008	42^{+4}_{-3}	$45\ ^{+1.4 \times 10^2}_{-33}$
587731511544774775	0.2811	$1.04 \times 10^2 \pm 11$	$4.9 \times 10^3 \pm 2.2 \times 10^3$	44.184 ± 0.003	43^{+4}_{-3}	$47^{+1.5 \times 10^2}_{-34}$
587731511548379306	0.2865	$1.6 \times 10^2 \pm 17$	$3.2 \times 10^3 \pm 3.3 \times 10^2$	44.130 ± 0.003	39^{+3}_{-3}	$42\ ^{+1.4 \times 10^2}_{-31}$
587731512614977609	0.2616	396 ± 4	$3.3 \times 10^3 \pm 78$	45.3258 ± 0.0007	$2.7 \times 10^2\ ^{+47}_{-41}$	$1.8 \times 10^2\ ^{+1.3 \times 10^2}_{-1.6 \times 10^2}$
587731514219036709	0.2915	$3.8 \times 10^2 \pm 15$	$5.0 \times 10^3 \pm 1.2 \times 10^2$	44.332 ± 0.003	55^{+5}_{-4}	$62\ ^{+1.9 \times 10^2}_{-46}$
587731514227818645	0.2578	$2.1 \times 10^2 \pm 10$	$4.9 \times 10^3 \pm 3.4 \times 10^2$	44.232 ± 0.004	47^{+4}_{-3}	$1.5 \times 10^2\ ^{+63}_{-80}$
587734303268077643	0.2878	$1.6 \times 10^2 \pm 25$	$1.9 \times 10^4 \pm 3.2 \times 10^2$	44.244 ± 0.006	47^{+4}_{-4}	$52\ ^{+1.6 \times 10^2}_{-39}$
587734304875020616	0.283	$2.4 \times 10^2 \pm 13$	$1.6 \times 10^3 \pm 2.2 \times 10^2$	44.342 ± 0.003	56^{+5}_{-5}	$65\ ^{+1.9 \times 10^2}_{-50}$
587734304876331060	0.2713	135 ± 5	$4.9 \times 10^3 \pm 2.2 \times 10^2$	44.370 ± 0.004	59^{+6}_{-5}	$5\ ^{+1.9 \times 10^2}_{-58}$
587734305416413205	0.2276	$2.2 \times 10^2 \pm 15$	$4.6 \times 10^3 \pm 3.1 \times 10^2$	44.155 ± 0.004	41^{+3}_{-3}	$23\ ^{+1.6 \times 10^2}_{-11}$
588015508208222443	0.2692	$1.2 \times 10^2 \pm 13$	$7.2 \times 10^3 \pm 2.1 \times 10^3$	44.318 ± 0.006	53^{+5}_{-5}	$68\ ^{+1.7 \times 10^2}_{-53}$
588015508213203014	0.2466	210 ± 9	$1.1 \times 10^4 \pm 8.3 \times 10^2$	44.313 ± 0.007	53^{+5}_{-5}	$41\ ^{+2.0 \times 10^2}_{-25}$
588015508736901262	0.242	197 ± 5	$5.7 \times 10^3 \pm 3.7 \times 10^2$	44.190 ± 0.004	43^{+4}_{-3}	$74\ ^{+1.2 \times 10^2}_{-62}$
588015509277376527	0.2386	353 ± 5	$3.9 \times 10^3 \pm 1.9 \times 10^2$	44.438 ± 0.009	65^{+7}_{-7}	$94\ ^{+1.3 \times 10^2}_{-75}$
588015509807759391	0.2738	$1.8 \times 10^2 \pm 12$	$5.5 \times 10^3 \pm 3.4 \times 10^2$	44.147 ± 0.005	41^{+3}_{-3}	$45\ ^{+1.4 \times 10^2}_{-33}$
588015509829451922	0.2369	102 ± 3	$6.7 \times 10^3 \pm 1.0 \times 10^3$	44.294 ± 0.003	51^{+5}_{-4}	$49\ ^{+1.8 \times 10^2}_{-34}$

Notes.
[a] `headobjid` from SDSS tables.
[b] Redshift.
[c] Rest frame equivalent width of broad line.
[d] FWHM of broad line.
[e] Computed from Kaspi relation, in rest frame.
[f] Own computation from all points within the 68% CI, in rest frame.

The second estimate for the first subsample of 17 light curves, done with Hβ and Hγ in r band, gives no sensible result (see Figure 7(b)). Even when omitting light curves with a clearly unreliable posterior PDF, the PDF tends to a prior cutoff at $\tau_{\mathrm{delay}}/\tau_{\mathrm{delay,expected}} = 4$. This might be because Hβ is mostly weak, and there is a contribution from Hγ and O III λ4959, λ5007. Thus our assumption of having the most contribution from one broadened line (here: Hβ) doesn't hold. For two luminosity bins in Figure 8(d), the points would lie above the prior cutoff line, so we consider them to be unreliable. These points are only given for reasons of completeness.

6.2. Individual and Ensemble Estimates of Black Hole Masses

We converted the computed observer-frame time delays $\tau_{\mathrm{delay,obs}}$ into rest frame delays by applying a cosmological $(1+z)^{-1}$ factor. Then they are converted to reverberation-based M_{BH} by applying Equation (1). To define $M_{\mathrm{BH}} - L$ relations, we follow Vestergaard (2002), using $\lambda L_\lambda(5100\ \text{Å})$ and $L_{\mathrm{H}\beta}$ as luminosity measures.

Vestergaard et al. (Vestergaard 2002; Vestergaard & Peterson 2006) found four empirical mass scaling relationships between line widths and luminosity for estimating M_{BH} in nearby AGNs and distant luminous quasars up to $z \sim 6$. In detail, they found

Table 3
Sample 2 Properties and Reverberation Mapping Results $z = 0.555$–0.591, with g Band: Mg II, r Band: Continuum

Object[a]	z[b]	EW(Mg II)/Å[c]	$\frac{\mathrm{FWHM}(H\beta)}{1000\ \mathrm{km\ s^{-1}}}$ [d]	$\log\left[\frac{\lambda L_\lambda(5100\ \text{Å})}{\mathrm{erg\ s^{-1}}}\right]$	$\frac{R_{\mathrm{BLR,Kaspi}}}{\mathrm{lightdays}}$ [e]	$\frac{R_{\mathrm{BLR}}}{\mathrm{lightdays}}$ [f]
587731185127129152	0.5826	41 ± 8	$2.6 \times 10^3 \pm 2.9 \times 10^2$	44.17 ± 0.06	42^{+8}_{-7}	$53^{+1.4\times10^2}_{-41}$
587731185661640908	0.5755	4 ± 8	$1.8 \times 10^3 \pm 80$	44.33 ± 0.02	55^{+7}_{-6}	$41^{+1.8\times10^2}_{-27}$
587731185663082656	0.5651	22 ± 3	$3.2 \times 10^3 \pm 5.7 \times 10^2$	44.40 ± 0.02	61^{+8}_{-7}	$2.2 \times 10^2{}^{+34}_{-2.0\times10^2}$
587731185663475838	0.5649	17 ± 5	$3.0 \times 10^3 \pm 1.1 \times 10^3$	44.10 ± 0.08	37^{+9}_{-7}	$45^{+1.2\times10^2}_{-34}$
587731185663672525	0.5838	58 ± 20	$1.0 \times 10^3 \pm 4.5 \times 10^3$	44.22 ± 0.05	46^{+8}_{-7}	$39^{+1.7\times10^2}_{-26}$
587731185669898347	0.5681	31 ± 5	$6.1 \times 10^3 \pm 2.3 \times 10^3$	44.35 ± 0.03	56^{+8}_{-7}	$76^{+1.8\times10^2}_{-60}$
587731186198708457	0.5886	53 ± 10	$2.2 \times 10^3 \pm 3.2 \times 10^2$	44.22 ± 0.02	45^{+5}_{-5}	$39^{+1.7\times10^2}_{-23}$
587731186199036062	0.5551	13 ± 2	$1.9 \times 10^3 \pm 2.0 \times 10^3$	44.340 ± 0.009	55^{+6}_{-5}	$57^{+1.7\times10^2}_{-43}$
587731186205327526	0.5691	$1.0 \times 10^2 \pm 27$	$4.8 \times 10^3 \pm 2.0 \times 10^2$	44.29 ± 0.01	52^{+6}_{-5}	77^{+98}_{-63}
587731186208080015	0.5902	67 ± 13	$1.9 \times 10^3 \pm 2.6 \times 10^2$	44.18 ± 0.02	43^{+5}_{-4}	$16^{+1.8\times10^2}_{-4}$
587731186208211123	0.5766	28 ± 2	$5.8 \times 10^3 \pm 8.7 \times 10^2$	44.39 ± 0.02	60^{+8}_{-7}	$27^{+2.2\times10^2}_{-11}$
587731186455019583	0.5851	16 ± 2	$1.9 \times 10^3 \pm 97$	45.305 ± 0.004	$2.6 \times 10^2{}^{+47}_{-40}$	$9.8 \times 10^2{}^{+2.0\times10^2}_{-6.8\times10^2}$
587731186731254014	0.5662	$1.3 \times 10^2 \pm 11$	$6.6 \times 10^3 \pm 1.2 \times 10^3$	44.324 ± 0.009	54^{+6}_{-5}	$2.3 \times 10^2{}^{+12}_{-1.9\times10^2}$
587731186734006569	0.5717	31 ± 6	$5.5 \times 10^3 \pm 2.0 \times 10^3$	44.274 ± 0.02	50^{+6}_{-5}	$44^{+1.6\times10^2}_{-31}$
587731186734596354	0.5676	53 ± 7	$1.5 \times 10^3 \pm 2.1 \times 10^3$	44.29 ± 0.02	51^{+6}_{-5}	$74^{+1.6\times10^2}_{-60}$
587731186742788371	0.5756	$2.0 \times 10^2 \pm 29$	$7.1 \times 10^3 \pm 4.1 \times 10^3$	43.99 ± 0.03	32^{+4}_{-3}	$142^{+1.7}_{-99}$
587731187272908947	0.5792	42 ± 6	$4 \times 10^3 \pm 8.1 \times 10^2$	44.35 ± 0.02	56^{+7}_{-6}	$32^{+2.0\times10^2}_{-17}$
587731187282215130	0.5587	38 ± 5	$4.3 \times 10^3 \pm 4.8 \times 10^2$	44.32 ± 0.02	54^{+6}_{-6}	$30^{+2.1\times10^2}_{-15}$
587731187809386613	0.5705	$1.4 \times 10^2 \pm 23$	$6.5 \times 10^3 \pm 2.7 \times 10^3$	43.94 ± 0.02	29^{+3}_{-3}	112^{+7}_{-98}
587731187816136876	0.568	41 ± 7	$6.3 \times 10^3 \pm 1.9 \times 10^3$	44.31 ± 0.03	53^{+7}_{-6}	$215^{+2}_{-2.0\times10^2}$
587731511545823430	0.5734	74 ± 15	$8.9 \times 10^3 \pm 1.5 \times 10^3$	44.11 ± 0.08	38^{+8}_{-6}	$18^{+1.6\times10^2}_{-7}$
587731512073584798	0.5846	56 ± 5	$7.4 \times 10^3 \pm 1.8 \times 10^3$	44.43 ± 0.02	64^{+9}_{-9}	51^{+86}_{-33}
587731512612815013	0.5555	40 ± 7	$4.0 \times 10^3 \pm 7.5 \times 10^2$	44.25 ± 0.02	48^{+5}_{-5}	$41^{+1.8}_{-27}$
587731512613929053	0.5633	36 ± 5	$2.8 \times 10^3 \pm 5.3 \times 10^2$	44.20 ± 0.05	44^{+7}_{-6}	$26^{+1.7\times10^2}_{-13}$
587731512615829758	0.5696	34 ± 5	$7.6 \times 10^3 \pm 1.7 \times 10^3$	44.26 ± 0.02	48^{+6}_{-5}	$31^{+1.7\times10^2}_{-19}$
587731512620548263	0.5762	32 ± 6	$3.3 \times 10^3 \pm 1.4 \times 10^3$	44.05 ± 0.04	34^{+5}_{-4}	49^{+94}_{-40}
587731512621727958	0.5805	19 ± 4	$4.2 \times 10^3 \pm 1.9 \times 10^3$	44.25 ± 0.01	47^{+5}_{-5}	$51^{+1.6\times10^2}_{-38}$
587731513142935636	0.5697	37 ± 4	$3.3 \times 10^3 \pm 6.1 \times 10^2$	44.32 ± 0.02	53^{+7}_{-6}	$48^{+1.7\times10^2}_{-34}$
587731513144967281	0.574	42 ± 13	$2.1 \times 10^3 \pm 5.7 \times 10^2$	44.17 ± 0.02	42^{+5}_{-4}	20^{+154}_{-9}
587731513146736743	0.5895	19 ± 2	$3.7 \times 10^3 \pm 2.0 \times 10^2$	45.141 ± 0.004	$2.0 \times 10^2{}^{+33}_{-28}$	$8.9 \times 10^2{}^{+20}_{-6.4\times10^2}$
587731513146736818	0.5776	$1.5 \times 10^2 \pm 12$	$3.6 \times 10^3 \pm 1.4 \times 10^3$	44.39 ± 0.01	60^{+7}_{-6}	95^{+41}_{-36}
587731513150079130	0.5832	29 ± 4	$3.5 \times 10^3 \pm 6.4 \times 10^2$	44.28 ± 0.01	50^{+6}_{-5}	$53^{+1.5\times10^2}_{-40}$
587731513150210254	0.5667	21 ± 2	$5.5 \times 10^3 \pm 8.6 \times 10^2$	44.29 ± 0.04	51^{+8}_{-7}	$97^{+1.1\times10^2}_{-83}$
587731513151455344	0.5911	16 ± 5	$2.3 \times 10^3 \pm 5.3 \times 10^2$	44.51 ± 0.01	73^{+10}_{-8}	$37^{+2.6\times10^2}_{-18}$
587731513153683711	0.5909	55 ± 5	$6.1 \times 10^3 \pm 2.3 \times 10^3$	44.37 ± 0.01	58^{+7}_{-6}	$37^{+2.0\times10^2}_{-22}$
587731513154535595	0.5623	11 ± 6	$3.5 \times 10^3 \pm 1.3 \times 10^3$	44.11 ± 0.03	38^{+5}_{-4}	$40^{+1.7\times10^2}_{-30}$
587731513157746873	0.5766	29 ± 3	$6.1 \times 10^3 \pm 6.8 \times 10^2$	44.53 ± 0.01	76^{+10}_{-9}	$56^{+2.9\times10^2}_{-35}$
587731514220544089	0.5699	93 ± 8	$8.2 \times 10^3 \pm 3.1 \times 10^3$	44.26 ± 0.04	49^{+8}_{-6}	97^{+80}_{-83}
587731514231226522	0.5561	26 ± 4	$3.3 \times 10^3 \pm 4.3 \times 10^2$	44.43 ± 0.01	64^{+8}_{-7}	$72^{+2.2\times10^2}_{-54}$
587734304876593453	0.5773	58 ± 11	$3.8 \times 10^3 \pm 2.7 \times 10^3$	44.21 ± 0.03	46^{+6}_{-5}	$33^{+1.5\times10^2}_{-21}$
587734304880656528	0.5856	68 ± 29	$19.5 \times 10^3 \pm 5.9 \times 10^3$	44 ± 8 (?)	20	30^{+52}_{-24}
587734305416413383	0.5758	$1.2 \times 10^2 \pm 31$	$6.8 \times 10^3 \pm 4.3 \times 10^3$	44.33 ± 0.02	55^{+7}_{-6}	$46^{1.1\times10^2+}_{-31}$
588015507662635090	0.5675	57 ± 8	$4.5 \times 10^3 \pm 5.5 \times 10^2$	44.40 ± 0.01	61^{+7}_{-6}	$36^{+2.2\times10^2}_{-20}$
588015507681509558	0.5645	86 ± 33	$1.3 \times 10^3 \pm 6.0 \times 10^3$	43.9 ± 0.1	27^{+8}_{-6}	$21^{+1.0\times10^2}_{-13}$
588015507682033872	0.5891	30 ± 5	$4.3 \times 10^3 \pm 3.6 \times 10^2$	44.4 ± 0.01	67^{+8}_{-7}	$95^{+1.8\times10^2}_{-77}$
588015508190068915	0.5777	58 ± 6	$4.4 \times 10^3 \pm 2.1 \times 10^3$	44.29 ± 0.04	51^{+8}_{-7}	$55^{+1.6\times10^2}_{-41}$
588015508191903965	0.5647	27 ± 6	$2.8 \times 10^3 \pm 7.8 \times 10^2$	44.31 ± 0.02	53^{+6}_{-6}	$52^{+1.7\times10^2}_{-38}$
588015508196491368	0.5728	33 ± 5	$2.8 \times 10^3 \pm 5.2 \times 10^2$	44.29 ± 0.02	50^{+6}_{-5}	$4.4 \times 10^2{}^{+1.7\times10^2}_{-24}$

Table 3
(Continued)

Object[a]	z[b]	EW(Mg II)/Å[c]	$\frac{\mathrm{FWHM(H}\beta)}{1000\ \mathrm{km\ s^{-1}}}$ [d]	$\log\left[\frac{\lambda L_\lambda(5100\ \text{Å})}{\mathrm{erg\ s^{-1}}}\right]$	$\frac{R_{\mathrm{BLR,Kaspi}}}{\mathrm{lightdays}}$ [e]	$\frac{R_{\mathrm{BLR}}}{\mathrm{lightdays}}$ [f]
588015508197802108	0.5755	$1.1 \times 10^2 \pm 41$	$9.0 \times 10^3 \pm 7.5 \times 10^2$	44.31 ± 0.05	53^{+10}_{-8}	$1.7 \times 10^2\ ^{+67}_{-1.2 \times 10^2}$
588015508200489107	0.5576	44 ± 5	$3.2 \times 10^3 \pm 4.4 \times 10^2$	44.30 ± 0.02	52^{+6}_{-5}	$84^{+1.3 \times 10^2}_{-70}$
588015508207567019	0.5582	66 ± 4	$7.8 \times 10^3 \pm 6.3 \times 10^2$	44.40 ± 0.04	61^{+10}_{-9}	$29^{+1.3 \times 10^2}_{-13}$
588015508211630268	0.5736	48 ± 18	$8.4 \times 10^3 \pm 2.3 \times 10^3$	44.09 ± 0.07	37^{+8}_{-6}	$22^{+1.3 \times 10^2}_{-13}$
588015508736966847	0.5576	16 ± 3	$3.4 \times 10^3 \pm 6.1 \times 10^2$	44.41 ± 0.01	62^{+7}_{-7}	$50^{+2.3 \times 10^2}_{-32}$
588015508742865130	0.5749	45 ± 4	$5.2 \times 10^3 \pm 2.8 \times 10^3$	44.30 ± 0.03	52^{+7}_{-86}	$1.3 \times 10^2\ ^{+85}_{-67}$
588015508745486547	0.5646	82 ± 5	$3.9 \times 10^3 \pm 7.1 \times 10^2$	44.41 ± 0.03	62^{+9}_{-8}	$1.5 \times 10^2\ ^{+1.1 \times 10^2}_{-98}$
588015508747780246	0.5574	40 ± 4	$5.6 \times 10^3 \pm 5.7 \times 10^2$	44.11 ± 0.02	38^{+4}_{-4}	$39^{+1.2 \times 10^2}_{-29}$
588015508756234443	0.5748	33 ± 5	$6.9 \times 10^3 \pm 8.9 \times 10^2$	44.21 ± 0.03	45^{+6}_{-5}	$184^{+0.15}_{-1.7 \times 10^2}$
588015508756234590	0.5684	40 ± 8	$2.8 \times 10^3 \pm 4.3 \times 10^3$	44.33 ± 0.04	55^{+9}_{-8}	$45^{+2.0 \times 10^2}_{-29}$
588015509265449124	0.5854	23 ± 5	$6.1 \times 10^3 \pm 1.6 \times 10^3$	44.21 ± 0.02	45^{+6}_{-5}	$61^{+1.2 \times 10^2}_{-49}$
588015509267021941	0.5555	63 ± 13	$11.1 \times 10^3 \pm 2.4 \times 10^3$	44.23 ± 0.031	46^{+5}_{-7}	$42^{+1.5 \times 10^2}_{-30}$
588015509268660273	0.5599	33 ± 1	$4.3 \times 10^3 \pm 3.2 \times 10^2$	45.1424 ± 0.005	$2 \times 10^2\ ^{+34}_{-29}$	$2.2 \times 10^2\ ^{+5.9 \times 10^2}_{-1.7 \times 10^2}$
588015509269315709	0.57	24 ± 2	$6.9 \times 10^3 \pm 1.6 \times 10^3$	44.39 ± 0.06	60^{+12}_{-10}	$1.9 \times 10^2\ ^{+82}_{-1.7 \times 10^2}$
588015509282947197	0.559	45 ± 9	$5.8 \times 10^3 \pm 1.4 \times 10^3$	44.28 ± 0.02	50^{+6}_{-6}	$21^{+2.0 \times 10^2}_{-7}$
588015509287928008	0.5641	39 ± 4	$3.3 \times 10^3 \pm 6.9 \times 10^2$	44.31 ± 0.02	52^{+6}_{-5}	$68^{+1.7 \times 10^2}_{-53}$
588015509822832766	0.5582	58 ± 7	$2.9 \times 10^3 \pm 8.8 \times 10^2$	44.09 ± 0.02	37^{+4}_{-4}	$24^{+1.3 \times 10^2}_{-14}$
588015510343516323	0.5783	106 ± 8	$4.9 \times 10^3 \pm 6.3 \times 10^2$	44.29 ± 0.02	51^{+7}_{-6}	94^{+78}_{-57}
588015510360883275	0.5691	38 ± 1	$4.6 \times 10^3 \pm 8.7 \times 10^2$	45.653 ± 0.005	$4.6 \times 10^2\ ^{+99}_{-81}$	$1.2 \times 10^3\ ^{+5 \times 10^2}_{-65}$
588015510367764698	0.5775	87 ± 22	$4.5 \times 10^3 \pm 1.4 \times 10^3$	44.236 ± 0.07	47^{+10}_{-8}	87^{+61}_{-32}

Notes.
[a] `headobjid` from SDSS tables.
[b] Redshift.
[c] Rest frame equivalent width of broad line.
[d] FWHM of broad line.
[e] Computed from Kaspi relation, in rest frame.
[f] Own computation from all points within the 68% CI, in rest frame.

the following relationships for the optical regime:

$$\log M_{\mathrm{BH,Vestergaard1}} = \log\left(\left(\frac{\mathrm{FWHM(H}\beta)}{1000\ \mathrm{km\ s^{-1}}}\right)^2 \times \left(\frac{\lambda L_\lambda(5100\ \text{Å})}{10^{44}\ \mathrm{erg\ s^{-1}}}\right)^{0.50}\right) + (6.91 \pm 0.02) \quad (42)$$

$$\log M_{\mathrm{BH,Vestergaard2}} = \log\left(\left(\frac{\mathrm{FWHM(H}\beta)}{1000\ \mathrm{km\ s^{-1}}}\right)^2 \times \left(\frac{L_{\mathrm{H}\beta}}{10^{42}\ \mathrm{erg\ s^{-1}}}\right)^{0.63}\right) + (6.67 \pm 0.03). \quad (43)$$

Additional relationships exist for the UV, which cannot be applied here because no line widths are available from SDSS S82 data. They are given in Vestergaard & Peterson (2006).

For comparing to the masses from the Vestergaard relations, we calculate the reverberation-mapping based M_{BH} by using Equation (1). We set $f = 1$, and so we get

$$M_{\mathrm{BH,rev}} = 0.195 \left(\frac{\mathrm{FWHM(H}\beta)}{\mathrm{km\ s^{-1}}}\right)^2 \frac{\tau_{\mathrm{delay}}}{\mathrm{days}}\ M_\odot. \quad (44)$$

To determine the proportionality constant to the relationships, we adopt the form $M_{\mathrm{BH}} \propto M_{\mathrm{BH,Vestergaard1}}$ and $M_{\mathrm{BH}} \propto M_{\mathrm{BH,Vestergaard2}}$.

We calculated the posterior probability distributions from evaluating Equation (23) projected as a histogram, because we marginalize over the flux scaling factors e and s. This was done for different binning classes because we assume that $\tau_{\mathrm{delay}}/\tau_{\mathrm{delay,exp}} = f(L, z, \mathrm{EW_{line}})$.

For comparing to the relations (42) and (43), we binned by z according to our subsample Tables 2–5. We evaluated 29 light curves in the redshift range $z = 0.225$–0.291, with i band: Hα, z band: continuum. Seventeen light curves out of this range were also evaluated with r band: Hβ, Hγ (plus some other), g band: continuum. We evaluated 68 light curves in the redshift range $z = 0.555$–0.591 with g-band Mg II, r: continuum. We evaluated 111 light curves in the redshift range $z = 0.592$–0.6999, with g-band Mg II (Fe II λ2600), r continuum. The redshift range $z = 0.7$–0.846 was evaluated with g-band Mg II (Fe II λ2600), r continuum for 115 light curves.

In Figures 8(e)–(f) we show the deviations of our reverberation-based ensemble M_{BH} estimates from those of the Vestergaard relations as a function of z. Our result again shows ensemble estimates larger than those by the scaling relationships from Vestergaard by a factor of about 1.7, but with slightly larger deviations.

Table 4
Sample 3 Properties and Reverberation Mapping Results $z = 0.592$–0.6999, with g Band: Mg II, r Band: Continuum

Object[a]	z[b]	EW(Mg II)/Å[c]	$\frac{\mathrm{FWHM(H}\beta)}{1000\ \mathrm{km\ s^{-1}}}$ [d]	$\log\left[\frac{\lambda L_\lambda(5100\,\text{Å})}{\mathrm{erg\ s^{-1}}}\right]$	$\frac{R_{\mathrm{BLR,Kaspi}}}{\mathrm{lightdays}}$ [e]	$\frac{R_{\mathrm{BLR}}}{\mathrm{lightdays}}$ [f]
587730845814686076	0.6019	40 ± 6	$3.6 \times 10^3 \pm 6.1 \times 10^2$	44.18 ± 0.04	43^{+7}_{-6}	$54^{+1.4\times10^2}_{-41}$
587730846349919079	0.5988	85 ± 15	$4.6 \times 10^3 \pm 2.1 \times 10^3$	44.13 ± 0.04	40^{+6}_{-5}	91^{+88}_{-74}
587730847429689592	0.6615	35 ± 7	$1.2 \times 10^3 \pm 2.9 \times 10^3$	44.19 ± 0.06	43^{+9}_{-7}	$46^{+1.5\times10^2}_{-33}$
587730847430148472	0.6212	$3.8 \times 10^2 \pm 97$	42.44 ± 0.09	44.25 ± 0.01	48^{+5}_{-5}	$29^{+1.4\times10^2}_{-15}$
587730847960662320	0.6163	70 ± 8	$2.0 \times 10^3 \pm 2.2 \times 10^3$	44.34 ± 0.02	55^{+7}_{-6}	4^{+46}_{-29}
587731172231545105	0.6809	30 ± 1	$1.9 \times 10^3 \pm 1.1 \times 10^3$	45.21 ± 0.008	$2.3 \times 10^2\ ^{+41}_{-34}$	$4.5 \times 10^2\ ^{+5.7\times10^2}_{-3.9\times10^2}$
587731173842093154	0.6533	25 ± 5	$5.0 \times 10^3 \pm 1.7 \times 10^3$	44.55 ± 0.08	77^{+20}_{-15}	$17^{+3.3\times10^2}_{-5}$
587731174915507603	0.6074	31 ± 7	$7.6 \times 10^3 \pm 2.1 \times 10^3$	44.28 ± 0.02	50^{+6}_{-5}	$56^{+1.7\times10^2}_{-42}$
587731185656004677	0.8422	28 ± 3	$5.3 \times 10^3 \pm 2.7 \times 10^3$	44.9 ± 0.1	$1.5 \times 10^2\ ^{+63}_{-42}$	$2.3 \times 10^2\ ^{+4.4\times10^2}_{-1.9\times10^2}$
587731185660657782	0.6964	17 ± 3	$3.3 \times 10^3 \pm 5.3 \times 10^2$	$45{,}05 \pm 0.01$	$1.7 \times 10^2\ ^{+30}_{-25}$	$2.3 \times 10^2\ ^{+5.6\times10^2}_{-1.8\times10^2}$
587731185663410412	0.606	14 ± 3	$4.8 \times 10^3 \pm 3.2 \times 10^3$	44.35 ± 0.07	56^{+12}_{-10}	$72^{+1.8\times10^2}_{-56}$
587731185665507634	0.5981	93 ± 30	$3.6 \times 10^3 \pm 2.1 \times 10^3$	44.21 ± 0.02	45^{+5}_{-5}	$20^{+1.8\times10^2}_{-7}$
587731185673044112	0.619	41 ± 6	$3.1 \times 10^3 \pm 2.4 \times 10^3$	44.33 ± 0.02	55^{+7}_{-6}	$51^{+2.0\times10^2}_{-35}$
587731186197856351	0.6161	18 ± 3	$1.7 \times 10^3 \pm 6.5 \times 10^2$	45.027 ± 0.007	$1.7 \times 10^2\ ^{+27}_{-23}$	$98^{+6.6\times10^2}_{-51}$
587731186201002148	0.6958	26 ± 4	$2.7 \times 10^3 \pm 7.3 \times 10^2$	44.31 ± 0.05	52^{+9}_{-8}	$53^{+1.8\times10^2}_{-38}$
587731186206113952	0.6321	30 ± 5	$3.1 \times 10^3 \pm 5.0 \times 10^2$	44.35 ± 0.05	56^{+10}_{-8}	$55^{+2\times10^2}_{-39}$
587731186724373007	0.6546	41 ± 7	$4.4 \times 10^3 \pm 1.7 \times 10^3$	44.26 ± 0.03	49^{+6}_{-6}	$90^{+1.1\times10^2}_{-75}$
587731186740428908	0.6131	65 ± 6	$8.0 \times 10^3 \pm 1.2 \times 10^3$	44.32 ± 0.03	54^{+8}_{-7}	$2.4 \times 10^2\ ^{+0.6}_{-2.3\times10^2}$
587731186743443659	0.599	15 ± 6	$1.4 \times 10^3 \pm 1.7 \times 10^3$	44.33 ± 0.02	55^{+7}_{-6}	$33^{+2.1\times10^2}_{-17}$
587731186744492204	0.6321	44 ± 4	$3.9 \times 10^3 \pm 5.2 \times 10^2$	44.28 ± 0.03	51^{+7}_{-6}	$100^{+1.3\times10^2}_{-86}$
587731187263209489	0.6436	25 ± 3	$1.7 \times 10^3 \pm 6.5 \times 10^2$	45.089 ± 0.005	$1.9 \times 10^2\ ^{+30}_{-26}$	$4.7 \times 10^2\ ^{+3.7\times10^2}_{-3.7\times10^2}$
587731187280183499	0.6815	66 ± 15	$1.9 \times 10^3 \pm 6.1 \times 10^2$	44.20 ± 0.07	44^{+9}_{-7}	$30^{+9.8\times10^2}_{-18}$
587731187281166449	0.609	25 ± 6	$5.2 \times 10^3 \pm 1.8 \times 10^3$	44.36 ± 0.02	57^{+8}_{-7}	$80^{+1.8\times10^2}_{-63}$
587731187281494159	0.6572	46 ± 3	$4.8 \times 10^3 \pm 4.1 \times 10^2$	44.22 ± 0.04	45^{+7}_{-6}	$45^{+1.6\times10^2}_{-32}$
587731187814236291	0.6965	67 ± 6	$8.9 \times 10^3 \pm 2.5 \times 10^3$	44.34 ± 0.05	55^{+10}_{-8}	$44^{+1.8\times10^2}_{-28}$
587731187814432903	0.683	16 ± 4	$3.4 \times 10^3 \pm 5.8 \times 10^2$	44.32 ± 0.03	53^{+7}_{-6}	$45^{+2.0\times10^2}_{-29}$
587731511534092414	0.6576	61 ± 5	$7.1 \times 10^3 \pm 9.6 \times 10^2$	44.43 ± 0.05	64^{+13}_{-10}	$1.9 \times 10^2\ ^{+1.0\times10^2}_{-1.6\times10^2}$
587731511541039324	0.6841	64 ± 13	$1.6 \times 10^3 \pm 1.6 \times 10^3$	44.43 ± 0.06	64^{+14}_{-11}	$1.3 \times 10^2\ ^{+1.6\times10^2}_{-93}$
587731511543464064	0.66	23 ± 2	$2.9 \times 10^3 \pm 6.3 \times 10^2$	44.49 ± 0.04	76^{+12}_{-10}	$2.0 \times 10^2\ ^{+1.2\times10^2}_{-1.8\times10^2}$
587731512068276412	0.6301	27 ± 7	$3.8 \times 10^3 \pm 3.5 \times 10^3$	44.32 ± 0.05	53^{+10}_{-8}	$15^{+2.3\times10^2}_{-5}$
587731512070439082	0.6885	46 ± 9	$4.5 \times 10^3 \pm 6.2 \times 10^2$	44.28 ± 0.06	50^{+10}_{-8}	$66^{+1.5\times10^2}_{-52}$
587731512080990324	0.642	84 ± 7	$4.9 \times 10^3 \pm 9.1 \times 10^2$	44.45 ± 0.03	66^{+11}_{-9}	$1.2 \times 10^2\ ^{+1.7\times10^2}_{-84}$
587731512082890897	0.5928	43 ± 7	$2.6 \times 10^3 \pm 5.9 \times 10^2$	44.3 ± 0.1	48^{+14}_{-11}	$36^{+1.8\times10^2}_{-22}$
587731512083284109	0.6544	28 ± 3	$3.9 \times 10^3 \pm 3.8 \times 10^2$	44.46 ± 0.06	67^{+15}_{-12}	$3\text{–}0 \times 10^2\ ^{+8}_{-2.8\times10^2}$
587731512083873838	0.6065 37	± 1	$3.5 \times 10^3 \pm 2.9 \times 10^2$ 45.074	± 0.009	$1.8 \times 10^2\ ^{+31}_{-26}$	$52^{+5.0\times10^2}_{-1.3}$
587731512607899778	0.675	38 ± 4	$3.3 \times 10^3 \pm 1.3 \times 10^3$	44.3 ± 0.03	46^{+6}_{-5}	$26^{+1.8\times10^2}_{-13}$
587731512607965328	0.6712	62 ± 5	$5.5 \times 10^3 \pm 3.4 \times 10^3$	44.40 ± 0.03	61^{+10}_{-8}	$83^{+19\times10^2}_{-64}$
587731512617468016	0.6449	135 ± 7	$6.5 \times 10^3 \pm 4.6 \times 10^2$	44.42 ± 0.02	62^{+9}_{-7}	$1.3 \times 10^2\ ^{+31}_{-51}$
587731512619106413	0.6371	43 ± 6	$4.3 \times 10^3 \pm 6.7 \times 10^2$	44.2 ± 0.1	41^{+15}_{-10}	$69^{+1.2\times10^2}_{-58}$
587731512621662350	0.6197	38 ± 5	$4.2 \times 10^3 \pm 7.4 \times 10^2$	44.45 ± 0.01	66^{+8}_{-7}	$48^{+2.5\times10^2}_{-29}$
587731512621793356	0.6018	131 ± 13	$8.3 \times 10^3 \pm 2.2 \times 10^3$	44.34 ± 0.03	55^{+8}_{-7}	$65^{+1.8\times10^2}_{-50}$
587731513142935682	0.6122	62 ± 7	$5.0 \times 10^3 \pm 1.4 \times 10^3$	44.30 ± 0.02	52^{+7}_{-6}	$85^{+1.5\times10^2}_{-70}$
587731513146671274	0.6112	25 ± 5	$9.2 \times 10^3 \pm 3.0 \times 10^3$	44.36 ± 0.03	57^{+8}_{-7}	$44^{+2.1\times10^2}_{-29}$
587731513149423729	0.6874	29 ± 4	$5.1 \times 10^3 \pm 1.5 \times 10^3$	44.46 ± 0.02	68^{+9}_{-8}	$50^{+2.6\times10^2}_{-31}$
587731513150668937	0.6234	39 ± 4	$4.1 \times 10^3 \pm 9.7 \times 10^2$	44.45 ± 0.02	66^{+9}_{8-}	$100^{+2.0\times10^2}_{-79}$
587731513151062143	0.633	32 ± 6	$2.3 \times 10^3 \pm 4.8 \times 10^2$	44.32 ± 0.05	53^{+9}_{-8}	$3.4^{+2.4\times10^2}_{-19}$

Table 4
(Continued)

Object[a]	z[b]	EW(Mg II)/Å[c]	$\frac{\mathrm{FWHM}(H\beta)}{1000\ \mathrm{km\ s^{-1}}}$ [d]	$\log\left[\frac{\lambda L_\lambda(5100\,\text{Å})}{\mathrm{erg\ s^{-1}}}\right]$	$\frac{R_{\mathrm{BLR,Kaspi}}}{\mathrm{lightdays}}$ [e]	$\frac{R_{\mathrm{BLR}}}{\mathrm{lightdays}}$ [f]
587731513152241754	0.6325	$2.0 \times 10^2 \pm 13$	$5.0 \times 10^3 \pm 4.2 \times 10^2$	44.27 ± 0.05	49^{+8}_{-7}	33^{+45}_{-19}
587731513152438527	0.6967	36 ± 8	$1.6 \times 10^4 \pm 4.7 \times 10^3$	44.18 ± 0.03	43^{+6}_{-5}	$1.2 \times 10^2\,^{+77}_{-1.0 \times 10^2}$
587731513153683593	0.6271	61 ± 4	$1.9 \times 10^3 \pm 1.4 \times 10^3$	44.36 ± 0.02	57^{+8}_{-7}	$1.4 \times 10^2\,^{+1.0 \times 10^2}_{-1.2 \times 10^2}$
587731513154600973	0.6385	17.5 ± 0.6	$3.3 \times 10^3 \pm 75$	44.763 ± 0.002	$5.5 \times 10^2\,^{+1.2 \times 10^2}_{-99}$	$4.3 \times 10^2\,^{+1.2 \times 10^3}_{-2.8 \times 10^2}$
587731513158008994	0.6428	37 ± 2	$6.2 \times 10^3 \pm 7.8 \times 10^2$	44.47 ± 0.02	69^{+9}_{-8}	$1.0 \times 10^2\,^{+2.1 \times 10^2}_{-82}$
587731513159712875	0.6827	25 ± 1	$4.4 \times 10^3 \pm 3.2 \times 10^2$	44.4737 ± 0.007	$3.4 \times 10^2\,^{+70}_{-57}$	$2.3 \times 10^2\,^{+1.3 \times 10^3}_{-1.3 \times 10^2}$
587731513680855187	0.6529	62 ± 8	$6.1 \times 10^3 \pm 1.8 \times 10^3$	44.31 ± 0.02	52^{+6}_{-5}	$2.0 \times 10^2\,^{+38}_{-1.4 \times 10^2}$
587731513682952258	0.5941	46 ± 4	$5.1 \times 10^3 \pm 1.5 \times 10^3$	44.36 ± 0.02	57^{+8}_{-7}	$2.0 \times 10^2\,^{+63}_{-1.8 \times 10^2}$
587731513684983978	0.6064	40 ± 4	$5.6 \times 10^3 \pm 9.4 \times 10^2$	44.53 ± 0.08	75^{+20}_{-15}	$1.1 \times 10^2\,^{+2.3 \times 10^2}_{-83}$
587731513685115064	0.6885	30 ± 4	$1.6 \times 10^4 \pm 5.5 \times 10^3$	44.3 ± 0.1	56^{+22}_{-15}	$45^{+2.0 \times 10^2}_{-29}$
587731513685311641	0.6935	65 ± 11	$8.2 \times 10^3 \pm 3.2 \times 10^3$ 44.49	± 0.01	70^{+9}_{-8}	51^{73+}_{-31}
587731513686032593	0.5944	27 ± 4	$1.1 \times 10^4 \pm 1.7 \times 10^3$	44.48 ± 0.01	69^{+9}_{-8}	$50^{+2.6 \times 10^2}_{-31}$
587731513686884468	0.6153	26 ± 3	$1.9 \times 10^4 \pm 1.4 \times 10^3$	44.28 ± 0.02	50^{+6}_{-6}	$45^{+1-8 \times 10^2}_{-30}$
587731513691930901	0.6923	47 ± 9	$1.8 \times 10^3 \pm 2.9 \times 10^3$	44.39 ± 0.02	60^{+8}_{-7}	$39^{+2.3 \times 10^2}_{-22}$
587731513693438220	0.6186	58 ± 6	$1.9 \times 10^3 \pm 1.8 \times 10^3$	44.32 ± 0.03	63^{+7}_{-6}	89^{52}_{-58}
587731513695469663	0.633	33 ± 1	$4.9 \times 10^3 \pm 5.5 \times 10^2$	44.101 ± 0.002	$1.9 \times 10^2\,^{+30}_{-26}$	$71^{+6.6 \times 10^2}_{-18}$
587731514221789350	0.6005	59 ± 10	$3.4 \times 10^3 \pm 4.1 \times 10^3$	44.43 ± 0.02	64^{+9}_{-7}	$73^{+2.2 \times 10^2}_{-55}$
587731514224148656	0.6164	31 ± 4	$5.6 \times 10^3 \pm 1.8 \times 10^3$	44.23 ± 0.03	46^{+6}_{-5}	$52^{+2.6 \times 10^2}_{-38}$
587731514225393828	0.6003	35 ± 8	$3.8 \times 10^3 \pm 1.2 \times 10^3$	44.50 ± 0.02	71^{+10}_{-8}	$2.0 \times 10^2\,^{+1.2 \times 10^2}_{-1.8 \times 10^2}$
587731514228342988	0.6654	22 ± 3	$6.0 \times 10^3 \pm 9.4 \times 10^2$	44.3 ± 0.2	54^{+22}_{-15}	$49^{+1.9 \times 10^2}_{-35}$
587731514228408478	0.6102	38 ± 6	$8.3 \times 10^3 \pm 3.6 \times 10^3$	4.38 ± 0.05	59^{+11}_{-9}	$34^{+2.3 \times 10^2}_{-17}$
587734303270109310	0.6593	21 ± 11	$6.0 \times 10^3 \pm 7.6 \times 10^3$	44.22 ± 0.05	46^{+8}_{-7}	$62^{+1.4 \times 10^2}_{-49}$
587734303803179306	0.6951	37 ± 2	$3.9 \times 10^3 \pm 4.0 \times 10^2$	44.952 ± 0.006	148^{+23}_{-20}	$1.9 \times 10^2\,^{+4.8 \times 10^2}_{-1.5 \times 10^2}$
587734303806390551	0.6416	66 ± 7	$6.0 \times 10^3 \pm 1.3 \times 10^3$	44.13 ± 0.06	40^{+7}_{-6}	9.8^{+81}_{-46}
587734303807045647	0.6589	7 ± 1	$6.3 \times 10^3 \pm 3.0 \times 10^2$	44.998 ± 0.005	$1.6 \times 10^2\,^{+25}_{-22}$	$4.3 \times 10^2\,^{+2.9 \times 10^2}_{-3.8 \times 10^2}$
587734304339460348	0.6076	49 ± 10	$3.0 \times 10^3 \pm 3.8 \times 10^2$	44.33 ± 0.01	55^{+6}_{-5}	$50^{+2.0 \times 10^2}_{-35}$
587734304875085974	0.6712	33 ± 2	$11244.4 \pm 6.6 \times 10^2$	45.0 ± 0.03	$2\text{–}5 \times 10^2\,^{+60}_{-47}$	$1.1 \times 10^3\,^{+0.6}_{-8.1 \times 10^2}$
587734305414316071	0.6837	21 ± 2	$3.3 \times 10^3 \pm 1.1 \times 10^3$	44.94 ± 0.03	$1.5 \times 10^2\,^{+29}_{-23}$	$4.4 \times 10^2\,^{+2.2 \times 10^2}_{-4.0 \times 10^2}$
587734305680261334	0.6823	36 ± 1	$7.2 \times 10^3 \pm 1.6 \times 10^3$	45.13 ± 0.01	$2.0 \times 10^2\,^{+36}_{-30}$	$4.2 \times 10^2\,^{+4.6 \times 10^2}_{-1}$
588015507655819521	0.603	17 ± 4	$1.6 \times 10^3 \pm 2.3 \times 10^2$	44.34 ± 0.02	55^{+7}_{-6}	$59^{+1.9 \times 10^2}_{-43}$
588015507658440900	0.6012	54 ± 11	$3.1 \times 10^3 \pm 7.9 \times 10^2$	44.09 ± 0.04	37^{+5}_{-4}	$48^{+1.2 \times 10^2}_{-38}$
588015507662110749	0.6714	26.6 ± 0.8	$4.6 \times 10^3 \pm 3.3 \times 10^2$	45.301 ± 0.007	$2.6 \times 10^2\,^{+49}_{-41}$	$6.7 \times 10^2\,^{+5.1 \times 10^2}_{-6.0 \times 10^2}$
588015507671023717	0.6882	58 ± 5	$7.3 \times 10^3 \pm 7.0 \times 10^2$	44.2 ± 0.2	43^{+24}_{-14}	$119.888^{+73.0453}_{-77.8574}$
588015508191838443	0.6291	35 ± 9	$2.2 \times 10^3 \pm 1.3 \times 10^3$	44.32 ± 0.03	52^{+7}_{-6}	$68^{+1.7 \times 10^2}_{-53}$
588015508198326378	0.6754	38 ± 5	$7.7 \times 10^3 \pm 3.1 \times 10^3$	44.32 ± 0.05	54^{+10}_{-8}	$53^{+1.9 \times 10^2}_{-38}$
588015508199506219	0.6185	30 ± 4	$3.3 \times 10^3 \pm 9.6 \times 10^2$	44.22 ± 0.03	46^{+6}_{-5}	$60.4664^{+147.326}_{-47.408}$
588015508205404302	0.6228	102 ± 17	$4.9 \times 10^3 \pm 1.5 \times 10^3$	44.25 ± 0.02	48^{+6}_{-5}	$13.8029^{+149.6344}_{-0.1504}$
588015508210188443	0.6364	21 ± 6	$5.4 \times 10^3 \pm 1.1 \times 10^3$	44 ± 0.05	51^{+10}_{-8}	$58.7275^{+172.6071}_{-43.8074}$
588015508215496798	0.6136	39 ± 6	$3.4 \times 10^3 \pm 5.0 \times 10^3$	44.500 ± 0.007	72^{+8}_{-8}	$58^{+2.7 \times 10^2}_{-38}$
588015508215693543	0.6022	85 ± 9	43 ± 0.2	44.55 ± 0.01	78^{+10}_{-9}	$1.0 \times 10^2\,^{+43}_{-56}$
588015508219691244	0.6518	45 ± 4	$1.7 \times 10^3 \pm 1.1 \times 10^3$	44.49 ± 0.002	70^{+10}_{-8}	$2.2 \times 10^2\,^{+97}_{-2.0 \times 10^2}$
588015508736180263	0.6897	106 ± 4	$1.2 \times 10^3 \pm 2.0 \times 10^3$	45.00 ± 0.03	$1.6 \times 10^2\,^{+31}_{-25}$	$3.3 \times 10^2\,^{+4.0 \times 10^2}_{-2.8 \times 10^2}$
588015508736245912	0.6976	33 ± 4	$5.1 \times 10^3 \pm 3.2 \times 10^3$	44.3 ± 0.3	51^{+35}_{-19}	$92^{+1.4 \times 10^2}_{-77}$
588015508743192685	0.6202	37 ± 4	$4.9 \times 10^3 \pm 1.3 \times 10^3$	44.345 ± 0.03	56^{+8}_{-7}	$77^{+1.8 \times 10^2}_{-60}$
588015508746797215	0.5951	27 ± 4	$4.6 \times 10^3 \pm 5.3 \times 10^2$	44.34 ± 0.03	56^{+8}_{-7}	$77^{+1.8 \times 10^2}_{-60}$
588015509274886234	0.6462	70 ± 8	$7.3 \times 10^3 \pm 1.3 \times 10^3$	44.32 ± 0.06	54^{+11}_{-9}	$1.9 \times 10^2\,^{+51}_{-1.7 \times 10^2}$

Table 4
(Continued)

Object[a]	z[b]	EW(Mg II)/Å[c]	$\frac{\mathrm{FWHM(H}\beta)}{1000\ \mathrm{km\ s^{-1}}}$ [d]	$\log\left[\frac{\lambda L_\lambda(5100\ \text{Å})}{\mathrm{erg\ s^{-1}}}\right]$	$\frac{R_{\mathrm{BLR,Kaspi}}}{\mathrm{lightdays}}$ [e]	$\frac{R_{\mathrm{BLR}}}{\mathrm{lightdays}}$ [f]
588015509278884004	0.623	52 ± 5	$4.0 \times 10^3 \pm 6.4 \times 10^2$	44.33 ± 0.02	55^{+7}_{-6}	$1.3 \times 10^2\ ^{+1.2 \times 10^2}_{-1.1 \times 10^2}$
588015509286158482	0.6057	22 ± 4	$3.6 \times 10^3 \pm 1.7 \times 10^2$	44.40 ± 0.01	61^{+7}_{-7}	$75^{+2.0 \times 10^2}_{-57}$
588015509287141539	0.6501	29 ± 6	$2.8 \times 10^3 \pm 9.3 \times 10^2$	44.27 ± 0.02	49^{+7}_{-6}	$23^{+2.0 \times 10^2}_{-9}$
588015509289238698	0.6065	35 ± 6	$3.8 \times 10^3 \pm 1.5 \times 10^3$	44.26 ± 0.05	48^{+9}_{-8}	$7^{+1.8 \times 10^2}_{-23}$
588015509291663524	0.6058	58 ± 6	$5.4 \times 10^3 \pm 8.1 \times 10^2$	44.19 ± 0.02	44^{+5}_{-4}	$36^{+1.6 \times 10^2}_{-24}$
588015509292056718	0.5919	$1.4 \times 10^2 \pm 22$	$7.7 \times 10^3 \pm 1.8 \times 10^3$	44.42 ± 0.01	63^{+7}_{-6}	$1.0 \times 10^2\ ^{+35}_{-41}$
588015509293957240	0.6138	14 ± 3	$2.8 \times 10^3 \pm 3.9 \times 10^2$	44.28 ± 0.01	50^{+6}_{-5}	$35^{+1.9 \times 10^2}_{-21}$
588015509805989986	0.6912	28 ± 4	$2.2 \times 10^3 \pm 1.1 \times 10^3$	44.27 ± 0.05	50^{+9}_{-7}	$211.7124^{+12.7619}_{-196.2287}$
588015509815689306	0.6095	66 ± 6	$4.8 \times 10^3 \pm 2.1 \times 10^3$	44.23 ± 0.02	46^{+6}_{-5}	$88^{+1.2 \times 10^2}_{-75}$
588015509821915357	0.5961	136 ± 19	$1.2 \times 10^4 \pm 3.6 \times 10^3$	44.27 ± 0.03	49^{+7}_{-6}	$55^{+1.7 \times 10^2}_{-41}$
588015509824143507	0.6262	101 ± 15	$1.2 \times 10^4 \pm 3.2 \times 10^3$	44.29 ± 0.03	51^{+7}_{-6}	$33^{+2.0 \times 10^2}_{-17}$
588015509825716274	0.663	59 ± 5	$4.3 \times 10^2 \pm 9.8 \times 10^2$	44.47 ± 0.04	69^{+13}_{-11}	$83^{+2.3 \times 10^2}_{-64}$
588015510340042880	0.6359	49 ± 7	$2.1 \times 10^3 \pm 7.9 \times 10^2$	44.31 ± 0.03	52^{+7}_{-6}	$47^{+1.9 \times 10^2}_{-33}$
588015510350266371	0.6505	24 ± 2	$6.1 \times 10^3 \pm 3.4 \times 10^2$	45.04 ± 0.04	$1.7 \times 10^2\ ^{+40}_{-32}$	$421.0391^{+3.5 \times 10^2}_{-3.6 \times 10^2}$
588015510359244938	0.6796	27 ± 3	$2.8 \times 10^3 \pm 2.1 \times 10^3$	44.21 ± 0.09	45^{+11}_{-9}	$68^{+1.30 \times 10^2}_{-55}$
588015510361669834	0.6585	28 ± 4	$2.4 \times 10^3 \pm 1.8 \times 10^3$	44.36 ± 0.01	57^{+7}_{-6}	$21.009^{+236.4755}_{-4.894}$
588015510362325105	0.6378	29 ± 3	$2.6 \times 10^3 \pm 1.0 \times 10^3$	44.53 ± 0.02	75^{+11}_{-9}	$82^{+2.6 \times 10^2}_{-60}$
588015510362914849	0.6619	23 ± 1	$3.2 \times 10^3 \pm 5.8 \times 10^2$	44.984 ± 0.012	$1.6 \times 10^2\ ^{+26}_{-22}$	$4.4 \times 10^2\ ^{+2.7 \times 10^2}_{-3.9 \times 10^2}$
588015510366912891	0.6242	$1.2 \times 10^2 \pm 12$	$1.8 \times 10^4 \pm 1.5 \times 10^3$	43.91 ± 0.08	28^{+6}_{-5}	72^{+53}_{-43}

Notes.
[a] `headobjid` from SDSS tables.
[b] Redshift.
[c] Rest frame equivalent width of broad line.
[d] FWHM of broad line.
[e] Computed from Kaspi relation, in rest frame.
[f] Own computation from all points within the 68% CI, in rest frame.

6.3. Accuracy of the $R_{\mathrm{BLR}} - L$ and $M_{\mathrm{BH}} - L$ Estimates

As illustrated in Figure 5, time delays can only be robustly recovered if they fall into certain windows that are set by the S82 sampling. We now check the time delays inferred for the S82 from our analysis *post facto* against this criterion.

For this purpose we made a mean histogram of the inferred ensemble time lags for all the 323 light curves used to calculate the ensemble relation (Figure 8). For each of these objects, we used their UV luminosity and line width in conjunction with the Kaspi relation—scaled by the factor from Figure 8(a) for objects in any given bin—to predict their most likely τ_{delay}. This procedure results in a histogram of the inferred time delay $\tau_{\mathrm{delay,predicted}} \times factor$ for the objects in each bin, which are shown as colored histograms in the panels of Figure 9. Specifically, the scaling factors we used were the most likely ones for each bin, for example, 3.2 for Figure 9(a), 1.6 for Figure 9(b), 1.7 for Figure 9(c), 1.6 for Figure 9(d), 1.7 for Figure 9(e).

Assuming that the Kaspi relation with a factor of one is true, the τ_{delay} should fall into a region where we can recover them, as this was one of the selection criteria. If the inferred scaling factors from our analysis were true, the implied delays fall into the tails of the distribution. In this case, correct inference may occur, but its recovery robustness is not particularly likely. From further analysis, most of the individual τ_{delay} fall in regions were less than 50 percent of the time delays are assumed to be correctly calculated.

Additionally, reverberation-based masses are typically uncertain by a factor of $f = 2$–3. The absolute accuracy of the single-epoch mass estimates by Vestergaard (2002) is stated to be between a factor of 3.6 and 4.6. In addition, one has to keep in mind that the scaling relations and their uncertainties are of statistical nature. Any given single estimate from a $R_{\mathrm{BLR}} - L$ or $M_{\mathrm{BH}} - L$ scaling relation can be off by some factor. Therefore it should not be trusted in cases where high accuracy is needed. Such relations are, however, useful tools for application to large statistical samples.

7. CONCLUSION AND DISCUSSION

For the purpose of evaluating sparsely sampled photometric data, we implemented an advanced stochastical reverberation mapping algorithm in order to find correlated variations in a purely continuum and a continuum plus emission line band. This method is based on an approach for spectroscopic reverberation mapping by Rybicki & Kleyna (1994) and Zu et al. (2011), and extended for being capable of handling sparsely sampled multi-epoch photometric data in combination with constraining single-epoch spectroscopy. This enables us to use the data from available long-term photometric surveys, where we explored

Table 5
Sample 4 Properties and Reverberation Mapping Results $z = 0.7$–0.846, with g Band: Mg II, r Band: Continuum

Object[a]	z[b]	EW(Mg II)/Å [c]	$\frac{\mathrm{FWHM(H}\beta)}{1000\ \mathrm{km\ s^{-1}}}$ [d]	$\log\left[\frac{\lambda L_\lambda(5100\,\text{Å})}{\mathrm{erg\ s^{-1}}}\right]$	$\frac{R_{\mathrm{BLR,Kaspi}}}{\mathrm{lightdays}}$ [e]	$\frac{R_{\mathrm{BLR}}}{\mathrm{lightdays}}$ [f]
587730845818355869	0.7934	41 ± 2	$8.1 \times 10^3 \pm 6.0 \times 10^2$	45.12 ± 0.02	$1.9 \times 10^{2\ +38}_{\ -32}$	57^{+49}_{-2}
587730846355554516	0.8009	93 ± 16	$1.2 \times 10^3 \pm 1.5 \times 10^3$	44.1 ± 0.2	39^{+22}_{-13}	88^{+77}_{-76}
587730847426674879	0.7877	31 ± 3	$9.1 \times 10^3 \pm 9.6 \times 10^2$	44.96 ± 0.02	$1.5 \times 10^{2\ +28}_{\ -24}$	$92^{+6.0 \times 10^2}_{-49}$
587730847429689518	0.8232	24 ± 2	$3.8 \times 10^3 \pm 7.3v$	45.06 ± 0.03	$1.7 \times 10^{2\ +38}_{\ -30}$	$7.7 \times 10^{2\ +27}_{\ -7.2 \times 10^2}$
587731512612094070	0.8134	25 ± 3	$2.3 \times 10^3 \pm 3.7 \times 10^2$	44.98 ± 0.05	$1.5 \times 10^{2\ +38}_{\ -30}$	$4.2 \times 10^{2\ +2.8 \times 10^2}_{\ -3.7 \times 10^2}$
587730847966953841	0.7996	44 ± 5	$6.6 \times 10^3 \pm 3.7 \times 10^3$	44.1 ± 0.1	40^{+11}_{-8}	$37^{+1.5 \times 10^2}_{-25}$
587731185113759904	0.704	53 ± 5	$1.8 \times 10^4 \pm 1.6 \times 10^3$	45.31 ± 0.02	$2.7 \times 10^{2\ +57}_{\ -46}$	$1.2 \times 10^{3\ +0.6}_{\ -1.1 \times 10^3}$
588015509825912950	0.8199	24 ± 1	$3.8 \times 10^3 \pm 4.6 \times 10^2$	45.09 ± 0.05	$1.9 \times 10^{2\ +49}_{\ -38}$	$2.2 \times 10^{2\ +6.2 \times 10^2}_{\ -1.7 \times 10^2}$
587731185115070898	0.8356	43 ± 3	$8.7 \times 10^3 \pm 2.7 \times 10^3$	44.2 ± 0.1	43^{+15}_{-11}	$15^{+1.7 \times 10^2}_{-3}$
587731185117233542	0.8321	48 ± 4	$3.6 \times 10^3 \pm 2.5 \times 10^3$	45.18 ± 0.03	$2.13 \times 10^{2\ +48}_{\ -38}$	$2.3 \times 10^{2\ +4.0 \times 10^2}_{\ -1.7 \times 10^2}$
587731185126146205	0.8081	41 ± 5	$7.3 \times 10^3 \pm 4.2 \times 10^3$	44.3 ± 0.1	50^{+16}_{-11}	$46^{+1.8 \times 10^2}_{-34}$
587731185135321096	0.8404	38 ± 2	$6.0 \times 10^3 \pm 2.6 \times 10^3$	45.00 ± 0.08	$1.6 \times 10^{2\ +48}_{\ -36}$	$1.9 \times 10^{2\ +5.4 \times 10^2}_{\ -1.2 \times 10^3}$
587731185135910996	0.7563	44 ± 2	$2.9 \times 10^3 \pm 7.2 \times 10^2$	44.977 ± 0.008	$1.5 \times 10^{2\ +25}_{\ -21}$	$698.7417^{+0.7402}_{-648.7547}$
587731185653711180	0.705	29 ± 5	$5.7 \times 10^3 \pm 1.6 \times 10^2$	44 ± 0.1	52^{+18}_{-12}	$50^{+1.8 \times 10^2}_{-35}$
587731185662296109	0.755	37 ± 1	$4.4 \times 10^3 \pm 2.3 \times 10^2$	45.31 ± 0.03	$2.7 \times 10^{2\ +61}_{\ -49}$	$3.8 \times 10^{2\ +8.2 \times 10^2}_{\ -3.0 \times 10^2}$
587731185666293846	0.7643	44 ± 2	$3.8 \times 10^3 \pm 3.0 \times 10^2$	45.300 ± 0.007	$2.6 \times 10^{2\ +49}_{\ -41}$	$7.9 \times 10^{2\ +3.9 \times 10^2}_{\ -7.0 \times 10^2}$
587731186187632758	0.7449	44 ± 3	$8.7 \times 10^3 \pm 1.8 \times 10^3$	45.068 ± 0.006	$1.8 \times 10^{2\ +29}_{\ -25}$	$3.2 \times 10^{2\ +41}_{\ -1.9 \times 10^2}$
587731186189664401	0.8069	27 ± 2	$4.7 \times 10^3 \pm 6.3 \times 10^2$	45.24 ± 0.05	$2.4 \times 10^{2\ +66}_{\ -50}$	$4.2 \times 10^{2\ +6.5 \times 10^2}_{\ -3.5 \times 10^2}$
587731186190975111	0.7309	35 ± 2	$5.8 \times 10^3 \pm 7.2 \times 10^2$	45.13 ± 0.02	$1.9 \times 10^{2\ +37}_{\ -31}$	$6.3 \times 10^{2\ +2.6 \times 10^2}_{\ -5.5 \times 10^2}$
587731186192285977	0.7585	47 ± 6	$9.8 \times 10^3 \pm 9.6 \times 10^2$	43.94 ± 0.09	29^{+6}_{-5}	$30^{+1.0 \times 10^2}_{-21}$
587731186195693586	0.7732	24 ± 2	$2.3 \times 10^3 \pm 5.1 \times 10^2$	45.20 ± 0.01	$2.2 \times 10^{2\ +40}_{\ -34}$	$8.0 \times 10^{2\ +1.9 \times 10^2}_{\ -7.4 \times 10^2}$
587731186201329747	0.743	33 ± 2	$4.5 \times 10^3 \pm 4.7 \times 10^2$	45.00 ± 0.06	$1.6 \times 10^{2\ +42}_{\ -32}$	$6.5 \times 10^{2\ +81}_{\ -5.0 \times 10^2}$
587731186204803148	0.7334	31 ± 2	$3.0 \times 10^3 \pm 7.6 \times 10^2$	45.0 ± 0.1	$1.7 \times 10^{2\ +61}_{\ -43}$	$71.215^{+71.591}_{-23.309}$
587731186736103673	0.8103	41 ± 6	...	44.89 ± 0.03	134^{+27}_{-22}	$4.2 \times 10^{2\ +1.9 \times 10^2}_{\ -3.8 \times 10^2}$
587731186741936203	0.7477	22 ± 2	$4.9 \times 10^3 \pm 6.6 \times 10^2$	44.92 ± 0.07	142^{+41}_{-31}	$6.1 \times 10^{2\ +27}_{\ -5.6 \times 10^2}$
587731187283263580	0.7264	19.8 ± 0.6	$2.5 \times 10^3 \pm 7.2 \times 10^2$	45.200 ± 0.009	$2.2 \times 10^{2\ +40}_{\ -34}$	$4.1 \times 10^{2\ +5.9 \times 10^2}_{\ -3.4 \times 10^2}$
587731187801391447	0.8222	93 ± 12	$1.4 \times 10^4 \pm 1.1 \times 10^4$	44 ± 8 (?)	42	48^{+75}_{-36}
587731187803422729	0.7409	28 ± 2	$1.9 \times 10^3 \pm 3.6 \times 10^2$	45.18 ± 0.04	$2.1 \times 10^{2\ +53}_{\ -42}$	$5.4 \times 10^{2\ +4.3 \times 10^2}_{\ -4.7 \times 10^2}$
587731187805061144	0.8076	28 ± 2	$3.3 \times 10^3 \pm 8.5 \times 10^2$	44.93 ± 0.08	$1.4 \times 10^{2\ +43}_{\ -32}$	$1.2 \times 10^{2\ +5.3 \times 10^2}_{\ -77}$
587731187817054255	0.7286	31 ± 2	$5.4 \times 10^3 \pm 1.1 \times 10^3$	5.290 ± 0.008	$2.6 \times 10^{2\ +48}_{\ -40}$	$4.2 \times 10^{2\ +1.1 \times 10^2}_{\ -3.4 \times 10^2}$
587731187817185350	0.8237	168 ± 9	$1.2 \times 10^3 \pm 7.3 \times 10^2$	44.949 ± 0.008	$1.5 \times 10^{2\ +23}_{\ -20}$	$1.0 \times 10^{2\ +4.2 \times 10^2}_{\ -59}$
587731511533568075	0.7067	25 ± 2	$3.0 \times 10^3 \pm 7.5 \times 10^2$	45.13 ± 0.02	$2–0 \times 10^{2\ +39}_{\ -32}$	$2.3 \times 10^{2\ +6.7 \times 10^2}_{\ -1.7 \times 10^2}$
587731511533568176	0.7114	31 ± 6	$7.7 \times 10^3 \pm 8.5 \times 10^2$	45.030 ± 0.009	$1.7 \times 10^{2\ +28}_{\ -24}$	$20 \times 10^{2\ +5.6 \times 10^2}_{\ -1.5 \times 10^2}$
587731511537041576	0.7047	26 ± 3	$5.6 \times 10^3 \pm 2.1 \times 10^3$	44.42 ± 0.07	63^{+14}_{-11}	$60^{+2.2 \times 10^2}_{-43}$
587731511540187278	0.727	67 ± 8	$5.2 \times 10^3 \pm 1.1 \times 10^3$	44.23 ± 0.08	47^{+11}_{-8}	$84^{+1.3 \times 10^2}_{-70}$
587731511540514930	0.7746	30 ± 4	$5.2 \times 10^3 \pm 8.0 \times 10^2$	44.5 ± 0.2	66^{+36}_{-22}	$32^{+2.7 \times 10^2}_{-13}$
587731511545692429	0.8288	27 ± 6	$8.7 \times 10^3 \pm 3.2 \times 10^3$	43.9 ± 0.4	26^{+25}_{-12}	24^{+93}_{-17}
587731511547002980	0.7609	43 ± 4	$3.9 \times 10^3 \pm 1.5 \times 10^3$	44.98 ± 0.01	$1.6 \times 10^{2\ +26}_{\ -22}$	$4.0 \times 10^{2\ +3.0 \times 10^2}_{\ -3.5 \times 10^2}$
587731512073257137	0.7273	27 ± 3	$2.0 \times 10^3 \pm 1.3 \times 10^3$	44.44 ± 0.09	65^{+17}_{-13}	$76^{+2.2 \times 10^2}_{-58}$
587731512077516962	0.8402	39 ± 4	$5.1 \times 10^3 \pm 1.5 \times 10^3$	44.3 ± 0.3	48^{+21}_{-14}	$2.9 \times 10^{2\ +14}_{\ -1.9 \times 10^2}$
587731512077975687	0.7444	40 ± 5	$2.0 \times 10^3 \pm 9.2 \times 10^2$	44.39 ± 0.05	60^{+12}_{-9}	$66^{+2.0 \times 10^2}_{-49}$
587731512335663273	0.7359	78 ± 7	$4.2 \times 10^3 \pm 1.1 \times 10^3$	43.2 ± 0.2	9^{+4}_{-2}	37^{+1}_{-34}
587731512604688586	0.7379	96 ± 12	$9.0 \times 10^3 \pm 2.6 \times 10^3$	43.90 ± 0.05	28^{+4}_{-4}	$12^{+1.1 \times 10^2}_{-4}$
587731512613404738	0.766	35 ± 4	$5.4 \times 10^3 \pm 1.3 \times 10^3$	43.8 ± 0.2	24^{+9}_{-6}	38^{+69}_{-31}
587731512615371027	0.7327	40.7 ± 0.7	$1.3 \times 10^3 \pm 1.0 \times 10^3$	44.47 ± 0.05	68^{+14}_{-11}	$63^{+2.5 \times 10^2}_{-43}$
587731512617599004	0.7025	33 ± 1	$5.5 \times 10^3 \pm 6.3 \times 10^2$	45.12 ± 0.01	$1.9 \times 10^{2\ +35}_{\ -30}$	$1.0 \times 10^{2\ +33}_{\ -47}$

Table 5
(Continued)

Object[a]	z[b]	EW(Mg II)/Å [c]	$\frac{\mathrm{FWHM(H}\beta)}{1000\ \mathrm{km\ s^{-1}}}$ d	$\log\left[\frac{\lambda L_\lambda(5100\,\text{Å})}{\mathrm{erg\ s^{-1}}}\right]$	$\frac{R_{\mathrm{BLR,Kaspi}}}{\mathrm{lightdays}}$ e	$\frac{R_{\mathrm{BLR}}}{\mathrm{lightdays}}$ f
587731512617861317	0.8388	20 ± 1	$5.7 \times 10^3 \pm 3.9 \times 10^3$	45.03 ± 0.09	$1.7 \times 10^2\ ^{+56}_{-40}$	$1.9 \times 10^2\ ^{+5.6 \times 10^2}_{-1.4 \times 10^2}$
587731512618319897	0.7687	28 ± 1	$3.3 \times 10^3 \pm 3.4 \times 10^2$	45.616 ± 0.006	$4.4 \times 10^2\ ^{+92}_{-76}$	$1.8 \times 10^2\ ^{+59}_{-55}$
587731512618778741	0.7668	88 ± 7	$2.2 \times 10^3 \pm 2.9 \times 10^3$	44.36 ± 0.06	58^{+12}_{-9}	$2.6 \times 10^2\ ^{+0.1}_{-2.4 \times 10^2}$
587731513141035048	0.7534	54 ± 1	$6.3 \times 10^3 \pm 3.7 \times 10^2$	45.25 ± 0.01	$2.4 \times 10^2\ ^{+46}_{-38}$	$9.0 \times 10^2\ ^{+1.8 \times 10^2}_{-5.8 \times 10^2}$
587731513142214691	0.8054	16 ± 2	$2.5 \times 10^3 \pm 8.4 \times 10^2$	45.20 ± 0.09	$2.2 \times 10^2\ ^{+78}_{-55}$	$8.1 \times 10^2\ ^{+2.0 \times 10^2}_{-7.4 \times 10^2}$
587731513144508433	0.7783	22 ± 1	$3.4 \times 10^3 \pm 1.1 \times 10^3$	45.02 ± 0.02	$1.6 \times 10^2\ ^{+29}_{-24}$	$4.2 \times 10^2\ ^{+3.3 \times 10^2}_{-3.7 \times 10^2}$
587731513150144633	0.7741	58 ± 4	$4.0 \times 10^3 \pm 1.8 \times 10^3$	44.96 ± 0.08	$1.5 \times 10^2\ ^{+46}_{-34}$	$2.1 \times 10^2\ ^{+4.7 \times 10^2}_{-1.6 \times 10^2}$
587731513152045207	0.79	47 ± 5	$3.1 \times 10^3 \pm 1.4 \times 10^3$	44.4 ± 0.1	61^{+18}_{-13}	$1.0 \times 10^2\ ^{+1.7 \times 10^2}_{-86}$
587731513155387599	0.8394	39 ± 6	...	45.04 ± 0.04	$1.7 \times 10^2\ ^{+38}_{-31}$	$2.0 \times 10^2\ ^{+5.7 \times 10^2}_{-1.5 \times 10^2}$
587731513158991981	0.7823	25 ± 3	$2.3 \times 10^3 \pm 3.8 \times 10^3$	44.45 ± 0.07	66^{+16}_{-12}	$53^{+2.5 \times 10^2}_{-34}$
587731513409404993	0.777	29 ± 1	$4.4 \times 10^3 \pm 3.8 \times 10^2$	45.57 ± 0.01	$4.9 \times 10^2\ ^{+88}_{-72}$	$8.3 \times 10^2\ ^{+4.3 \times 10^2}_{-7.2 \times 10^2}$
587731513681051679	0.7415	74 ± 8	$1.6 \times 10^4 \pm 1.6 \times 10^4$	44.3 ± 0.1	49^{+19}_{-13}	$98^{+1.0 \times 10^2}_{-84}$
587731513685115005	0.8033	110 ± 13	$2.3 \times 10^4 \pm 1.1 \times 10^4$	43.8 ± 0.2	25^{+9}_{-6}	$7^{+1.0 \times 10^2}_{-0.01}$
587731513692192954	0.8303	39 ± 3	...	44.91 ± 0.04	$1.4 \times 10^2\ ^{+31}_{-25}$	$57^{+5.7 \times 10^2}_{-18}$
587731514215956525	0.8074	28 ± 2	$5.6 \times 10^3 \pm 1.4 \times 10^3$	44.94 ± 0.05	$1.5 \times 10^2\ ^{+36}_{-28}$	$4.1 \times 10^2\ ^{+2.5 \times 10^2}_{-3.7 \times 10^2}$
587731514221330585	0.7305	$1.3 \times 10^2 \pm 16$	$3.4 \times 10^3 \pm 5.1 \times 10^3$	44.15 ± 0.08	40^{+9}_{-7}	$40^{+1.4 \times 10^2}_{-26}$
587731514226639046	0.8088	48 ± 5	$3.8 \times 10^3 \pm 1.9 \times 10^3$	44.31 ± 0.08	53^{+13}_{-10}	$33^{+1.2 \times 10^2}_{-18}$
587734303807832105	0.8082	18 ± 2	$3.1 \times 10^3 \pm 1.3 \times 10^3$	45.76 ± 0.08	$5.5 \times 10^2\ ^{+2.2 \times 10^2}_{-1.5 \times 10^2}$	$1.2 \times 10^2\ ^{+4.1 \times 10^2}_{-1.1 \times 10^3}$
587734304877183038	0.7753	24 ± 2	$4.3 \times 10^3 \pm 1.2 \times 10^3$	44.95 ± 0.02	$1.5 \times 10^2\ ^{+28}_{-23}$	$3.7 \times 10^2\ ^{+3.0 \times 10^2}_{-3.3 \times 10^2}$
587734305415299187	0.8264	21 ± 1	$2.5 \times 10^3 \pm 4.1 \times 10^2$	45.18 ± 0.04	$2.1 \times 10^2\ ^{+53}_{-42}$	$1.9 \times 10^2\ ^{+7.6 \times 10^2}_{-1.3 \times 10^2}$
587734305950531598	0.7226	70 ± 4	$7.0 \times 10^3 \pm 5.2 \times 10^2$	45.263 ± 0.003	$2.5 \times 10^2\ ^{+43}_{-37}$	$8.7 \times 10^2\ ^{+2.4 \times 10^2}_{-1.2 \times 10^2}$
587734305952497968	0.7699	54 ± 6	$3.2 \times 10^3 \pm 3.8 \times 10^2$	44.90 ± 0.01	$1.4 \times 10^2\ ^{+22}_{-19}$	$2.0 \times 10^2\ ^{+4.1 \times 10^2}_{-1.7 \times 10^2}$
587734305954922626	0.7437	29 ± 2	$5.3 \times 10^3 \pm 1.2 \times 10^3$	44.94 ± 0.04	$1.5 \times 10^2\ ^{+32}_{-25}$	$4.1 \times 10^2\ ^{+2.5 \times 10^2}_{-3.6 \times 10^2}$
588015507653066986	0.7861	47 ± 6	$2.0 \times 10^3 \pm 1.9 \times 10^3$	44.2 ± 0.1	47^{+15}_{-11}	$34^{+1.8 \times 10^2}_{-20}$
588015507657654301	0.7675	34 ± 1	$2.9 \times 10^3 \pm 1.1 \times 10^3$	45.46 ± 0.03	$3.4 \times 10^2\ ^{+81}_{-64}$	$1.5 \times 10^3\ ^{+8}_{-1.3 \times 10^3}$
588015507660669093	0.805	30 ± 1	$2.9 \times 10^3 \pm 3.7 \times 10^2$	45.00 ± 0.03	$1.6 \times 10^2\ ^{+34}_{-27}$	$6.1 \times 10^2\ ^{+1.2 \times 10^2}_{-5.7 \times 10^2}$
588015507661127686	0.7857	33 ± 1	$4.1 \times 10^3 \pm 1.2 \times 10^3$	44.90 ± 0.03	$1.4 \times 10^2\ ^{+27}_{-22}$	$2.0 \times 10^2\ ^{+4.2 \times 10^2}_{-1.6 \times 10^2}$
588015507666829383	0.7533	$2.5 \times 10^2 \pm 32$	$2.1 \times 10^3 \pm 1.5 \times 10^2$	45.08 ± 0.02	$1.8 \times 10^2\ ^{+35}_{-29}$	$4.4 \times 10^2\ ^{+3.7 \times 10^2}_{-3.6 \times 10^2}$
588015508192165993	0.7715	27 ± 2	$2.4 \times 10^3 \pm 1.5 \times 10^2$	45.09 ± 0.02	$1.9 \times 10^2\ ^{+38}_{-31}$	$58^{+7.1 \times 10^2}_{-5}$
588015508195049640	0.7018	63 ± 10	$1.35 \times 10^4 \pm 4.1 \times 10^3$	43.6 ± 0.4	17^{+16}_{-8}	11^{+66}_{-6}
588015508195901596	0.7062	28 ± 10	$3.3 \times 10^3 \pm 1.3 \times 10^3$	44.30 ± 0.05	52^{+10}_{-8}	$51^{+1.8 \times 10^2}_{-36}$
588015508202258589	0.7328	$2.3 \times 10^3 \pm 5.8 \times 10^2$	47 ± 2	44.9 ± 0.2	$1.5 \times 10^2\ ^{+1.1 \times 10^2}_{-59}$	$3.9 \times 10^2\ ^{+2.7 \times 10^2}_{-3.5 \times 10^2}$
588015508205273127	0.7995	41 ± 2	$5.6 \times 10^3 \pm 3.7 \times 10^2$	45.07 ± 0.03	$1.8 \times 10^2\ ^{+39}_{-31}$	$7.4 \times 10^2\ ^{+68}_{-6.8 \times 10^2}$
588015508210647058	0.771	21 ± 3	$4.2 \times 10^3 \pm 1.0 \times 10^3$	45.03 ± 0.03	$1.7 \times 10^2\ ^{+36}_{-29}$	$1.2 \times 10^2\ ^{+6.4 \times 10^2}_{-71}$
588015508212089028	0.8121	35 ± 4	$4.6 \times 10^3 \pm 1.5 \times 10^3$	43.8 ± 0.4	22^{+21}_{-10}	19^{+80}_{-13}
588015508213989529	0.8119	55 ± 4	$2.5 \times 10^3 \pm 1.1 \times 10^3$	44.85 ± 0.07	$1.3 \times 10^2\ ^{+35}_{-26}$	$2.3 \times 10^2\ ^{+3.3 \times 10^2}_{-2.0 \times 10^2}$
588015508214906936	0.7227	88 ± 5	$1.0 \times 10^4 \pm 2.8 \times 10^3$	44.88 ± 0.03	$1.3 \times 10^2\ ^{+25}_{-21}$	$2.2 \times 10^2\ ^{+3.5 \times 10^2}_{-1.7 \times 10^2}$
588015508457717826	0.8166	46 ± 4	$1.2 \times 10^3 \pm 1.1 \times 10^3$	44.90 ± 0.06	$1.4 \times 10^2\ ^{+34}_{-26}$	$68^{+5.3 \times 10^2}_{-29}$
588015508726481000	0.7324	24 ± 4	$2.3 \times 10^3 \pm 3.9 \times 10^3$	44.2 ± 0.2	44^{+21}_{-13}	$65^{+1.3 \times 10^2}_{-53}$
588015508728381656	0.7956	28 ± 2	$4.9 \times 10^3 \pm 9.2 \times 10^2$	45.19 ± 0.03	$2.2 \times 10^2\ ^{+50}_{-40}$	$2.0 \times 10^2\ ^{+7.8 \times 10^2}_{-1.3 \times 10^2}$
588015508729364533	0.8014	32 ± 1	$4.1 \times 10^3 \pm 3.3 \times 10^2$	45.31 ± 0.06	$2.6 \times 10^2\ ^{+78}_{-59}$	$8.3 \times 10^2\ ^{+3.6 \times 10^2}_{-5.7 \times 10^2}$
588015508732510294	0.703	24 ± 1	$4.1 \times 10^3 \pm 1.3 \times 10^3$	45.3 ± 0.3	$2.7 \times 10^2\ ^{+2.7 \times 10^2}_{-1.3 \times 10^2}$	$8.8 \times 10^2\ ^{+3.5 \times 10^2}_{-6.2 \times 10^2}$
588015508739915785	0.7375	21 ± 2	$2.5 \times 10^3 \pm 5.6 \times 10^2$	45.22 ± 0.02	$2.3 \times 10^2\ ^{+45}_{-37}$	$65^{+0.7 \times 10^2}_{-0.3}$
588015508748173447	0.7706	31 ± 3	$3.9 \times 10^3 \pm 1.0 \times 10^3$	44.84 ± 0.02	$1.3 \times 10^2\ ^{+21}_{-18}$	$5.7 \times 10^2\ ^{+0.3}_{-5.2}$
588015508752433223	0.705	23 ± 2	$3.0 \times 10^3 \pm 6.4 \times 10^2$	44.98 ± 0.02	$1.6 \times 10^2\ ^{+29}_{-24}$	$115.4815^{+588.1607}_{-71.4742}$

Table 5
(Continued)

Object[a]	z[b]	EW(Mg II)/Å [c]	$\frac{\mathrm{FWHM(H}\beta)}{1000\ \mathrm{km\ s^{-1}}}$ [d]	$\log\left[\frac{\lambda L_\lambda(5100\ \text{Å})}{\mathrm{erg\ s^{-1}}}\right]$	$\frac{R_{\mathrm{BLR,Kaspi}}}{\mathrm{lightdays}}$ [e]	$\frac{R_{\mathrm{BLR}}}{\mathrm{lightdays}}$ [f]
588015508757151947	0.7991	26 ± 3	$3.2 \times 10^3 \pm 2.2 \times 10^3$	44.90 ± 0.04	$1.4 \times 10^2\ ^{+29}_{-23}$	$82^{+5.4 \times 10^2}_{-43}$
588015509273378959	0.8024	30 ± 7	$3.9 \times 10^3 \pm 2.0 \times 10^3$	44.30 ± 0.08	52^{+13}_{-10}	$62^{+1.7 \times 10^2}_{-48}$
588015509274427525	0.8246	32 ± 5	$4.1 \times 10^3 \pm 1.8 \times 10^3$	45.04 ± 0.03	$1.7 \times 10^2\ ^{+35}_{-28}$	$1.9 \times 10^2\ ^{+5.8 \times 10^2}_{-1.4 \times 10^2}$
588015509275803698	0.7189	32 ± 1	$5.0 \times 10^3 \pm 1.0 \times 10^3$	45.446 ± 0.007	$3.3 \times 10^2\ ^{+66}_{-55}$	$2.2 \times 10^2\ ^{+1.3 \times 10^3}_{-1.3 \times 10^2}$
588015509281767465	0.838	47 ± 2	$6.9 \times 10^3 \pm 1.6 \times 10^3$	45.46 ± 0.05	$3.4 \times 10^2\ ^{+99}_{-75}$	$3.9 \times 10^2\ ^{+1.0 \times 10^2}_{-2.9 \times 10^2}$
588015509283930145	0.8222	26 ± 1	$2.9 \times 10^3 \pm 5.4 \times 10^2$	45.12 ± 0.04	$2.0 \times 10^2\ ^{+45}_{-36}$	$7.9 \times 10^2\ ^{+92}_{-5.7 \times 10^2}$
588015509288058920	0.7654	32 ± 1	$5.1 \times 10^3 \pm 9.8 \times 10^2$	45.107 ± 0.008	$1.9 \times 10^2\ ^{+32}_{-28}$	$8.5 \times 10^2\ ^{+12}_{-8.0 \times 10^2}$
588015509288517766	0.7494	33 ± 1	$4.8 \times 10^3 \pm 4.1 \times 10^2$	44.88 ± 0.01	$1.3 \times 10^2\ ^{+21}_{-18}$	$1.7 \times 10^2\ ^{+4.3 \times 10^2}_{-1.3 \times 10^2}$
588015509291532453	0.7013	20 ± 3	$2.7 \times 10^3 \pm 2.9 \times 10^3$	44.2 ± 0.2	43^{+18}_{-12}	$42^{+1.5 \times 10^2}_{-30}$
588015509804875792	0.8272	23 ± 2	$3.0 \times 10^3 \pm 7.1 \times 10^2$	45.1 ± 0.1	$1.9 \times 10^2\ ^{+79}_{-53}$	$3.8 \times 10^2\ ^{+4.8 \times 10^2}_{-3.2 \times 10^2}$
588015509812871367	0.7565	27 ± 6	$5.3 \times 10^3 \pm 1.6 \times 10^3$	44.05 ± 0.08	35^{+8}_{-6}	$28^{+1.3 \times 10^2}_{-18}$
588015509813198910	0.7032	49 ± 1	$5.0 \times 10^3 \pm 7.1 \times 10^2$	45.522 ± 0.005	$3.7 \times 10^2\ ^{+76}_{-63}$	$1.3 \times 10^2\ ^{+7}_{-3.0 \times 10^2}$
588015509815361541	0.7711	53 ± 2	$3.7 \times 10^3 \pm 6.5 \times 10^2$	44.93 ± 0.01	$1.4 \times 10^2\ ^{+23}_{-20}$	$4.2 \times 10^2\ ^{+2.3 \times 10^2}_{-3.7 \times 10^2}$
588015509816213721	0.8112	71 ± 8	$6.3 \times 10^3 \pm 1.9 \times 10^3$	45.05 ± 0.03	$1.7 \times 10^2\ ^{+38}_{-31}$	72^{+40}_{-22}
588015509818114095	0.7647	41 ± 2	$6.5 \times 10^3 \pm 7.3 \times 10^2$	45.13 ± 0.02	$2.0 \times 10^2\ ^{+38}_{-3}$	$1.9 \times 10^2\ ^{+7.0 \times 10^2}_{-1.3 \times 10^2}$
588015509818310681	0.7586	35 ± 2	$5.1 \times 10^3 \pm 8.9 \times 10^2$	45.08 ± 0.01	$1.8 \times 10^2\ ^{+32}_{-27}$	$2.0 \times 10^2\ ^{+6.3 \times 10^2}_{-1.4 \times 10^2}$
588015509827420352	0.7534	30 ± 4	...	43.61 ± 0.4	18^{+16}_{-8}	7^{+75}_{-2}
588015510337159227	0.7196	39 ± 2	$2.0 \times 10^3 \pm 3.7 \times 10^2$	45.201 ± 0.009	$2.2 \times 10^2\ ^{+40}_{-34}$	$937.5204^{+65.1546}_{-874.5104}$
588015510340632684	0.7078	29 ± 2	$3.1 \times 10^3 \pm 5.4 \times 10^2$	45.07 ± 0.01	$1.8 \times 10^2\ ^{+32}_{-27}$	$4.2 \times 10^2\ ^{+4.0 \times 10^2}_{-3.6 \times 10^2}$
588015510340960369	0.7156	24 ± 2	$4.0 \times 10^3 \pm 2.8 \times 10^2$	45.02 ± 0.07	$1.7 \times 10^2\ ^{+48}_{-36}$	$4.0 \times 10^2\ ^{+3.5 \times 10^2}_{-3.5 \times 10^2}$
588015510355837082	0.7128	35 ± 3	$1.2 \times 10^3 \pm 2.6 \times 10^3$	44.8 ± 0.1	$1.2 \times 10^2\ ^{+41}_{-30}$	$2.1 \times 10^2\ ^{+3.5 \times 10^2}_{-1.7 \times 10^2}$
588015510356689027	0.748	70 ± 17	$6.3 \times 10^3 \pm 3.3 \times 10^3$	44.1 ± 0.2	37^{+15}_{-10}	76^{+89}_{-65}
588015510361014492	0.7497	84 ± 40	$1.3 \times 10^3 \pm 1.2 \times 10^3$	44.14 ± 0.04	40^{+6}_{-5}	$42^{+1.4 \times 10^2}_{-31}$
588015510365601830	0.8007	14 ± 2	$1.7 \times 10^3 \pm 3.9 \times 10^3$	44.94 ± 0.08	$1.5 \times 10^2\ ^{+44}_{-33}$	$83^{+5.8 \times 10^2}_{-42}$

Notes.
[a] `headobjid` from SDSS tables.
[b] Redshift.
[c] Rest frame equivalent width of broad line.
[d] FWHM of broad line.
[e] Computed from Kaspi relation, in rest frame.
[f] Own computation from all points within the 68% CI, in rest frame.

whether photometric reverberation mapping is feasible. Having a method to evaluate such data enables us to apply reverberation mapping for the first time to large samples of a few hundred AGNs at far higher redshifts than before.

We set out to obtain individual and ensemble estimates of the BLR size in quasars, and on that basis explore their M_{BH}. We did this by means of photometric reverberation mapping, drawing on the existing data in SDSS S82. Our results show the power of stochastical broadband reverberation mapping techniques of quasar ensembles, in contrast to classical spectroscopic monitoring of individual objects. This enables us to use available long-term surveys. We present novel relationships between spectrophotometric parameters allowing one to calculate ensemble estimates of AGN central black hole masses, computed by an improved reverberation mapping method and carried out on S82 for the first time.

We model the continuum in one band as stochastic Gaussian process and assume a flux model that describes the other band with emission line contribution as a scaled version of the pure continuum band plus a smoothed and displaced version of the continuum that was generated using a δ function transfer function. The evaluation is carried out by stochastic methods. This approach not only interpolates between data points, but also makes and includes self-consistent estimates, where statistical confidence limits on all estimated parameters are determined. It also is able to simultaneously derive the lags of multiple emission lines.

By generating and evaluating extensive sets of problem-specific mock data, we made sure that our model sufficiently fits the continuum light curve and in a second step, the continuum plus emission light curve in order to solve for the time delay. We found a method to estimate whether time lags in the range of the expected can be determined in principle from a given light curve with respect to its time sampling. This is necessary for making sure that we can trust our estimates. This also greatly reduces computation time.

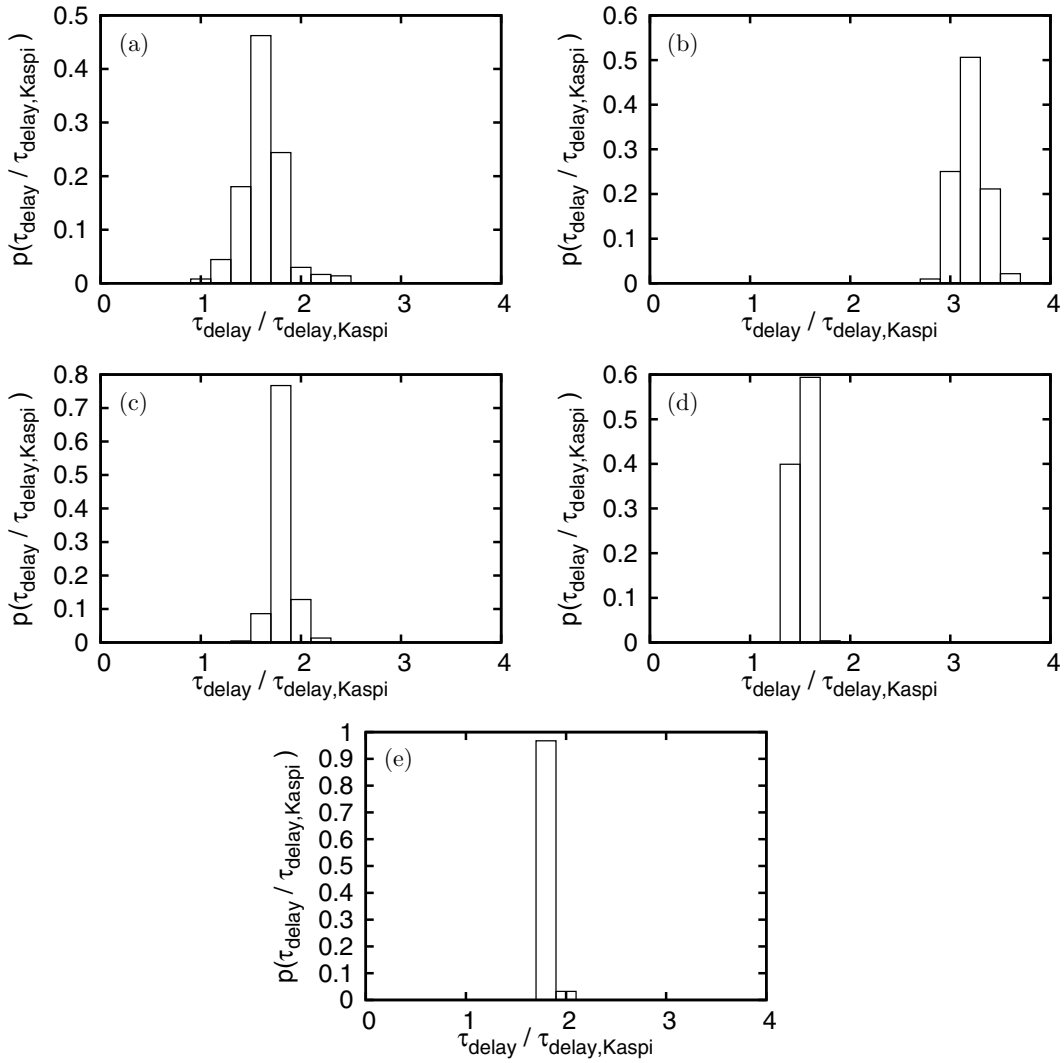

Figure 7. Marginalized ensemble PDFs for comparison of the delays inferred here to those from the Kaspi relation (40) for different subsamples and emission lines. For each subsample, the redshift, emission lines, and band used for the continuum are given. (a) Sample 1: $z = 0.225$–0.291, with i band: Hα, z band: continuum (29 light curves). (b) Sample 1: $z = 0.225$–0.291, with r band: Hβ, Hγ (plus some other), g band: continuum (17 light curves). (c) Sample 2: $z = 0.555$–0.591, with g band Mg II, r: continuum (68 light curves). (d) Sample 3: $z = 0.592$–0.6999, with g-band Mg II (Fe II λ2600), r continuum (111 light curves). (e) Sample 4: $z = 0.7$–0.846, with g-band Mg II (Fe II λ2600), r continuum (115 light curves)

In the application to SDSS S82 data, we combine on average more than 60 epochs of photometric data with one epoch of spectroscopy. In all bandpasses the accretion disk emission (the continuum) contributes much of the flux, but in some bands, the BLR line flux contributes up to 15%. Constraining spectroscopic broadband information is provided for the Hα, Hβ, and Mg II lines.

We identified the SDSS S82 temporal sampling windows as a serious issue. Despite the fact that the stochastic approach is very good in dealing with uneven and sparse time sampling, the sampling windows make it necessary to pre-select sufficient light curves before evaluating them. This is necessary because data usually only exists for 2–3 months within each year. In addition, we identified suitable redshift ranges to get, at minimum, one band that is emission-line free and one having contribution from Hα, Hβ, or Mg II. For SDSS-like mock data, we were able to show that the method should work for the application to individual AGNs, so we can trust in our estimates for $\tau_{\rm delay}$ from SDSS S82 light curves.

We estimated the time delay $\tau_{\rm delay}$ for a well-defined sample of 323 objects spanning redshifts from $z = 0.225$–0.846. In detail, we evaluated 29 light curves in the redshift range $z = 0.225$–0.291, with i band: Hα, z band: continuum. We evaluated 68 light curves in the redshift range $z = 0.555$–0.591 with g-band Mg II, r: continuum. We evaluated 111 light curves in the redshift range $z = 0.592$–0.6999, with g-band Mg II (Fe II λ2600), r continuum. In the redshift range $z = 0.7$–0.846, we evaluated 115 light curves with g-band Mg II (Fe II λ2600), r continuum. The Tables 2–5 show detailed information about the four subsamples and the results of individual objects.

Seventeen light curves out of the redshift range $z = 0.225$–0.291 were also evaluated with r band: Hβ, Hγ (plus some other), g band: continuum. From this, we get no sensible results. Even when omitting light curves with clearly unreliable posterior PDF, the PDF tends to the prior cutoff at $\tau_{\rm delay}/\tau_{\rm delay,expected} = 4$. Also, it is troubling that the Hβ BLR comes out larger than the Hα BLR, in light of other results (Bentz et al. 2010). One reason for this could be the mostly

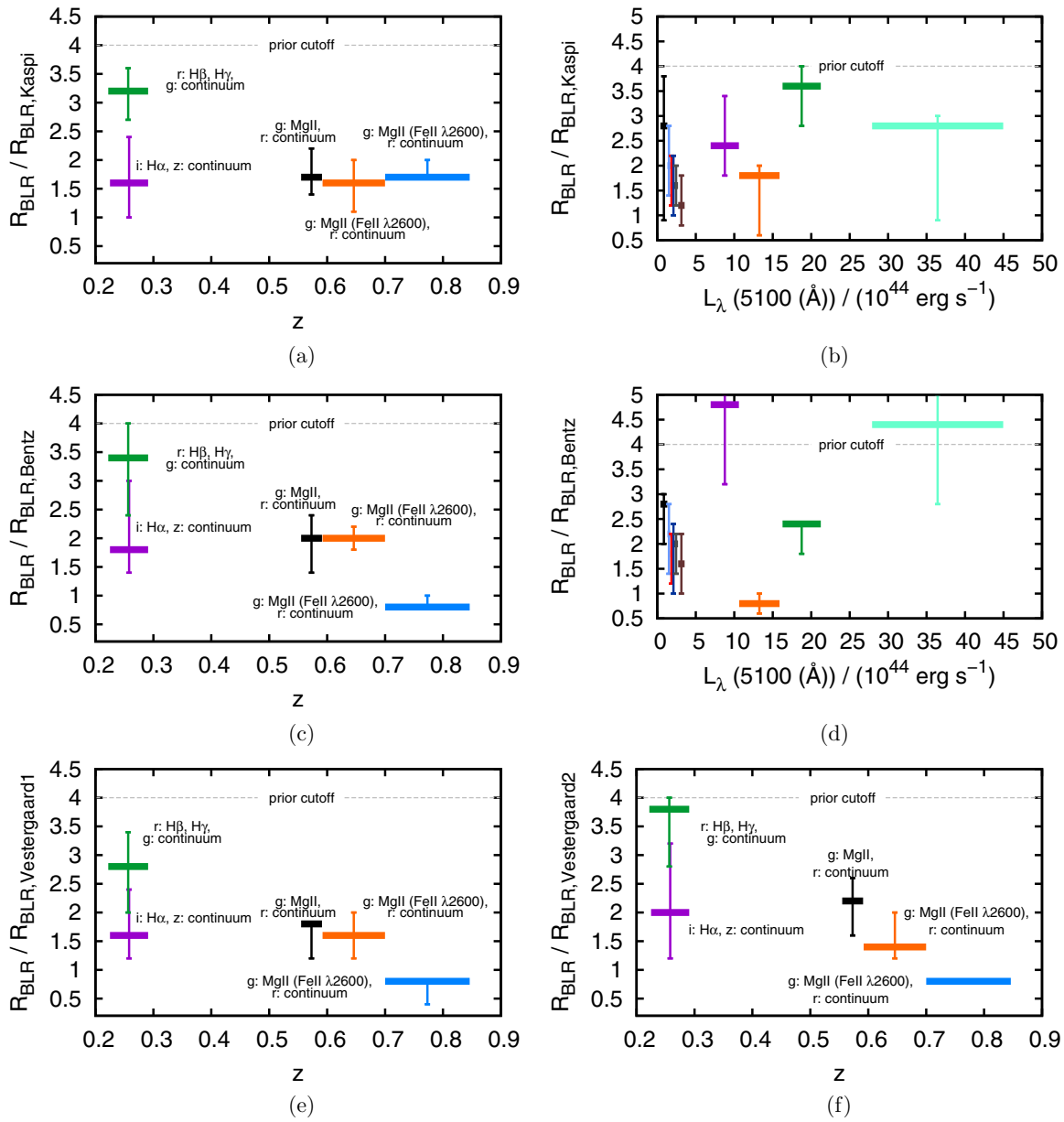

Figure 8. Comparing our results to Kaspi et al. (2000), Bentz et al. (2013), and Vestergaard (2002): (a) ensemble $R_{\rm BLR}/R_{\rm BLR,Kaspi}$ binned by redshift, (b) ensemble $R_{\rm BLR}/R_{\rm BLR,Kaspi}$ binned by luminosity, (c) ensemble $R_{\rm BLR}/R_{\rm BLR,Bentz}$ binned by redshift, (d) ensemble $R_{\rm BLR}/R_{\rm BLR,Bentz}$ binned by luminosity, (e) ensemble $M_{\rm BH}/M_{\rm BH,Vestergaard1}$ binned by redshift, (f) ensemble $M_{\rm BH}/M_{\rm BH,Vestergaard2}$ binned by redshift. Bins are colored for the sake of clarity. Each color indicates the same bin for all diagrams showing binning by z. Each color indicates the same bin for all diagrams showing binning by luminostiy. For z bins, the used bands and their broad emission lines along with contaminating lines are also given.

weak Hβ, together with contribution from Hγ and O III λ4959, λ5007, so our assumption of having most contribution from Hβ doesn't hold.

The posterior distribution functions of the fit parameters for ensembles of these objects where evaluated by multiplying them for sensible redshift or luminosity bins. As a result, we get an ensemble scaling relationship for the scaling of the BLR size as a function of luminosity and redshift. We are also able to give constraints on the scaling relationship between the central black hole masses and the luminosity of the AGN. Comparing our results with comparable published data by Kaspi et al. (2000), Vestergaard (2002), and Bentz et al. (2013), we find that the proportionality constant is significantly bigger than those published before, but S82 data makes the result, and its implication, tentative.

It is important to note that the $L - R_{\rm BLR}$ and $L - M_{\rm BH}$ relationships and their quoted uncertainties stem from the ensemble average of many objects. The uncertainties associated with individual $M_{\rm BH}$ estimates may be considerably higher.

We have shown that the robustness of our method is limited by time sampling. Presuming the Kaspi relation with factor one is true, the $\tau_{\rm delay}$ should fall into a region where we can recover them, as this was one of the selection criteria. Assuming that the Kaspi relation has to be scaled by a factor—as our results indicate—the inferred $\tau_{\rm delay}$ are no longer falling into regions of the time sampling that are well covered. In such cases, the correct inference may occur due to the interpolation, but cannot be trusted. From further analysis, most of the individual $\tau_{\rm delay}$ fall in regions were less than 50 percent of the time delays are assumed to be calculated correctly.

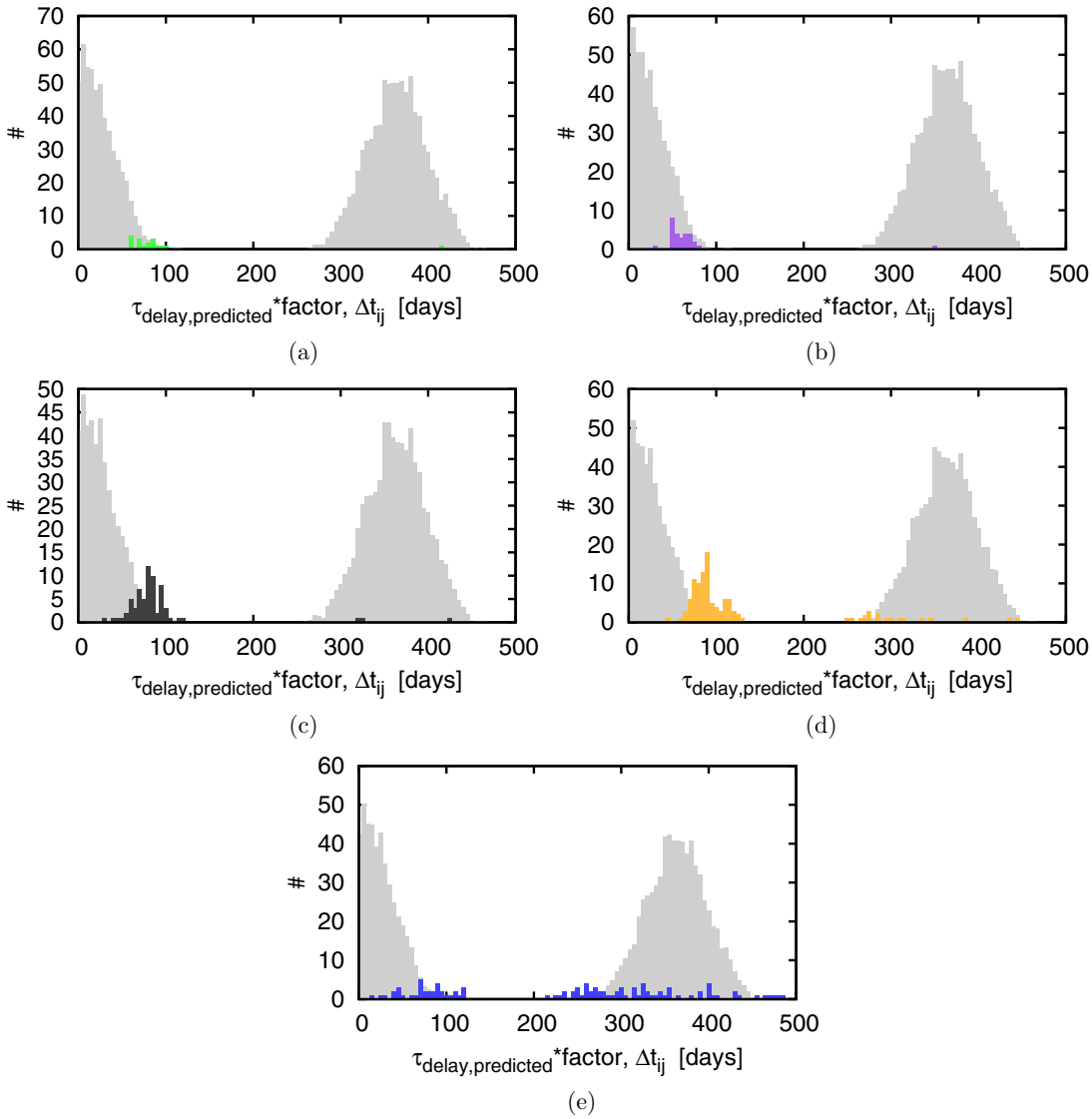

Figure 9. Gray histograms indicate the ensemble-mean observational time lag distribution for the light curves in each redshift bin used to calculate the ensemble relation; this histogram indicates (see Figure 5) the regime for τ_{delay} where the value can be robustly recovered. The various colored histograms indicate the distribution of the predicted τ_{delay} from the Kaspi relation scaled by the proportionality factor as we inferred from the data (see Figure 8(a)) in the different redshift bins. A comparison of the gray and colored histograms shows that, except for perhaps (b) and (e) the S82 sampling is expected to seriously affect the robustness of the formally inferred time delays. (a) *r*: Hβ, Hγ, *g*: continuum, (b) *i*: Hα, *z*: continuum, (c) *g*: Mg II, *r*: continuum, (d) *g*: Mg II (Fe II λ2600), *r*: continuum, (e) *g*: Mg II (Fe II λ2600), *r*: continuum.

The formalism developed here should be useful for application to future data sets.

As we use constraining single-epoch spectra, an extension to apply the method to more spectra for given objects may be interesting. For some AGNs, SDSS provides multi-epoch spectra, where we have seen that their emission lines vary significantly in some cases.

Another useful extension would be to add the information that light-curve properties lead to good τ_{delay} estimate and give different weights for the ensemble PDF, instead of excluding some and weighing the remaining equally.

It would be interesting to introduce a wider range of transfer functions. We derived the formalism for dealing with not only a δ function but also a Gaussian. However, the Gaussian transfer function couldn't be applied here because it cannot be applied easily to the power-law structure function model for reasons of non-analytical integrals. For application to a DRW, we get analytical integrals, but the DRW doesn't work well for photometric reverberation of SDSS S82 light curves. For this reason, the implementation of additional transfer functions like the top-hat or sawtooth function, as used by some authors, would be useful. We know that not all parts of an emission line vary. To deal with this issue, we use the information on the broad emission line provided by the *Catalog of Quasar Properties*, in detail, the line luminosity, FWHM, and rest frame equivalent with the broad emission lines. It might be feasible to better include the fact that not all parts of an emission line vary, since up to now the prediction of equivalent widths from given (e, s) scaling factors for calculating L_{spec}. This should be a minor effect, though, because the line profile looks very similar between the mean spectrum and the RMS spectrum, where the RMS is over spectra taken at different times (Kaspi et al. 2000).

Whereas the *Catalog of Quasar Properties* provides information on the broad component of Hα, Hβ, Mg III, and we use them, for C IV, only information about the whole line is available. As no information on the FWHM of the broad component

of C IV is available from the catalog (Shen et al. 2011), no comparison to the third Vestergaard relation (see Equation (7) in Vestergaard & Peterson 2006) could be done. This might be carried out with data from upcoming surveys.

The research leading to these results received funding from the European Research Council under the European Union's Seventh Framework Programme (FP 7) ERC Grant Agreement No. [321035]. Jo Bovy was supported by NASA through Hubble Fellowship grant HST-HF-51285.01 from the Space Telescope Science Institute, which is operated by the Association of Universities for Research in Astronomy, Incorporated, under NASA contract NAS5-26555.

APPENDIX A

THE STRUCTURE FUNCTION AND THE GAUSSIAN PROCESS

Imagine a set of N measurements m_i, with calibrated magnitude or flux measurements all taken in a single bandpass of a single source. Each measurement m_i is taken at a time t_i and has an (presumed known) uncertainty variance σ_i. The structure function $V(|\Delta t|)$ is defined as follows. The expectation value $E[\cdot]$ for the difference between the observation m_i and m_j (with $i \neq j$) is

$$E[(m_i - m_j)^2] = \sigma_i^2 + \sigma_j^2 + V(|t_i - t_j|), \tag{A1}$$

where the observations are presumed to be (from a measurement noise perspective) independent, and the structure function $V(\cdot)$ effectively describes the variance. In the literature, the structure function has occasionally been defined in terms of the root-mean square (the square root of the above definition) and sometimes in terms of the mean absolute differences, which is slightly different again.

A Gaussian process is characterized by a function describing the mean measurement $\bar{\mathbf{m}}(t)$ (magnitude or flux) as a function of time t and a function $C(t, t')$, describing the covariance between observations $\mathbf{m}$ at different epochs t and t'. We will assume that the mean is constant and that the process is stationary, such that $C(t, t') \equiv C(t - t')$. The probability of a set of N observations $\{m_i\}_{i=1}^N$ is given by that of the N-dimensional Gaussian with mean $\bar{\mathbf{m}} = (m, m, ..., m)^{\mathrm{T}}$ and $N \times N$ dimensional covariance matrix C with elements $C_{ij} = C(t_i - t_j)$. It is possible to define a Gaussian process that generates data in accordance with any (reasonable) structure function. As the structure function is the expectation of the squared measurement differences between observations t_i and t_j separated by a time Δt, we can write it as (Rybicki & Press 1992)

$$\begin{aligned} V(|\Delta t|) &= E[(m(t) - m(t + \Delta t))^2] \\ &= 2E[(m(t) - E[m])^2] - 2E[(m(t) \\ &\quad - E[m])(m(t + \Delta t) - E[m]] \end{aligned} \tag{A2}$$

and

$$V_{ij} \equiv \frac{1}{2} V(|t_i - t_j|) \tag{A3}$$

$$V_\infty = \frac{1}{2} V(\Delta t \to \infty). \tag{A4}$$

The covariance function of the Gaussian process corresponding to the structure function V with parameters $\mathbf{p}$ is then given by $C_{ij} = V_\infty - V_{ij}$, or expanded

$$\begin{aligned} C &= C(t, \mathbf{p}, \sigma) \\ &= \begin{pmatrix} \left(V_\infty + \sigma_1^2\right) & (V_\infty - V_{12}) & (V_\infty - V_{13}) & \dots & (V_\infty - V_{1N}) \\ (V_\infty - V_{21}) & \left(V_\infty + \sigma_2^2\right) & (V_\infty - V_{23}) & \dots & (V_\infty - V_{2N}) \\ (V_\infty - V_{31}) & (V_\infty - V_{32}) & \left(V_\infty + \sigma_3^2\right) & \dots & (V_\infty - V_{3N}) \\ \dots & \dots & \dots & \dots & \dots \\ (V_\infty - V_{N1}) & (V_\infty - V_{N2}) & (V_\infty - V_{N3}) & \dots & \left(V_\infty + \sigma_N^2\right) \end{pmatrix}. \end{aligned} \tag{A5}$$

To get the effective (observed) variability, the photometric uncertainty variances σ_i are added to the diagonal elements of C. Variability models can therefore be expressed either in terms of the variance function or equivalently in terms of the structure function. For example, imagine that the two quantities m_i and m_j are not observations of a quasar, but instead random numbers drawn from an N-dimensional Gaussian,

$$p(\mathbf{m}) = N(\mathbf{m}|\bar{\mathbf{m}}, C), \tag{A6}$$

$$\mathbf{m} = (m_1, m_2, m_3, ..., m_N)^{\mathrm{T}}, \quad \bar{\mathbf{m}} = (\bar{m}, \bar{m}, \bar{m}, ..., \bar{m})^{\mathrm{T}} \tag{A7}$$

where we have assembled the observations into a column vector $\mathbf{m}$. $N(\cdot|\bar{\mathbf{m}}, C)$ is the general normal or Gaussian PDF, given mean vector $\bar{\mathbf{m}}$ and a variance tensor C, $\bar{m}$ is an arbitrary parameter, $2V_{ij}$ is the structure function evaluated at time lag $|t_i - t_j|$ as defined above. If we make many draws from this Gaussian, the expectation values of $(m_i - m_j)$ and $(m_i - m_j)^2$ for any pair of measurements m_i and m_j (with $i \neq j$) are just

$$E[(m_i - m_j)] = 0 \tag{A8}$$

and

$$E[(m_i - m_j)^2] = \sigma_i^2 + \sigma_j^2 + V(|t_i - t_j|), \tag{A9}$$

which, by design, is equivalent to the description of the structure function.

Two additional points arise from this description. Although m does not enter in the prediction of the mean or variance of the magnitude differences, it does, of course, affect the magnitude. So it is, in principle, an observational property of the model. Although V_∞ is not measurable, it can be approximated by evaluating the structure function at a large time lag.

A.1. The Basic Stochastic Approach

The idea behind this approach was developed by Press & Rybicki (1992), Rybicki & Press (1992), and Rybicki & Kleyna (1994) in order to estimate the best-fit structure function parameters for a given light curve. Later on this was extended by Zu et al. (2011) and Chelouche & Daniel (2012) to a method that enables both structure-function parameter estimation and estimation of the time delay between multiple uneven sampled light curves. Here, we refer to the method from Zu et al. (2011) and re-summarize some of its formalism. We present how we have improved it to do broadband reverberation mapping, supported by one epoch of spectroscopy to separate continuum and emission line contribution, as well as their application.

The intrinsic variability has a covariance matrix $S = \langle \mathbf{ss} \rangle$, whereas the noise has a covariance matrix $N = \langle \mathbf{nn} \rangle$. By definition, we know that

$$P(\mathbf{s}) \propto |S|^{-1/2} \exp\left(-\frac{\mathbf{s}^{\mathrm{T}} S^{-1} \mathbf{s}}{2}\right) \tag{A10}$$

and that

$$P(\mathbf{n}) \propto |N|^{-1/2} \exp\left(-\frac{\mathbf{n}^{\mathrm{T}} N^{-1} \mathbf{n}}{2}\right). \tag{A11}$$

Thus, the probability of the data given the linear coefficients $\mathbf{q}$, the intrinsic light curve $\mathbf{s}$, and any other parameters of the light curve model $\mathbf{p}$ (the structure function parameters) is

$$P(\mathbf{m}|\mathbf{q}, \mathbf{s}, \mathbf{p}) \propto |SN|^{-1/2} \int d^n \mathbf{n} S(\mathbf{m} - (\mathbf{s} + \mathbf{n} + L\mathbf{q})) \times \exp\left(-\frac{\mathbf{s}^{\mathrm{T}} S^{-1} \mathbf{s} + \mathbf{n}^{\mathrm{T}} N^{-1} \mathbf{n}}{2}\right). \tag{A12}$$

After evaluating the Dirac δ function, we complete the squares in the exponential with respect to both the unknown intrinsic source variability $\mathbf{s}$ and the linear coefficients $\mathbf{q}$.

This determines our best estimate for the mean light curve,

$$\hat{\mathbf{p}} = SC^{-1}(\mathbf{m} - L\hat{\mathbf{q}}) \tag{A13}$$

with linear coefficients

$$\hat{\mathbf{q}} = (L^{\mathrm{T}} C^{-1} L)^{-1} L^{\mathrm{T}} C^{-1} \mathbf{m} \equiv C_q L^{\mathrm{T}} C^{-1} \mathbf{m}. \tag{A14}$$

$C = S + N$ is the overall covariance matrix of the data and $C_q \equiv (L^{\mathrm{T}} C^{-1} L)^{-1}$. With these definitions, we can factor the argument of the exponential into

$$P(\mathbf{m}|\mathbf{q}, \mathbf{s}, \mathbf{p}) \propto |SN|^{-1/2} \times \exp\left(-\frac{\Delta\mathbf{s}^{\mathrm{T}}(S^{-1} + N^{-1})\Delta\mathbf{s}}{2} - \frac{\Delta\mathbf{q}^{\mathrm{T}} C_q^{-1} \Delta\mathbf{q}}{2} - \frac{\mathbf{m}^{\mathrm{T}} C_{\perp}^{-1} \mathbf{m}}{2}\right), \tag{A15}$$

where

$$C_{\perp}^{-1} \equiv C^{-1} - C^{-1} L C_q L^{\mathrm{T}} C^{-1} \tag{A16}$$

is the component of the covariance matrix C that is orthogonal to the fitted linear functions. The variances in the linear parameters are

$$\langle \Delta\mathbf{q}^2 \rangle = (L^{\mathrm{T}} C^{-1} L)^{-1} \equiv C_q, \tag{A17}$$

$$\Delta\mathbf{s} = \mathbf{s} - \hat{\mathbf{s}}, \tag{A18}$$

$$\Delta\mathbf{q} = \mathbf{q} - \hat{\mathbf{q}}. \tag{A19}$$

We are now prepare to marginalize the probability over the light curve $\mathbf{s}$ and the linear parameters $\mathbf{q}$ under the assumption of uniform priors for these variables. When doing so, we find that

$$P(\mathbf{m}|\mathbf{p}) \propto \mathcal{L}(\mathbf{m}|\mathbf{p}) \equiv |S + N|^{-1/2} |L^{\mathrm{T}} C^{-1} L|^{-1/2} \times \exp\left(-\frac{\mathbf{m}^{\mathrm{T}} C_{\perp}^{-1} \mathbf{m}}{2}\right), \tag{A20}$$

where for the exponential model the remaining parameters $\mathbf{p}$ are τ and ω, and for the power-law model A and γ. $\mathcal{L}$ represents the likelihood function we need to maximize in order to find the most likely combination of those parameters.

Mathematically, the mean light curve is the weighted average of all process light curves described by the parameter vector $\mathbf{p}$ being statistically consistent with the data, and the variance is the scatter of these light curves about the mean.

The main advantage of this approach is that it not only does interpolation between data points, but also estimates the uncertainties in the interpolation. Figure 10 shows two typical examples of SDSS S82 quasar light curves fitted by the stochastic process.

Following Zu et al. (2011), there are two important points to consider when comparing these light curve reconstructions and the error snakes defined by the variances to the data points. First, these are variances in the mean light curve and not the variance of the data relative to the mean light curve. The latter quantity is defined only when there is data and so it is ill suited for showing a continuous light curve. Data points will be scattered relative to the mean light curve by the combination of the variance in the mean light curve and uncertainties in the individual data points. Second, the reconstructed light curve is not an example of an individual light curve defined by the structure function parameters of the underlying model, but rather the average of all light curves defined by the structure function parameters that are consistent with the observed light curve given its uncertainties.

The variance in the reconstructed light curve is then the variance of these individual light curves about the mean. If we generated individual realizations of light curves each constrained by the data, they would track the mean light curve and statistically stay inside the error snake defined by the variances, but would show much more structure on short timescales and excursions outside the error snakes consistent with the estimated variances.

This approach can now easily be extended for the purpose of estimating a time delay τ_{delay} between two (or more) light curves in order to estimate the size of the BLRs in AGNs. An approach for reverberation mapping based on this was first outlined by Zu et al. (2011), and was enhanced in this work to do broadband reverberation mapping, supported by one epoch of spectroscopy to separate continuum and emission line contribution, and to use the power law instead of the DRW.

APPENDIX B

REVERBERATION MAPPING COVARIANCE MATRIX ELEMENTS

In the case of a *δ-function transfer function*, one gets the following equations:

for the power-law model:

1. covariance matrix for autocorrelation of the k band flux:

$$C_{ij} = C_{kk}^{cc} = \left\langle f_k^c(t_i) f_k^c(t_j) \right\rangle = A^2 \left[\left(\frac{t_{\mathrm{obs}}}{1\ \mathrm{yr}} \right)^{\gamma} - \frac{1}{2} \left(\frac{|t_i - t_j|}{1\ \mathrm{yr}} \right)^{\gamma} \right] \tag{B1}$$

2. covariance matrix for the correlation function between k-band flux and l-band flux:

$$C_{ij} = C_{kl}^{c,(e+c)} = \left\langle f_k^c(t_i) f_l^{ec}(t_j) \right\rangle = s\ A^2 \left[\left(\frac{t_{\mathrm{obs}}}{1\ \mathrm{yr}} \right)^{\gamma} - \frac{1}{2} \left(\frac{|t_i - t_j|}{1\ \mathrm{yr}} \right)^{\gamma} \right]$$

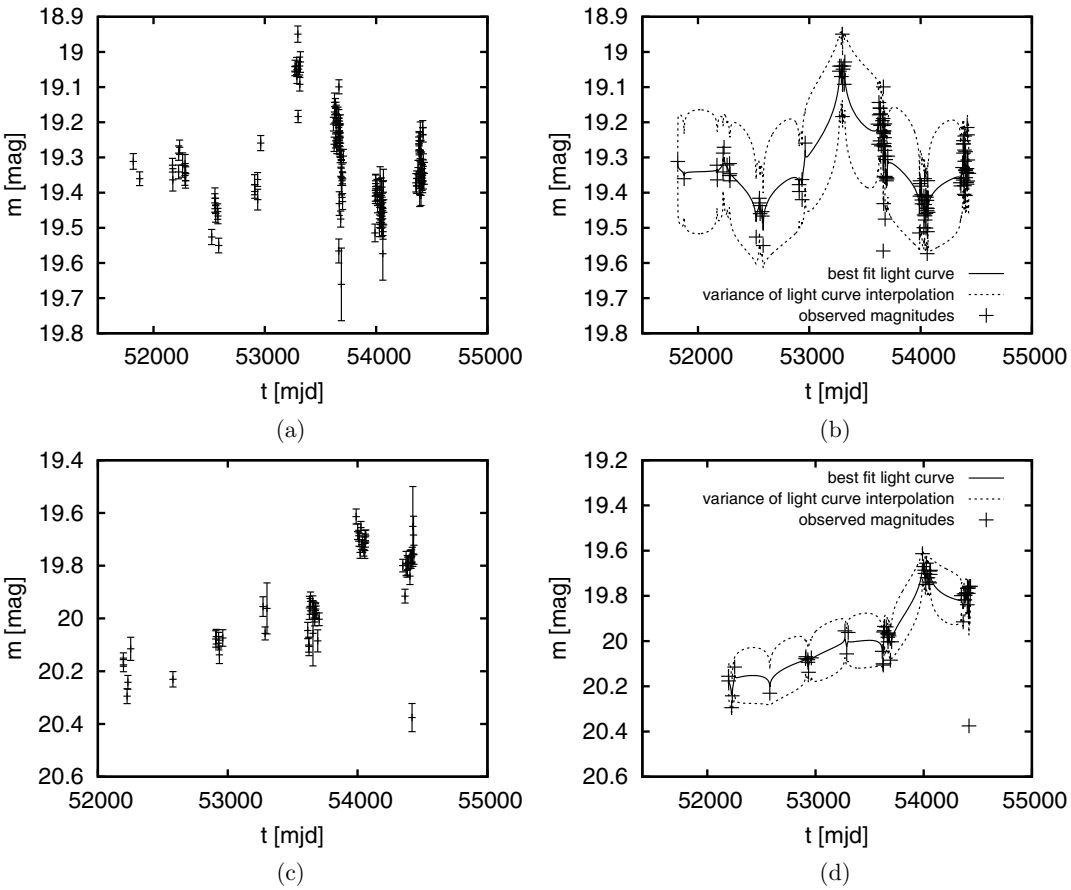

Figure 10. Examples of light curve models for two quasar light curves. The light curves are from spectroscopically confirmed quasars of the SDSS Stripe 82 in a redshift region where the r band is only continuum. They are showing different seasonal gaps. Outliers are excluded when fitting the light curves. The solid lines in the right panel represent the best-fit mean model light curves from the power-law model. The area between the dotted lines represents the error snake, which is the 1σ range of possible stochastic models. The error snakes bound to the reconstructed light curve are thinner than the data points because of the additional measurement error on the data. We also give the best model parameter values along with the confidence intervals (CI). First row: SDSS S82 r band quasar light curve headobjid = 588015509285437517, observation period: 30.9.2000–28.11.2007 (2614.9 days), fitted with a $\bar{m} = 19.331$ mag, $A = 0.136$ (0.68 CI [0.113,0.165], (0.95 CI [0.099,0.216]), $\gamma = 0.205$ (0.68 CI [0.101,0.284], (0.95 CI [0.089,0.393]). Second row: SDSS S82 r band quasar light curve headobjid = 587731185661640908, observation period: 13.10.2001–28.11.2007 (2236.9 days), fitted with a $\bar{m} = 19.993$ mag, $A = 0.175$ (0.68 CI [0.133,0.234], (0.95 CI [0.110,0.348]), $\gamma = 0.256$ (0.68 CI [0.068,0.403], (0.95 CI [0.068,0.627]).

$$+ e\,A^2\left[\left(\frac{t_{\rm obs}}{1\ {\rm yr}}\right)^{\gamma} - \frac{1}{2}\left(\frac{|t_i - t_j + \tau_{\rm delay}|}{1\ {\rm yr}}\right)^{\gamma}\right] \tag{B2}$$

3. covariance matrix for the autocorrelation of the l-band flux:

$$\begin{aligned} C_{ij} = C_{ll}^{(e+c),(e+c)} &= \left\langle f_l^{ec}(t_i) f_l^{ec}(t_j)\right\rangle \\ &= s^2\,A^2\left[\left(\frac{t_{\rm obs}}{1\ {\rm yr}}\right)^{\gamma} - \frac{1}{2}\left(\frac{|t_i - t_j|}{1\ {\rm yr}}\right)^{\gamma}\right] \\ &\quad + s e\,A^2\left[\left(\frac{t_{\rm obs}}{1\ {\rm yr}}\right)^{\gamma} - \frac{1}{2}\left(\frac{|t_i - t_j + \tau_{\rm delay}|}{1\ {\rm yr}}\right)^{\gamma}\right] \\ &\quad + s e\,A^2\left[\left(\frac{t_{\rm obs}}{1\ {\rm yr}}\right)^{\gamma} - \frac{1}{2}\left(\frac{|t_i - t_j - \tau_{\rm delay}|}{1\ {\rm yr}}\right)^{\gamma}\right] \\ &\quad + e^2 A^2\left[\left(\frac{t_{\rm obs}}{1\ {\rm yr}}\right)^{\gamma} - \frac{1}{2}\left(\frac{|t_i - t_j|}{1\ {\rm yr}}\right)^{\gamma}\right] \end{aligned} \tag{B3}$$

where $\tau_{\rm delay}$ is the time delay in years, e is the line response of the l-band emission line to the flux in the x band, and s is the continuum response of the flux in the y band to the flux in the k band.

When using the DRW model instead, one gets the following equations.

1. Covariance matrix for autocorrelation of the k-band continuum:

$$C_{ij} = \langle f_k^c(t_i) f_k^c(t_j)\rangle = \frac{\omega^2}{2}\exp\left(-\frac{|t_i - t_j|}{\tau}\right) \tag{B4}$$

2. Covariance matrix for the correlation function between k-band flux and l-band flux:

$$\begin{aligned} C_{ij} = \left\langle f_k^c(t_i) f_l^{ec}(t_j)\right\rangle &= s\,\frac{\omega^2}{2}\exp\left(-\frac{|t_i - t_j|}{\tau}\right) \\ &\quad + e\,\frac{\omega^2}{2}\exp\left(-\frac{|t_i - t_j + \tau_{\rm delay}|}{\tau}\right) \end{aligned} \tag{B5}$$

3. Covariance matrix for autocorrelation of the l-band flux:

$$\begin{aligned} C_{ij} = \left\langle f_l^{ec}(t_i) f_l^{ec}(t_j)\right\rangle &= s^2\,\frac{\omega^2}{2}\exp\left(-\frac{|t_i - t_j|}{\tau}\right) \\ &\quad + s\,e\cdot\frac{\omega^2}{2}\exp\left(-\frac{|t_i - t_j + \tau_{\rm delay}|}{\tau}\right) \end{aligned}$$

$$+ se\,\frac{\omega^2}{2}\exp\left(-\frac{|t_i - t_j - \tau_{\rm delay}|}{\tau}\right) + e^2\,\frac{\omega^2}{2}\exp\left(-\frac{|t_i - t_j|}{\tau}\right). \quad \text{(B6)}$$

In the case of using a *Gaussian as transfer function*, we first carry out the covariance matrix of the cross-correlation between k-band continuum and l-band line

$$\begin{aligned}\left\langle f_k^c(t_j) f_l^e(t_i)\right\rangle &= \int_{t'=0}^{t_i} dt' \Psi(t_i - t')\left\langle f_k^c(t') f_k^c(t_j)\right\rangle \\ &= \int_{t'=0}^{t_i} dt' \Psi_{\rm Gauss}(t_i - t')\left\langle f_k^c(t') f_k^c(t_j)\right\rangle \\ &= \int_{t'=0}^{t_i} dt' e\,\frac{1}{\sqrt{2\pi\sigma_{\rm Gauss}^2}}\exp\left[-\frac{(t_i - t' - \tau_{\rm delay})^2}{2\sigma_{\rm Gauss}^2}\right] \\ &\quad\times\left\langle f_k^c(t') f_k^c(t_j)\right\rangle \\ &= e\,\frac{1}{\sqrt{2\pi\sigma_{\rm Gauss}^2}}\int_{t'=0}^{t_i} dt' \exp\left[-\frac{(t_i - t' - \tau_{\rm delay})^2}{2\sigma_{\rm Gauss}^2}\right] \\ &\quad\times\left\langle f_k^c(t') f_k^c(t_j)\right\rangle \end{aligned} \quad \text{(B7)}$$

where $\mathrm{erf}(z) = 2/\sqrt{\pi}\int_0^z \exp[-t^2]dt \overset{\text{McLaurin series}}{=} 2/\pi(z - z^3/3 + z^5/10 - z^7/42 + z^9/216 - ...)$. This can be calculated with the `gsl` function `double gsl_sf_erf(double x)`.

In addition, we carry out the covariance matrix of the autocorrelation of the l-band line

$$\begin{aligned}&\left\langle f_l^e(t_j) f_l^e(t_i)\right\rangle \\ &= \int_{t'=0}^{t_i} dt' \int_{t''=0}^{t_j} dt'' \Psi(t_i - t')\Psi(t_j - t'')\left\langle f_k^c(t') f_k^c(t'')\right\rangle \\ &= \int_{t'=0}^{t_i} dt' \int_{t''=0}^{t_j} dt'' \Psi_{\rm Gauss}(t_i - t')\Psi_{\rm Gauss}(t_j - t'')\left\langle f_k^c(t') f_k^c(t'')\right\rangle \\ &= \int_{t'=0}^{t_i} dt' \int_{t''=0}^{t_j} dt'' \cdot \frac{e^2}{2\pi\sigma_{\rm Gauss}^2}\cdot\exp\left[-\frac{(t_i - t' - \tau_{\rm delay})^2}{2\sigma_{\rm Gauss}^2}\right] \\ &\quad\times\exp\left[-\frac{(t_j - t'' - \tau_{\rm delay})^2}{2\sigma_{\rm Gauss}^2}\right]\left\langle f_x^c(t') f_x^c(t'')\right\rangle \end{aligned} \quad \text{(B8)}$$

For the power-law model,

$$\begin{aligned}\left\langle f_k^c(t_j) f_l^e(t_i)\right\rangle &= e\,\frac{1}{\sqrt{2\pi\sigma_{\rm Gauss}^2}}\int_{t'=0}^{t_i} dt' \\ &\quad\times\exp\left[-\frac{(t_i - t' - \tau_{\rm delay})^2}{2\sigma_{\rm Gauss}^2}\right]\left\langle f_x^c(t') f_x^c(t_j)\right\rangle \\ &= e\,\frac{1}{\sqrt{2\pi\sigma_{\rm Gauss}^2}}\int_{t'=0}^{t_i} dt' \exp\left[-\frac{(t_i - t' - \tau_{\rm delay})^2}{2\sigma_{\rm Gauss}^2}\right] A^2 \\ &\quad\times\left(t_{\rm obs}^{\gamma} - \frac{1}{2}\left(\frac{|t_j - t'|}{1\ \rm yr}\right)^{\gamma}\right) \end{aligned} \quad \text{(B9)}$$

$$\begin{aligned}\left\langle f_l^e(t_j) f_l^e(t_i)\right\rangle &= \int_{t'=0}^{t_i} dt' \int_{t''=0}^{t_j} dt'' \frac{e}{\sqrt{2\pi\sigma_{\rm Gauss}^2}} \\ &\quad\times\exp\left[-\frac{(t_i - t' - \tau_{\rm delay})^2}{2\sigma_{\rm Gauss}^2}\right] \\ &\quad\cdot\frac{e}{\sqrt{2\pi\sigma_{\rm Gauss}^2}}\exp\left[-\frac{(t_j - t'' - \tau_{\rm delay})^2}{2\sigma_{\rm Gauss}^2}\right]\left\langle f_x^c(t') f_k^c(t'')\right\rangle \\ &= \int_{t'=0}^{t_i} dt' \int_{t''=0}^{t_j} dt'' \frac{e^2}{2\pi\sigma_{\rm Gauss}^2}\cdot\exp\left[-\frac{(t_i - t' - \tau_{\rm delay})^2}{2\sigma_{\rm Gauss}^2}\right] \\ &\quad\times\exp\left[-\frac{(t_j - t'' - \tau_{\rm delay})^2}{2\sigma_{\rm Gauss}^2}\right] \\ &\quad\cdot A^2\left(t_{\rm obs}^{\gamma} - \frac{1}{2}\left(\frac{|t_j - t'|}{1\ \rm yr}\right)^{\gamma}\right). \end{aligned} \quad \text{(B10)}$$

Unfortunately, these integrals for the power-law structure function are not analytical.

When using a DRW structure function, the integrals are analytical:

covariance matrix of the cross-correlation between the k-band *band* continuum and l-band line

$$\begin{aligned}\left\langle f_k^c(t_j) f_l^e(t_i)\right\rangle &= e\,\frac{1}{\sqrt{2\pi\sigma_{\rm Gauss}^2}}\int_{t'=0}^{t_i} dt' \\ &\quad\times\exp\left[-\frac{(t_i - t' - \tau_{\rm delay})^2}{2\sigma_{\rm Gauss}^2}\right]\left\langle f_k^c(t') f_k^c(t_j)\right\rangle \\ &= e\,\frac{1}{\sqrt{2\pi\sigma_{\rm Gauss}^2}}\int_{t'=0}^{t_i} dt' \exp\left[-\frac{(t_i - t' - \tau_{\rm delay})^2}{2\sigma_{\rm Gauss}^2}\right]\hat{\omega}^2 \\ &\quad\times\exp\left[-\frac{|t_j - t'|}{\tau}\right] \\ &= \frac{1}{2}\exp\left[\frac{\sigma_{\rm Gauss}^2 - 2k\tau(\tau_{\rm delay} + t_j - t_i)}{2\tau^2}\right]\hat{\omega}^2\sigma_{\rm Gauss} \\ &\quad\cdot e\left(\mathrm{erf}\left[\frac{\tau_{\rm delay}\tau - w\sigma_{\rm Gauss}^2}{\sqrt{2}\tau\sigma_{\rm Gauss}^2}\right]\right. \\ &\quad\left. - \mathrm{erf}\left[\frac{\tau_{\rm delay}\tau - w\sigma_{\rm Gauss}^2 - \tau t_i}{\sqrt{2}\tau\sigma_{\rm Gauss}^2}\right]\right) \end{aligned} \quad \text{(B11)}$$

with

$$\hat{\omega} = \sqrt{\frac{2\omega^2}{\tau}} \quad \text{(B12)}$$

and

$$w = \begin{cases} +1, & \text{if } t_j > t_i \\ -1, & \text{if } t_j < t_i \end{cases} \quad \text{(B13)}$$

where per definition $t_j \neq t_i$.

The covariance matrix of the autocorrelation of the l-band line

$$\begin{aligned}\left\langle f_l^e(t_j) f_l^e(t_i)\right\rangle &= \int_{t'=0}^{t_i} dt' \int_{t''=0}^{t_j} dt'' \frac{e}{\sqrt{2\pi\sigma_{\rm Gauss}^2}} \\ &\quad\times\exp\left[-\frac{(t_i - t' - \tau_{\rm delay})^2}{2\sigma_{\rm Gauss}^2}\right] \\ &\quad\cdot\frac{e}{\sqrt{2\pi\sigma_{\rm Gauss}^2}}\exp\left[-\frac{(t_j - t'' - \tau_{\rm delay})^2}{2\sigma_{\rm Gauss}^2}\right]\left\langle f_k^c(t') f_k^c(t'')\right\rangle \\ &= \int_{t'=0}^{t_i} dt' \int_{t''=0}^{t_j} dt'' \frac{e}{\sqrt{2\pi\sigma_{\rm Gauss}^2}}\exp\left[-\frac{(t_i - t' - \tau_{\rm Gauss})^2}{2\sigma_{\rm Gauss}^2}\right] \end{aligned}$$

$$\cdot \frac{e}{\sqrt{2\pi\sigma^2_{\rm Gauss}}} \cdot \exp\left[-\frac{(t_j - t'' - \tau_{\rm delay})^2}{2\sigma^2_{\rm Gauss}}\right]\hat{\omega}^2$$
$$\times \exp\left[-\frac{|t'_t - t''|}{\tau}\right]$$
$$= \frac{1}{4} \cdot \exp\left[-\frac{wt_j\tau^2 + wt_i\tau}{\tau^2}\right]\hat{\omega}^2 e^2$$
$$\cdot \left(\mathrm{erf}\left[\frac{w\tau_{\rm delay}\tau + \sigma^2_{\rm Gauss}}{\sqrt{2}\tau^2\sigma^2_{\rm Gauss}}\right]\right.$$
$$\left. - \mathrm{erf}\left[\frac{w\tau_{\rm delay}\tau - wt_j\tau + \sigma^2_{\rm Gauss}}{\sqrt{2}\tau^2\sigma^2_{\rm Gauss}}\right]\right)$$
$$\cdot \left(\mathrm{erf}\left[\frac{\tau_{\rm delay}\tau - w\sigma^2_{\rm Gauss}}{\sqrt{2}\tau\sigma^2_{\rm Gauss}}\right]\right.$$
$$\left. - \mathrm{erf}\left[\frac{\tau_{\rm delay}\tau - w\sigma^2_{\rm Gauss} - \tau t_i}{\sqrt{2}\tau\sigma^2_{\rm Gauss}}\right]\right) \quad \text{(B14)}$$

with

$$w = \begin{cases} +1, & \text{if } t_j > t_i \\ -1, & \text{if } t_j < t_i \end{cases} \quad \text{(B15)}$$

where per definition $t_j \neq t_i$.

From this, we can calculate the covariance matrix for the correlation function between the k-band *band* flux and l-band flux, and the covariance matrix for autocorrelation of the l-band flux by inserting Equations (B11) and (B14) into Equations (17) and (18).

APPENDIX C
TEST DATA

Equipped with a statistical description of quasar variability (see Section 3), we generate well-sampled mock light curves in order to (1) test the algorithm for the determination of the structure-function parameters and later for reverberation mapping, (2) demonstrate the relationship between our model parameters and the shape of light curves, and (3) estimate the systematic effects that the sampling rate and light curve length have on the fitted parameter for determination of the structure-function parameter and for reverberation mapping. The later is especially important because the SDSS S82 data are fairly sparse.

C.1. Generating Test Data

A continuum light curve is generated using only the two structure-function parameters and the mean magnitude of the light curve as input parameters. To apply a time delay $\tau_{\rm delay}$ to the continuum plus emission line light curves, we refer to our assumption that all emission line light curves are scaled, smoothed, and displaced (delayed) versions of the continuum flux light curve, see Equation (11).

For generating the test data, one can choose

1. the structure function; here, a DRW model and a power-law model are implemented
2. the transfer function $\Psi(\tau_{\rm delay})$; here, a δ function and Gaussian are implemented
3. scaling factors s, e (instead of the emission line equivalent width)
4. the bands x and y, multiple emission lines are also possible
5. the time sampling and time windows; this can be chosen freely and also be inherited from SDSS S82 light curves.

As mock data are generated from e and s, and not with emission line equivalent width, we replace Equations (37) by

$$P(e) = \frac{1}{\sqrt{2\pi}\delta e_0} \exp\left(-\frac{(e - e_0)^2}{2\delta e0^2}\right), \quad \text{(C1)}$$

when testing with mock data. The values for e_0 and δe_0 are set depending on test, typical $e_0 \approx 0.2$, $\delta e_0 \approx 0.02$.

To make sure that the test data are consistent, samples of mock light curves are evaluated statistically. When averaging over a sample of 100 light curves with the same structure function V, the form of the point cloud $|\Delta m|$ versus $|\Delta t|$ should be represented by $\sqrt{V(|\Delta t|)}$ as a ridge-line. In addition, the standard deviation SD($|\Delta m|$) should be represented by the structure function itself, $V(|\Delta t|)$.

For the purpose of illustrating these effects, an observation time of 12 yr and observational time sampling of one day was simulated. The first and last years of the data points are neglected to avoid potential edge effects, which results in 10 yr of observational time. As shown in Figure 11, for both the power law and the damped random walk structure functions, the form of the point cloud $|\Delta m|$ versus $|\Delta t|$ is represented quite well by $\sqrt{V(|\Delta t|)}$ as a ridge-line, and the standard deviation is represented by the structure function itself, $V(|\Delta t|)$. In addition, it is plausible that about 63 percent of points of $|\Delta m|$ versus $|\Delta t|$ will be under the line (with the fraction of data being within 1σ in a Gaussian distribution). As a result, we know that the generated mock light curves follow our assumptions about structure functions. Because of this, we can be sure that such mock light curves can be used safely to test our algorithms for estimating structure-function parameters and reverberation mapping.

C.2. Results from Test Data

In this section we show results from mock data, which lead us to an understanding of the behavior of the reverberation mapping algorithm.

The structure-function parameter function is estimated by evaluating Equation (A20) as described in Section 3. This can be carried out on a parameter grid or by using a MCMC method. Using a parameter grid is not practical because it is time consuming, but functions for testing issues and to show the likelihood surface.

We found that the method is sufficient for estimating structure function parameters and fitting light curves, as even with sparsely sampled mock data it is able to recover the input values within about a 68% confidence interval or better. We also see that the posterior distribution in the parameter space, like the likelihood surface itself, is smooth, so the MCMC is able to sample the posterior distribution.

During first tests on estimation of the time delay $\tau_{\rm delay}$, uniformly sampled mock data were used. Using uniformly sampled light curves spanning a time longer than the input $\tau_{\rm delay}$, this delay can be recovered with a precision of one over the sampling frequency. This holds even when the flux contribution is about 5% (this is the expected value for many of the SDSS S82 light curves, whereas some have a flux contribution up to 20%). For more realistic tests, we have taken typical SDSS S82 time sampling and applied it to mock light curves. As expected,

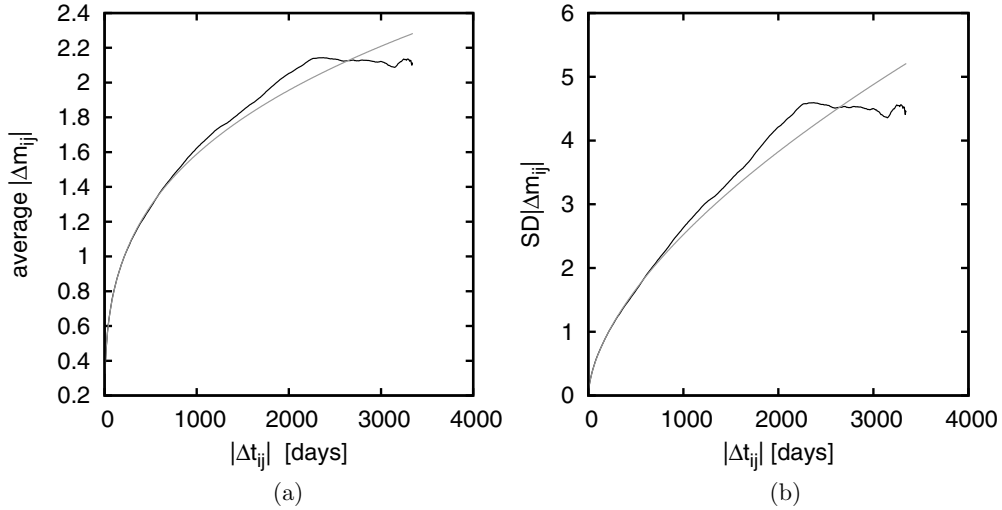

(a) (b)

Figure 11. Light curve statistics over $|\Delta t_{ij}|$ for 100 simulated power-law light curves, where i,j are the individual observations; (a) black curve: averaged $|\Delta m_{ij}|$, gray curve: $\sqrt{V(|\Delta t|)}$, (b) black curve: standard deviation of $|\Delta m_{ij}|$, gray curve: $V(|\Delta t|)$.

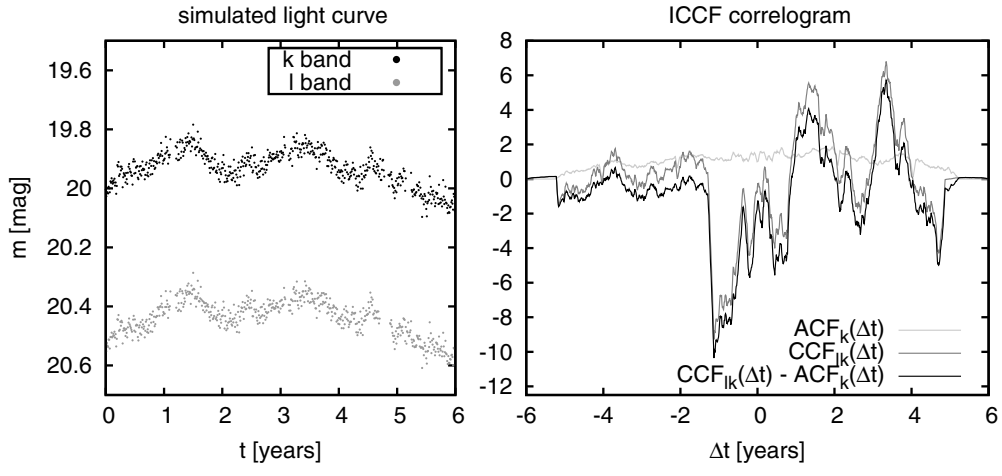

(a) (b)

Figure 12. Non-uniform sampled simulated light curve and its correlogram, input $\tau_{\rm delay} = 1$ yr is recovered as $\tau_{\rm delay} = 3.33$ yr. Band k contains continuum only, band l contains continuum and emission line.

the approach is sensitive to time sampling, but not as much as classical approaches such as CCF and ICCF. For an example plot, see Figure 12.

We found that we can easily estimate whether a given time sampling enables us to find a time delay in an expected range. The tool used for this is the histogram of observational time lags provided by the light curve in question. Details on this can be found in Section 5.

Despite the robustness of the stochastic approach, results must be handled with care. Even when the algorithm is able to recover the input $\tau_{\rm delay}$, we found that for sparsely sampled data the posterior distribution often turns out to be much more flat than for estimating the structure-function parameters. Additionally, the periodic pattern of higher and lower likelihood can be found in mock and real data. This pattern roughly reproduces the pattern in the histogram of observational time lags. As a result, we constrain the $\tau_{\rm delay}$ by Equation (24) and set a prior on (e, s) based on spectroscopic data. For details, see Section 5, Equation (27)–(37).

If those priors are applied, this periodic pattern only appears in some cases. When it appears, it is only weak. Most posterior distribution functions are smooth and round, whereas others have a stretched appearance or show a tail, which is a remnant of the periodic pattern. This demonstrates the importance of choosing a sensible prior.

REFERENCES

Andrae, R., Kim, D.-W., & Bailer-Jones, C. A. L. 2013, A&A, 554, 11
Annis, J., Soares-Santos, M., Strauss, M. A., et al. 2014, ApJ, 794, 120
Bentz, M. C., Denney, K. D., Grier, C. J., et al. 2013, ApJ, 767, 149
Bentz, M. C., Peterson, B. M., Netzer, H. M., et al. 2009, ApJ, 697, 160
Bentz, M. C., Walsh, J. L., Barth, A. J., et al. 2010, ApJ, 716, 993
Blandford, R. D., & McKee, C. F. 1982, ApJ, 255, 419
Butler, N. R., & Bloom, J. S. 2011, AJ, 141, 93
Chelouche, D., & Daniel, E. 2012, ApJ, 747, 62
Chelouche, D., Shemmer, O., Cotlier, G. I., Barth, A. J., & Rafter, S. E. 2014, ApJ, 785, 140
Chelouche, D., & Zucker, S. 2013, ApJ, 769, 124
Collier, S., & Peterson, B. M. 2001, ApJ, 555, 775
Edri, H., Rafter, S. E., Chelouche, D., Kaspi, S., & Behar, E. 2012, ApJ, 756, 73
Foreman-Mackey, D., Hogg, D. W., Lang, D., & Goodman, J. 2012, PASP, 125, 306
Frieman, J. A., Bassett, B., Becker, A., et al. 2008, AJ, 135, 338
Gaskell, C. M., & Peterson, B. M. 1987, ApJ, 65, 1

Greenstein, J. L., & Schmidt, M. 1964, ApJ, 140, 1
Haas, M., Chini, R., Ramolla, M., et al. 2011, A&A, 535, 11
Helfand, D. J., Stone, R. P. S., Willman, B., et al. 1994, MNRAS, 268, 305
Hughes, P. A., Aller, H. D., & Aller, M. F. 1992, ApJ, 396, 469
Ivezić, Z., Beers, T. C., & Jurić, M. 2012, ARA&A, 50, 251
Kaspi, S., Brandt, W. N., Maoz, D., et al. 2007, ApJ, 659, 997
Kaspi, S., Smith, P. S., Netzer, H., et al. 2000, ApJ, 533, 631
Kelly, B. C., Bechtolz, J., & Siemiginowska, A. 2009, ApJ, 698, 895
Kozłowski, S., Kochanek, Ch. S., et al. 2010, ApJ, 708, 927
MacLeod, Ch. L., Ivezić, Ž, Kochanek, C. S., et al. 2010, ApJ, 721, 1014
MacLeod, Ch. L., Ivezić, Z., Sesar, B., et al. 2012, ApJ, 753, 106
Morganson, E., Burgett, W. S., Chambers, K. C., et al. 2014, ApJ, 784, 92
Peterson, B. M. 1997, An Introduction to Active Galactic Nuclei (Cambridge: Cambridge Univ. Press)
Peterson, B. M. 2013, SSRv, 60
Peterson, B. M., Ferrarese, L., Gilbert, K. M., et al. 2004, ApJ, 613, 682
Peterson, B. M., & Wandel, A. 1999, ApJL, 521, L95
Press, W. H., & Rybicki, G. B. 1992, ApJ, 385, 404
Rasmussen, C. E., & Williams, C. K. I. 2006, Gaussian Processes for Machine Learning (Cambridge, MA: MIT Press)
Richards, G. T., Myers, A. D., Gray, A. G., et al. 2008, ApJS, 180, 67
Richards, G. T., Strauss, M. A., Fan, X., et al. 2006, AJ, 131, 2766
Rybicki, G. B., & Kleyna, J. T. 1994, PASP, 69, 85
Rybicki, G. B., & Press, W. H. 1992, ApJ, 398, 169
Schmidt, K. B., Marshall, P. J, Rix, H.-W., et al. 2010, ApJ, 714, 1194
Schmidt, K. B., Rix, H.-W., Shields, J. C., Knecht, M., et al. 2012, ApJ, 744, 147
Schneider, D. P., Hall, P. B., Richards, G. T., et al. 2007, AJ, 134, 102
Shen, Y., Richards, G. T., Strauss, M. A., et al. 2011, ApJS, 194, 45
Smith, H. J., & Hoffeit, D. 1965, Natur, 198, 650
Vanden Berk, D. E., Richards, G. T., Bauer, A., et al. 2001, AJ, 122, 549
Vestergaard, M. 2002, ApJ, 571, 733
Vestergaard, M., & Peterson, B. M. 2006, ApJ, 641, 689
Welsh, W. F. 1999, PASP, 111, 765
York, D. G., Adelman, J., Anderson, J. E., Jr., et al. 2000, AJ, 120, 1579
Zu, Y., Kochanek, C. S., Kozłowski, S., & Peterson, B. M. 2013a, arXiv:1310.6774
Zu, Y., Kochanek, C. S., Kozłowski, S., & Udalski, A. 2013b, ApJ, 765, 106
Zu, Y., Kochanek, C. S., & Peterson, B. M. 2011, ApJ, 735, 80